Global Dynamic Topography Observations Reveal Limited Influence of Large-Scale Mantle Flow

M. J. Hoggard*, N. White & D. Al-Attar

April 28, 2016

Bullard Laboratories, Department of Earth Sciences, University of Cambridge, Madingley Rise, Madingley Road, Cambridge, CB3 0EZ, UK. *email: mjh217@cam.ac.uk, njw10@cam.ac.uk

Convective circulation of the Earth's mantle maintains some fraction of surface topography that varies with space and time. Most predictive models show that this dynamic topography has peak amplitudes of ± 2 km, dominated by wavelengths of 10^4 km. Here, we test these models against our comprehensive observational database of 2,120 spot measurements of dynamic topography that were determined by analysing oceanic seismic surveys. These accurate measurements have typical peak amplitudes of ± 1 km and wavelengths of approximately 10^3 km and are combined with limited continental constraints to generate a global spherical harmonic model whose robustness has been carefully tested and benchmarked. Our power spectral analysis reveals significant discrepancies between observed and predicted dynamic topography. At longer wavelengths (such as 10^4 km), observed dynamic topography has peak amplitudes of ± 500 m. At shorter wavelengths (such as 10^3 km), significant dynamic topography is still observed. We show that these discrepancies can be explained if short-wavelength dynamic topography is generated by temperature-driven density anomalies within a sub-plate asthenospheric channel. Stratigraphic observations from adjacent continental margins show that these dynamic topographic signals evolve quickly with time. More rapid temporal and spatial changes in vertical displacement of the Earth's surface have direct consequences for fields as diverse as mantle flow, oceanic circulation and long-term climate change.

Topography and bathymetry at the Earth's surface are isostatically maintained by variations in the thickness and density of crust and lithospheric mantle. Thus mountain belts have thicker crust whereas depressions have thinner crust. In the oceanic realm, subsidence away from mid-oceanic ridges is dominated by cooling and thickening of the lithospheric plate. Nevertheless, it is generally recognised that some fraction of topography and bathymetry are controlled by a changing pattern of convective circulation within the underlying mantle[1]. Spatial and temporal patterns of this dynamic topography contain useful clues about the fluid mechanical properties of the convecting interior[2]. Pekeris[1] showed that, within a convecting Earth, normal stresses generated by internal flow act to deform the Earth's surface. Later, Richards and Hager[3] demonstrated that surface deflections and geoid variations are produced by lateral density anomalies within the mantle. In both cases, the response kernels (i.e. Green's functions) depend on the assumed radial viscosity structure of the mantle.

Agreement between observed and predicted geoid anomalies for spherical harmonic degrees $l = 2$–6 (i.e. wavelengths of $16,000$–$6,000$ km) is obtained using a density model estimated

by assuming that seismic anomalies within the lower mantle have a thermal origin[4,5,6]. For an acceptable range of radial viscosity functions, this density model predicts long-wavelength dynamic topographic anomalies with amplitudes of ± 1 km at wavelengths corresponding to $l = 2$–3[4]. Although the paradox that long-wavelength positive density anomalies within the lower mantle correlate with negative geoid anomalies was resolved if the lower mantle is ten times more viscous than the upper mantle, detailed observations were unavailable to test predicted patterns of dynamic topography.

Subsequent studies have explored complementary approaches for inferring mantle density structure which is then used to match long-wavelength geoid anomalies and to predict dynamic topography. For example, some instantaneous flow models exploit present-day mantle densities inferred from global seismic tomography[7,8]. Other models are based upon time-integrated histories of Phanerozoic plate subduction[9,10]. More controversially, time-dependent convective simulations of present-day density structures have been carried out using forward, backward and adjoint methods[11,12,13]. Despite increasing levels of computational complexity, these different models yield broadly similar dynamic topographic patterns, dominated by $l = 2$–6 with peak amplitudes of 1–3 km and root-mean-squared (rms) amplitudes of 0.5-1.0 km[10].

Global Residual Depth Measurements

Our goal is to develop an accurate spherical harmonic model of observed dynamic topography. Identifying dynamic topography is complicated by the need to separate it from isostatic topography generated by thickness and density contrasts within the lithospheric plates. Cooling and thickening of oceanic lithosphere generate a predictable relationship for subsidence as a function of age[14]. If the effects of plate cooling, loading and flexure are accurately removed, residual depth anomalies are isolated that can be regarded as proxies for oceanic dynamic topography[15]. A new database comprising 1,124 seismic reflection profiles, 191 seismic wide-angle (i.e. waveform-modelled) experiments, and 341 vintage seismic refraction (i.e. slope-intercept-modelled) experiments has been compiled (Figure 1a). This database provides comprehensive coverage of the oceanic realm with a bias toward the oldest oceanic crust that abuts continental margins. Regions where flexural bending and large amplitude but short-wavelength free-air gravity anomalies exist have been excluded (Supplementary Information).

On each image, *bona fide* oceanic crust is identified from its characteristic acoustic architecture and magnetic anomaly pattern[17]. On seismic reflection profiles, the sediment-basement interface is usually clear whilst the base of the crust (i.e. Moho) often consists of a single bright reflection (Figure 2a-c). Reliability of crustal models determined from reversed seismic wide-angle and refraction experiments depends upon vintage of the experiment and upon modelling technique. Optimal results come from modern, densely sampled experiments where observed and calculated travel times and waveforms are matched by forward or inverse modelling. It is important that the horizontal range of these experiments is great enough to observe diving waves turning within the upper mantle. Older refraction experiments analysed using slope-intercept methods typically underpredict true crustal thickness by $\sim 20\%$[18]. We measured water-loaded oceanic residual depth anomalies using a well-established approach[19,20,21]. Two isostatic corrections allow for variable sedimentary and crustal loading (Methods). Accuracy of the sedimentary correction depends upon calibration between two-way travel time and depth, which is obtained from 43 locations where seismic reflection and wide-angle surveys intersect. Observed crustal thicknesses are used to determine the crustal correction which assumes a reference crustal thickness of 7.1 km and a reference density of 2.86 Mg m^{-3}. Crustal age is

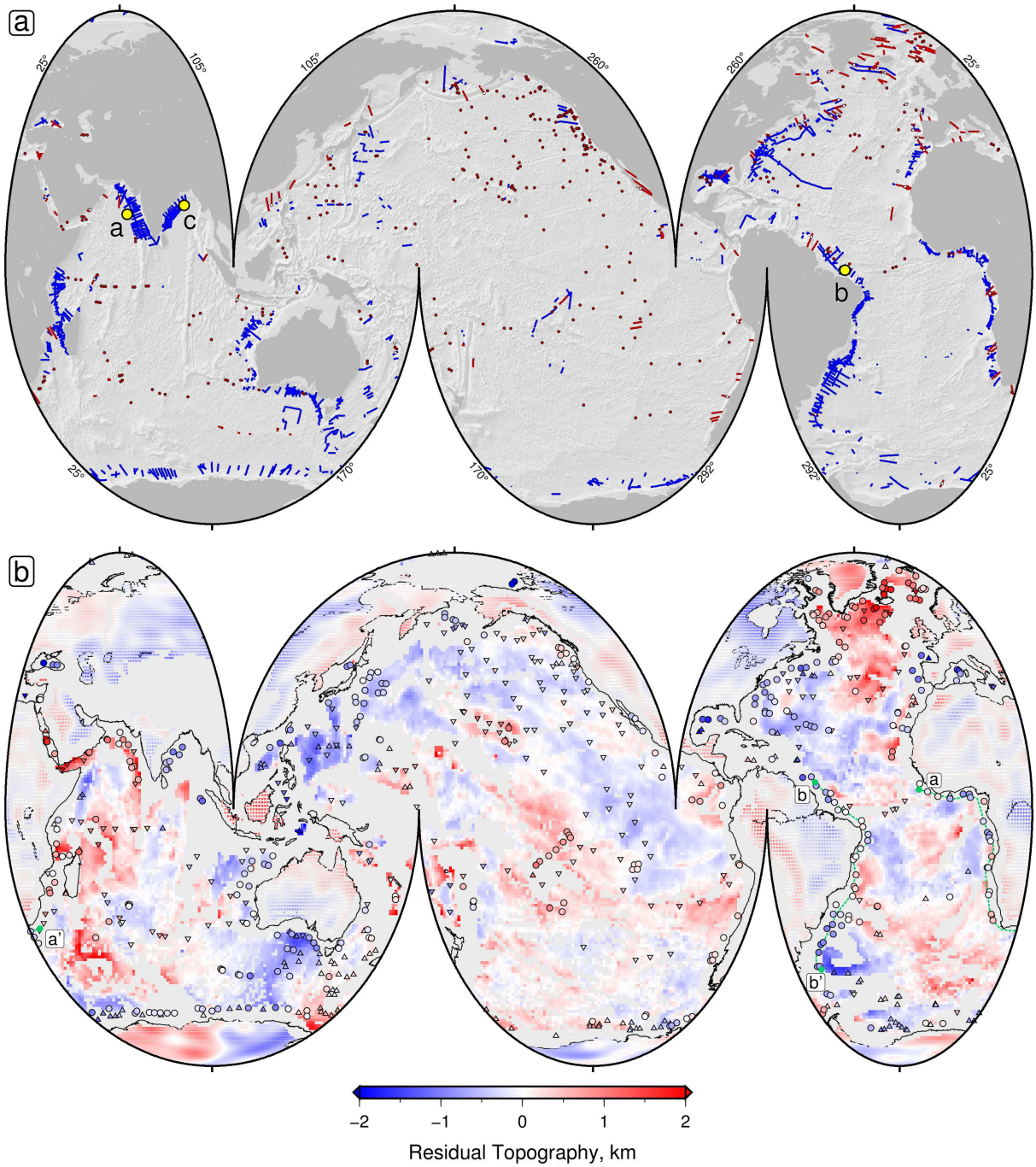

Figure 1: Maps of seismic and residual topographic databases. (a) Segmented Mollweide projection of global bathymetry sampled every 0.25°. Blue lines = 1,164 legacy seismic reflection profiles; red lines = 191 waveform-modelled seismic wide-angle experiments; red circles = locations of 341 slope-intercept modelled seismic wide-angle experiments; yellow circles = three seismic reflection images shown in Figure 2; small white circles = 43 intersections between reflection profiles and wide-angle seismic experiments used to calibrate the sedimentary correction. (b) Residual topographic measurements sampled in 4° bins (red/blue = positive/negative). Circles = measurements with sedimentary and crustal corrections; upward/downward pointing triangles = measurements with lower/upper limits only; offshore grid = residual topography estimated from edited ship-track database, sampled every 1°; onshore grid = residual topography calculated by scaling long-wavelength (> 700 km) free-air gravity anomalies sampled every 1° using an admittance, $Z = 50$ mGal/km[16]; green dashed lines labelled a–a′ and b–b′ = transects shown in Figure 3.

determined from the pattern of magnetic anomalies[17].

Resultant water-loaded depths to basement can be compared with a revised global oceanic age-depth relationship[22]. This relationship is preferable since it is based upon a global observational database from which anomalous oceanic crust and regions of dynamic topography were excised. We obtain similar results when alternative age-depth relationships are used (Supplementary Information). Most residual topography anomalies fall within ± 1 km of the expected age-depth relationship with a mean value of -60 m and a standard deviation of ~ 700 m. Positive anomalies tend to be associated with the youngest crust close to mid-oceanic ridges and negative anomalies occur within the oldest oceanic basins (Figure 2d). Positive anomalies with amplitudes of 1–2 km and wavelengths as great as 2500 km occur in the vicinity of the Icelandic, Hawaiian, Azorean and Afar plumes (Figure 1b). Similarly large negative anomalies occur along the east coast of North America, in the Gulf of Mexico, and between Australia and Antarctica.

Offshore West Africa, several cycles of smoothly varying residual topographic anomalies are observed (Figure 3a). Anomalies are negligible at the northern end of this transect before decreasing to -800 m at the Guinea Abyssal Plain. The Cameroon Volcanic Line sits on top of an elongated swell with a positive anomaly of up to +900 m. This anomaly decreases southwards to -1 km offshore Gabon. A second cycle steadily rises to +800 m at the offshore expression of the Angolan Dome. Different patterns of anomalies are observed along the Brazilian margin (Figure 3b). Notably, the Argentine abyssal plain is characterised by a $\sim$2000 km wide negative anomaly which is probably one of the largest convective drawdowns on Earth[23].

These long-wavelength anomalies cannot be maintained by lithospheric flexure but are generated by convective circulation. The match between our measurements and long-wavelength free-air gravity anomalies suggests that the gravity field is a reasonable proxy for dynamic topography elsewhere. Existence of these anomalies is corroborated by independent geological constraints which also demonstrate that they evolve rapidly with time. For example, the position of the Angolan Dome, which has a diameter of 1000 km and an amplitude of +800 m, coincides with evidence for $\sim$500 m of post-Pliocene uplift estimated from truncation of deltaic topset deposits along the continental shelf[24]. The adjacent coastline is characterised by emergent marine terraces that record Quaternary uplift rates of 0.3 mm yr^{-1} [25]. Both observations are consistent with an uplift rate history calculated from inverse modelling of river profiles that radially drain the Angolan Dome[26].

Spherical Harmonic Analysis

In the oceans, spot measurements are supplemented with conservatively edited grids of residual depth measurements. Water depths were measured from ship-track bathymetry[27]. Sedimentary corrections were calculated using global digital grids[28,29]. These grids have significant errors along continental margins and so we have excised regions where sediment is thicker than 1.5 km. Areas of anomalously thin/thick crust were also conservatively excised (e.g. seamounts, plateaux, fracture zones, flexural moats; Supplementary Information). At their intersections, spot and ship-track derived measurements generally match.

To generate a global spherical harmonic model of observed dynamic topography, more limited continental constraints are included. Attempts to constrain continental dynamic topography are complicated by variable lithospheric architecture[30]. Here, we have exploited two different strategies. Continental dynamic topography can be isostatically gauged using thickness and density measurements taken from the global CRUST1.0 database (Supplementary Informa-

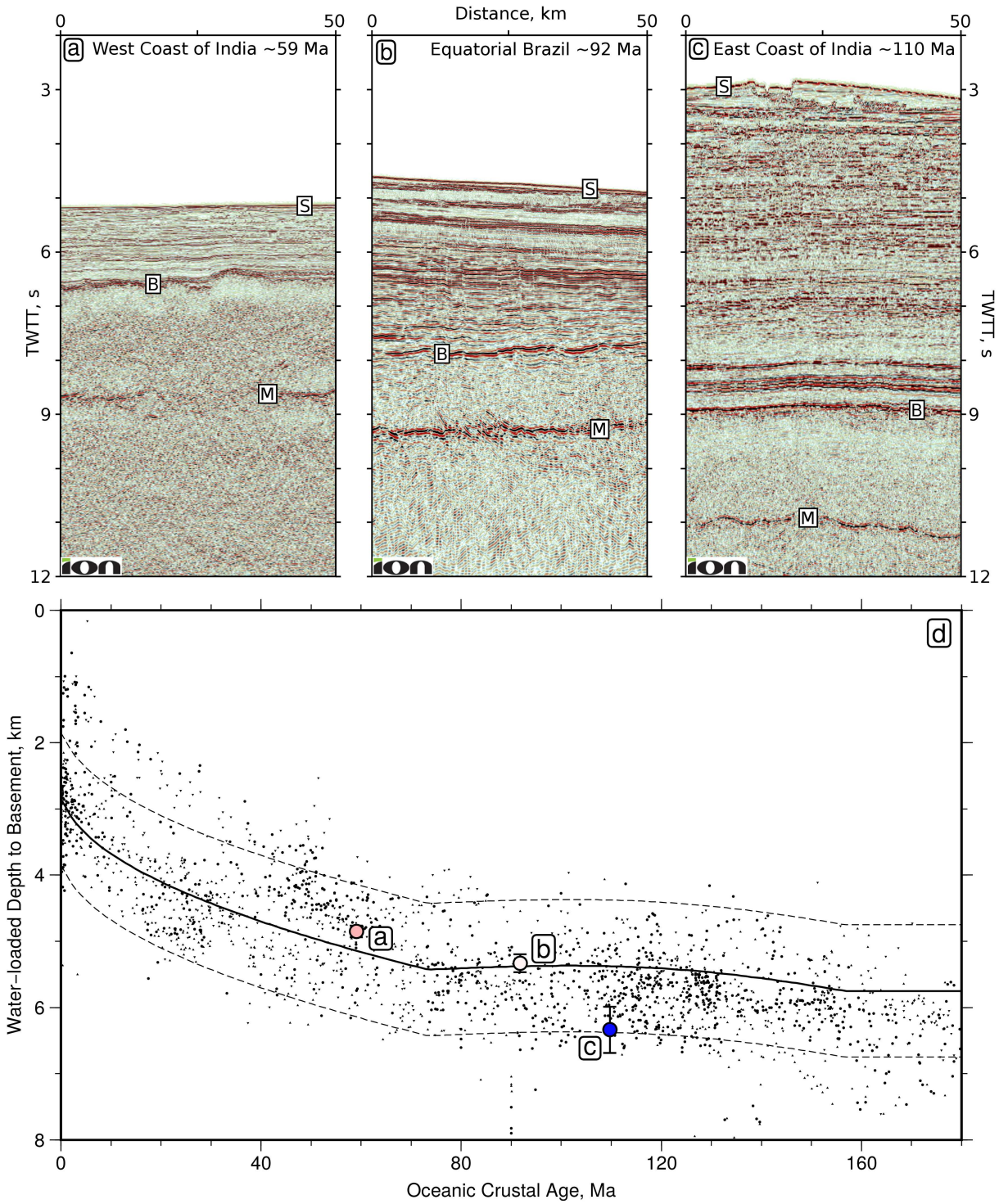

Figure 2: Images of oceanic crust. (a) Seismic reflection profile of 59 Ma oceanic crust (west of India). S = seabed; B = sediment-basement interface; M = Moho (i.e. base of crust); TWTT = two-way travel time. (b) 92 Ma oceanic crust (offshore Brazil). (c) 110 Ma oceanic crust (east of India). Crustal ages from magnetic reversal history[17]. Images shown courtesy of ION. (d) Black symbols = 2,120 age-depth measurements from seismic reflection/wide-angle experiments plotted as function of plate age; solid line = age-depth relationship of Crosby and McKenzie[22]; dashed lines = ± 1 km either side of age-depth relationship; Labelled coloured circles = age-depth measurements calculated from above three profiles, where colour = amplitude of residual depth anomaly (scale on Figure 1). Error bars represent 1σ uncertainties (Methods).

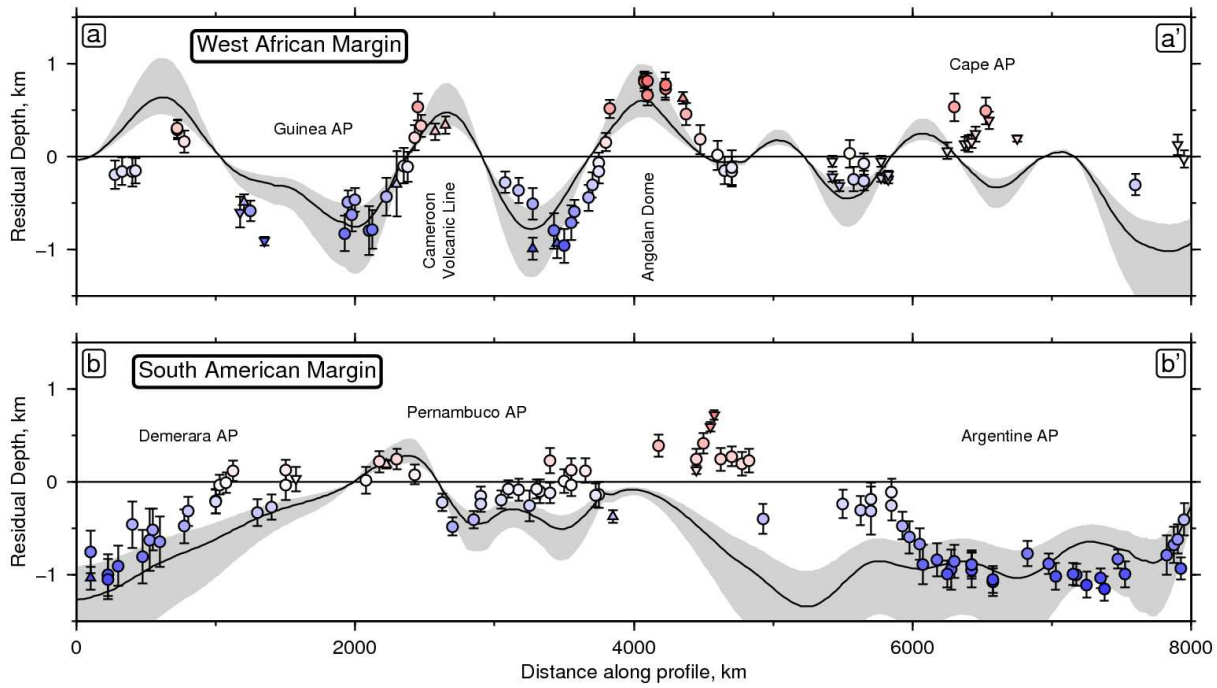

Figure 3: Transects along oldest oceanic crust of South Atlantic margins. (a–a′) West African margin. Coloured circles/triangles = residual depth measurements averaged within 1° bins with one σ uncertainty located within 80 km of transect; black line with grey band = dynamic topography calculated from long-wavelength (700–9,000 km) free-air gravity anomalies using $Z = 25 \pm 10$ mGal/km; AP = Abyssal Plain. (b–b′) South American margin. Both transects are approximately perpendicular to plate-spreading flowlines.

tion). However, since our oceanic analyses show that free-air gravity anomalies are a reliable proxy, we prefer to seed continents with estimates of dynamic topography that are based upon the coherence between long-wavelength gravity anomalies, topography and drainage patterns. First, the GRACE gravity field was low-pass filtered to remove wavelengths shorter than about 700 km (i.e. $l = 55$)[31]. Secondly, these long-wavelength anomalies were scaled by assuming a constant air-loaded admittance of $Z = 50$ mGal km^{-1}. We have also tested the effects of using different values and functional forms of Z (Supplementary Information)[16,32]. Thirdly, anomalies which occur within 500 km of oceanic residual depth measurements were removed. We excised all active orogenic belts and zones of flexural bending (Supplementary Information). The reliability of the remaining gravity anomalies is checked by plotting drainage networks and hotspot volcanism which typically show that radial drainage occurs away from positive anomalies[26]. The combined offshore and onshore database is shown in Figure 1b. This approach is reliable for Africa, Arabia, western North America and eastern Australia where long-wavelength gravity anomalies and topography correlate[26,33,34,35].

We have fitted spherical harmonic functions to this global database using a regularised least squares inversion algorithm (Methods). Figure 4a shows a damped model that was fitted up to, and including, $l = 30$. This model yields a residual misfit of $\chi^2 \sim 1$ (Figure 5a). If lower degree models are used to fit the global database, χ^2 is substantially larger (e.g. $\chi^2 \sim 8$ for an $l = 2$ model). These results imply that it is necessary to include shorter wavelength functions in order to adequately fit the observational database. If only accurate spot measurements are used, χ^2 is larger, suggesting that higher degree structure is present. The robustness of our inverse

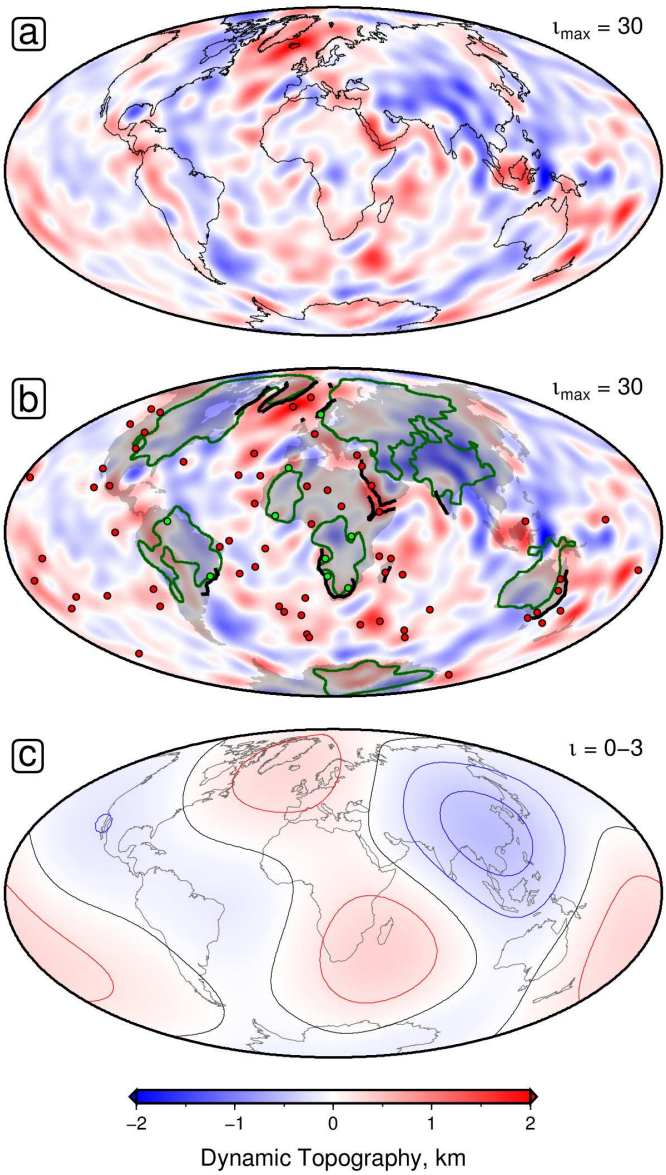

Figure 4: Observed dynamic topography. (a) Spherical harmonic model up to $l = 30$ of measurements shown in Figure 1b. (b) Model overlain with other geological/geophysical observations. Green polygons = continental lithosphere > 150 km thick[36]; red/green circles = magmatic/amagmatic topographic swells with radial drainage patterns (Supplementary Information); black lines = prominent anorogenic escarpments. (c) $l = 0$–3 components of spherical harmonic model. Contour lines every 200 m; black line = zero contour.

method has been tested by carrying out a battery of checkerboard tests, damping parameter sweeps, and spatial coverage analyses (Supplementary Information). We have also carefully tested the consequences of using alternative age-depth models. Crucially, if the CRUST1.0 database is used to calculate continental dynamic topography, or if continents are completely excluded, the resultant spectra are practically identical (Supplementary Figure S3).

Our global model is consistent with independent geological observations. Active hotspot volcanism, radial drainage patterns, and prominent escarpments all occur in regions of positive dynamic support and often coincide with embayments into thick cratonic lithosphere (Figure 4b). The longest wavelength components of our spherical harmonic model (i.e. $l = 0$–3)

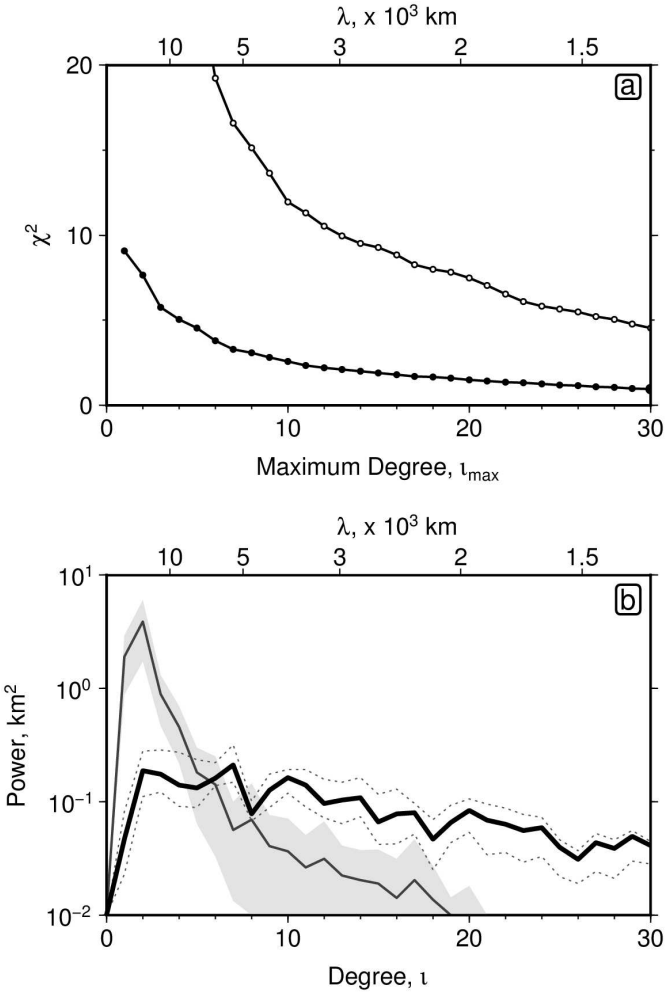

Figure 5: Residual misfit and power spectra. (a) Residual misfit, χ^2, plotted as function of maximum degree, $l_{\max}$, used to fit observations (Figure 1b). Solid circles = χ^2 values from fitting combined offshore/onshore global database of dynamic topographic observations; open circles = χ^2 values from fitting spot measurements from oceanic realm alone. Corresponding wavelengths, λ, are shown at the top. (b) Black solid line = power spectrum obtained by regularised least squares inversion of global database of dynamic topography observations; dotted lines = uncertainty resulting from range of gradient regularisation and amplitude damping coefficients ($10^{-0.5}$–$10^{+0.5}$ and 10^2–10^3, respectively); thin line with grey bounds = mean and standard deviation of power spectra for five predictive models of dynamic topography[7,8,9,10,13].

broadly agree with the pattern of geoid anomalies (Figure 4c). For example, positive anomalies occur over the Icelandic plume, over sub-equatorial Africa, and over the west Pacific Ocean. Negative anomalies occur over southeast Asia, over equatorial South America, and over western North America. Amplitudes of these long-wavelength anomalies are significantly smaller than those predicted by most models. The rms amplitude for $l = 0$–3 is 170 m with peaks of -515 m and +373 m. A typical predictive model has an rms amplitude of 648 m with peaks of -1658 m and +1664 m for $l = 0$–3[10].

Geodynamical Consequences

Power spectral analyses of our observations and of predictive models reveal significant differences (Figure 5b). Predictive models are spectrally red with a prominent peak at $l = 2$. In contrast, the observed spectrum has one order of magnitude less power at $l = 2$ with much greater power at $l = 20$–30. Significantly, the slope of this spectrum matches Kaula's Rule, even when continental observations are excluded (Supplementary Information). Differences between these observed and predicted spectra yield new and important insights into the nature of mantle convection. If viscosity varies as a function of radius alone, Hager and Richards[37] showed that the geoid and dynamic topography at the Earth's surface can be calculated from

$$\delta N^{lm} = \frac{4\pi G a}{g(2l+1)} \int_r^a G^l(r)\, \delta\rho^{lm}(r)\, dr \tag{1}$$

and

$$\delta a^{lm} = \frac{1}{\Delta\rho_a} \int_r^a A^l(r)\, \delta\rho^{lm}(r)\, dr \tag{2}$$

where δN^{lm} is the geoid height and δa^{lm} is deflection of the Earth's surface. g is acceleration due to gravity and $\Delta\rho_a$ is the density difference between mantle and water (or air). $G^l(r)$ and $A^l(r)$ are normalised geoid and surface response kernels as a function of radius, r, for a density anomaly located at different depths within the mantle. Finally, $\delta\rho^{lm}(r)$ represents mantle density anomalies. Superscripts l and m refer to spherical harmonic degree and order, respectively (Methods). Predicted geoid and dynamic topography depends upon viscosity structure and upon the distribution of mantle density anomalies. Figures 6c and 6d show how $G^l(r)$ and $A^l(r)$ vary with degree for a typical radial viscosity function[38].

Mantle density anomalies are computed directly from seismic tomographic models by scaling shear wave velocity anomalies. It is generally accepted that temperature variations are the dominant control although compositional variations play some role e.g.[5,6,39]. A useful rule of thumb is to multiply shear wave velocity anomalies by 0.2 (Mg m^{-3})(km s^{-1})$^{-1}$. Forte[39] analysed a suite of six global tomographic models and used a range of scaling factors to calculate the average magnitude of density anomaly as a function of radius (Figure 6e). Lateral density variations are important within the top 1000 km and bottom 1000 km of the mantle, reflecting the distribution of shear wave velocity anomalies.

Geoid variations and dynamic topography are calculated by convolving response kernels with density profiles (Figure 6c–e). Since the observed velocity (and inferred density) structure of the whole mantle are dominated by $l = 2$, calculated water-loaded dynamic topography has an amplitude of 1.5 ± 0.4 km, in accordance with the suite of predicted power spectra shown in Figure 5b. This value is much larger than the $l = 0$–3 components of the observed dynamic topography model which have an amplitude range of 888 m (Figure 4c). To isolate the source of this discrepancy, we divide the problem into two parts. First, consider the lower mantle where the response kernel is non-negligible for only the smallest degrees. At $l = 2$, density anomalies between 1500 km depth and the core-mantle boundary generate 179 ± 63 m of dynamic topography. This value matches our observations and suggests that the lower mantle contributes modestly to dynamic topography[41]. At $l = 2$, positive lower mantle density anomalies generate geoid anomalies of -31 ± 10 m, which agrees with the observed geoid[4]. Since response kernels for $l = 8$–30 in the lower mantle are nearly zero, short-wavelength density anomalies at these depths cannot generate either surface deformation or geoid anomalies.

We now turn our attention to the upper half of the mantle where the shear wave spectrum is dominated by long wavelengths (Figure 6f). If inferred density anomalies are predominantly at

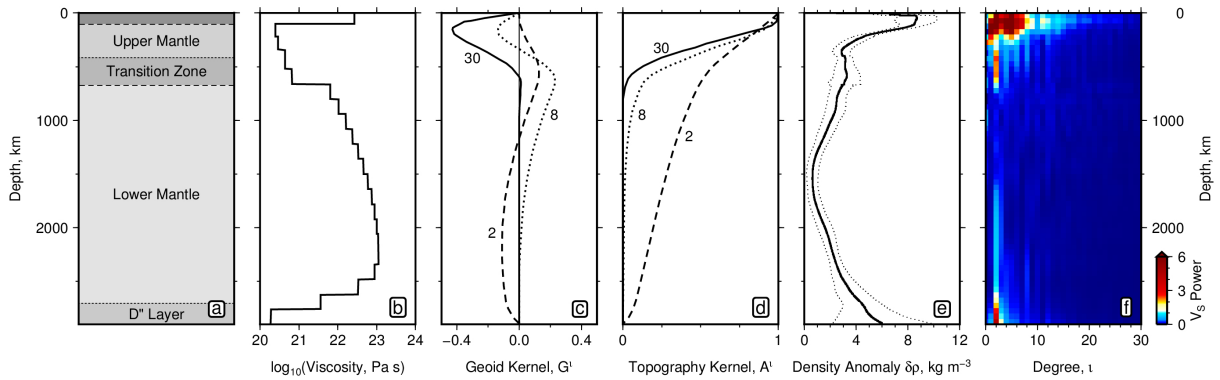

Figure 6: Viscosity, velocity and density structure of mantle. (a) Schematic mantle structure as function of depth. D" refers to a layer of variable thickness located at the boundary between the core and mantle. (b) Radial viscosity structure[38]. (c) Normalised geoid kernels and (d) normalised surface deformation kernels, calculated from radial viscosity structure shown in (b), for $l = 2$, 8 and 30[38]. (e) Average radial density anomaly relative to PREM, calculated from a set of six shear wave tomographic models[39]. Dotted lines = one standard deviation. (f) Power of shear wave velocity anomalies as function of depth and degree for S40RTS tomography model[40].

$l = 2$, the amplitude of calculated dynamic topography is 1.36 ± 0.29 km. Note that many predictive models omit the outer ~ 300 km of the mantle and lithosphere[10]. This omission reduces the amplitude of calculated dynamic topography to 0.48 ± 0.13 km at $l = 2$. There are three reasons for omitting the uppermost mantle. First, the density of crossing rays is greatly reduced near the Earth's surface, smearing out body wave tomographic models. Secondly, compositional variations beneath mid-oceanic ridges and within the continental lithosphere complicate this velocity-to-density conversion. Thirdly, the value of the surface response kernel, $A^l(r)$, rapidly approaches unity, leading to unrealistically large values of dynamic topography. If, instead, the upper mantle is dominated by density anomalies of $l = 30$, the predicted dynamic topography is 0.86 ± 0.14 km with a negligible geoid anomaly, in close agreement with our observed dynamic topography and with geoid anomalies. A simple way of resolving the discrepancy is to infer $l = 30$ density anomalies within the upper half of the mantle and $l = 2$ anomalies within the lower half. In this instance, the $l = 2$ component of dynamic topography is 179 ± 63 m and the $l = 30$ component is 864 ± 142 m. Thus distributing density anomalies at low degrees in the lower mantle and at higher degrees in the upper mantle better matches both the geoid and observed dynamic topography. This bimodal distribution may also explain why negative admittance is so rarely observed on Earth (Figure 2 from Colli et al.[32]).

The existence of significant observed power at $l = 10$–30 underlines the importance of shallow, short-wavelength mantle density structure, which is supported by independent observations[42]. Beneath the North Atlantic Ocean, a 150 ± 50 km low velocity layer has been seismically imaged[43,44]. Short-wavelength temperature perturbations generated within a major convective upwelling centred beneath Iceland flow radially within this layer[45,46]. Globally, there is increasing seismic and geochemical evidence for sub-plate asthenospheric channels[44,47,48,49]. To generate dynamic topography, the required temperature perturbation, ΔT, within a channel is given by

$$\Delta T = \frac{U\,(1 - \alpha T_\circ)}{h\alpha} \tag{3}$$

where U is the air-loaded dynamic topography in km, $\alpha = 3.3 \times 10^{-5}$ °C^{-1} is the thermal expansion coefficient, $T_\circ = 1300°$ C is the background temperature of the asthenosphere,

and h km is the channel thickness (Supplementary Information)[46]. The amplitude of water-loaded dynamic topography is ± 1 km which represents an air-loaded equivalent of ± 0.7 km. If $h = 150 \pm 50$ km, we obtain $\Delta T \sim 150 \pm 50\,^{\circ}$C, consistent with the range of asthenospheric temperatures inferred from geochemical analysis of basaltic rocks at mid-oceanic ridges, from oceanic crustal thicknesses, and from convective circulation models[18,49,50,51].

Implications for Mantle Dynamics and Surface Systems

We present a new and comprehensive global database of oceanic residual depth measurements which was carefully constructed by analysing substantial inventories of seismic reflection, modern wide-angle and legacy refraction profiles. Residual depth anomalies have amplitudes of ± 1 km and wavelengths of 10^3 km. We combined our database of residual depths with sparser continental constraints to build a globally continuous model. Spectral analysis shows there is one order of magnitude less power at the longest wavelengths and significantly more power at shorter wavelengths than suggested by existing predictive models. This discrepancy holds true when only the most robust observations from the oceanic realm alone are analysed.

Our new results have two significant implications. First, it is likely that shallow mantle convection exerts a significant role in generating and maintaining dynamic topography. An important corollary is that existing global seismic tomographic models of the upper mantle do not currently resolve short-wavelength density anomalies. Secondly, the ubiquity of observed short-wavelength dynamic topography implies that the planform of mantle convection evolves more rapidly than previously imagined.

Our observations provide new constraints for calculating mantle density and viscosity structure that will have an immediate impact on studies concerning mantle fluid dynamics (e.g. glacial-isostatic adjustment, true polar wander). Furthermore, transient vertical motions on short length and timescales have profound consequences for subjects as diverse as the reconstruction of ancient oceanic currents, long-term climate, fluvial geomorphology and sedimentary routing systems.

Methods

Residual Depth Calculation

Residual depth, z_r, is the difference between the expected depth to water-loaded oceanic basement, z_w, obtained from age-depth analysis of oceanic lithosphere unaffected by dynamic topography, and the observed depth to oceanic basement, z_o[15]. Thus

$$z_r = z_w - z_o - C_s - C_c \tag{4}$$

where C_s and C_c are sedimentary and crustal loading corrections, respectively.

Age-Depth Analysis

z_w is obtained from a global age-depth analysis of oceanic lithosphere unaffected by dynamic topography[22]. Long-wavelength free-air gravity anomalies and ship-track bathymetric inventories were used to identify and remove regions where significant positive and negative dynamic topography occurs and where oceanic crust is anomalously thick or thin[14]. This relationship has been revised to remove sharp discontinuities and to account for the effects of cooling by hydrothermal circulation at mid-oceanic ridges.

$$z_w(t) = \begin{cases} 2850 & 0 \leq t < 1 \\ 2652 + 324\sqrt{t} & 1 \leq t \leq 73 \\ 5028 + 5.26t - 250 \sin\left(\frac{t-75}{30}\right) & 73 < t \leq 156 \\ 5750 & t > 156 \end{cases} \tag{5}$$

where t is the plate age in millions of years and z_w is the water-loaded depth to top of oceanic basement in metres. In addition to exploiting the age-depth relationship shown in Equation (5), we have also tested previously published age-depth relationships as well as both half-space cooling and plate models calculated directly from our observational database (Supplementary Information).

Sedimentary and Crustal Corrections

Variable sedimentary loads are converted into equivalent water loads using

$$C_s = \left(\frac{\rho_a - \overline{\rho}_s}{\rho_a - \rho_w}\right) z_s \tag{6}$$

where z_s is the thickness of the sedimentary layer, $\rho_a = 3.20 \pm 0.02$ Mg m^{-3} is the density of asthenosphere, $\overline{\rho}_s$ is the average density of the sedimentary layer, and $\rho_w = 1.03 \pm 0.01$ Mg m^{-3} is the density of water. In the absence of borehole penetrations, z_s and $\overline{\rho}_s$ are calculated from measurements of the two-way travel time of the sedimentary layer, t_s, using a global empirical database assembled from seismic reflection and wide-angle datasets shown in Figure 1a.

Sedimentary porosity, $\phi(z_s)$, is assumed to vary as a function of z_s according to

$$\phi(z_s) = \phi_\circ \exp\left(\frac{-z_s}{\lambda}\right) \tag{7}$$

where $\phi_\circ$ and λ are the initial porosity and compaction decay length, respectively. The sonic velocity of the sedimentary layer, v, is given by

$$\frac{1}{v} = \frac{\phi}{v_w} + \frac{1-\phi}{v_{sg}} \tag{8}$$

where $v_{sg} = 5.50 \pm 0.50$ km s^{-1} is the velocity of solid quartz grains and $v_w = 1.50 \pm 0.01$ km s^{-1} is the velocity of water. It is straightforward to determine the relationship between t_s and z_s so that

$$\frac{t_s}{2} = \frac{z_s}{v_{sg}} + \phi_\circ \lambda \left(\frac{1}{v_w} - \frac{1}{v_{sg}} \right) \left[1 - \exp\left(\frac{-z_s}{\lambda} \right) \right] \tag{9}$$

The best fit between Equation 9 and the global empirical database is obtained for $\phi_\circ = 0.6 \pm 0.1$ and $\lambda = 3.9 \pm 1.1$ km for $v_{sg} = 5.50$ km s^{-1}. A *Monte Carlo* approach can be used to investigate how uncertainties in $\phi_\circ$, λ, and v_{sg} propagate into uncertainties in C_s. The value of $\overline{\rho}_s$ is given by

$$\overline{\rho}_s(z_s) = \rho_{sg} + \frac{\phi_\circ \lambda}{z_s} (\rho_w - \rho_{sg}) \left[1 - \exp\left(\frac{-z_s}{\lambda} \right) \right] \tag{10}$$

where $\rho_{sg} = 2.65 \pm 0.05$ Mg m^{-3} is the density of solid quartz grains. This empirical approach enables z_s, $\overline{\rho}_s$ and C_s to be estimated for each seismic reflection image.

A smaller crustal correction, C_c, is estimated in two steps. First, two-way travel time is converted into crustal thickness, z_c, using an average crustal velocity of $\overline{v}_c = 6.28 \pm 0.34$ km s^{-1}. Secondly, z_c is normalised to the global average value of 7.1 km[18]. This yields

$$C_c = \left(\frac{\rho_a - \overline{\rho}_c}{\rho_a - \rho_w} \right) (z_c - 7.1) \tag{11}$$

where $\overline{\rho}_c = 2.86 \pm 0.03$ Mg m^{-3} is the average crustal density.

Spherical Harmonic Analysis

The observational database consists of spot measurements of dynamic topography, d_i, at a set of colatitudes, θ_i, and longitudes, φ_i, for $i = 1, \ldots, N$. It is assumed that these data are subject to zero-mean, uncorrelated, Gaussian random errors where variance of the ith datum is σ_i^2.

To investigate the spectral properties of this database, we seek an interpolating function, $f(\theta, \varphi)$, taking the form

$$f(\theta, \varphi) = \sum_{l=1}^{L} \sum_{m=-l}^{l} f_{lm} \, \mathcal{Y}_{lm}(\theta, \varphi) \tag{12}$$

such that $f(\theta_i, \varphi_i) \approx d_i$ at each spot measurement. Here, the $\mathcal{Y}_{lm}$ are fully normalised real spherical harmonics where l is the degree and m is the order. L is the maximum spherical harmonic degree used in the expansion. We note that degree-zero contributions to the interpolating function have been excluded in accordance with physical constraints on dynamic topography. Given this interpolating function, the associated power at each value of l is given by

$$P_l = \sum_{m=-l}^{l} f_{lm}^2 \tag{13}$$

To determine the appropriate expansion coefficients, f_{lm}, in Equation (12), we use a regularised least squares misfit

$$J = \frac{1}{2}\sum_{i=1}^{N}\frac{1}{\sigma_i^2}\left[f(\theta_i,\varphi_i) - d_i\right]^2 + \frac{1}{2}\int_{\mathbb{S}^2}\left[\lambda_1\|\nabla_1 f\|^2 + \lambda_2 f^2\right]\,\mathrm{d}S \tag{14}$$

where λ_1 and λ_2 are non-negative weighting factors, $\mathbb{S}^2$ denotes the unit two-sphere, and ∇_1 is the tangential gradient operator. The first term on the right-hand side of Equation (14) is proportional to

$$\chi^2 = \frac{1}{N}\sum_{i=1}^{N}\frac{1}{\sigma_i^2}[f(\theta_i,\varphi_i) - d_i]^2 \tag{15}$$

which determines how well the interpolating function fits observations. The second term acts to regularise the problem towards smooth interpolating functions and the third term damps the average amplitude of the model. In the absence of regularisation, the least squares problem has a unique solution only when there are more data points than expansion coefficients. However, by under-parameterising we could potentially neglect geologically significant short-wavelength features. Instead, it is preferable to exploit a combination of gradient regularisation to remove spurious short-wavelength features and amplitude damping to maintain realistic values of dynamic topography in unconstrained regions. In practice, this amplitude damping is only important beneath the excised Himalayan orogenic belt.

To obtain a set of expansion coefficients, f_{lm}, that minimise J in Equation (14), we set

$$\frac{\partial J}{\partial f_{lm}} = 0 \tag{16}$$

for all appropriate values of l and m. This constraint leads to a system of linear equations that can be written as

$$(\mathbf{A}^T\mathbf{C}^{-1}\mathbf{A} + \lambda_1\mathbf{R} + \lambda_2\mathbf{I})\mathbf{m} = \mathbf{A}^T\mathbf{C}^{-1}\mathbf{d} \tag{17}$$

There is a unique solution if $\lambda_1 > 0$ or $\lambda_2 > 0$. $\mathbf{m}$ is a vector containing the $M = (L+1)^2 - 1$ expansion coefficients where

$$\mathbf{m} = \begin{pmatrix} f_{1\,-1} \\ \vdots \\ f_{L\,L} \end{pmatrix} \tag{18}$$

and $\mathbf{d}$ is an N-dimensional vector containing the data where

$$\mathbf{d} = \begin{pmatrix} d_1 \\ \vdots \\ d_N \end{pmatrix} \tag{19}$$

$\mathbf{A}$ is an $N \times M$ matrix given by

$$\mathbf{A} = \begin{pmatrix} \mathcal{Y}_{1\,-1}(\theta_1,\varphi_1) & \cdots & \mathcal{Y}_{L\,L}(\theta_1,\varphi_1) \\ \vdots & \ddots & \vdots \\ \mathcal{Y}_{1\,-1}(\theta_N,\varphi_N) & \cdots & \mathcal{Y}_{L\,L}(\theta_N,\varphi_N) \end{pmatrix} \tag{20}$$

$\mathbf{C} = \mathrm{diag}(\sigma_1^2,\ldots,\sigma_N^2)$ is the covariance matrix and $\mathbf{I}$ is the identity matrix. $\mathbf{R}$ is an $M \times M$ matrix associated with gradient regularisation which is diagonal with components

$$R_{lml'm'} = l(l+1)\delta_{ll'}\delta_{mm'} \tag{21}$$

where $\delta_{ll'}$ is the Kronecker delta.

Data and Code Sources

The oceanic residual depth measurements are tabulated in the Supplementary Information and available online. Seismic reflection surveys can be requested from ION. Isostatic and spherical harmonic inversion codes are available on request from
`ftp://www.bullard.esc.cam.ac.uk/pub/incoming/mjh217`.

References

[1] Pekeris, C. L. Thermal Convection in the Interior of the Earth. *Geophysical Supplements to the Monthly Notices of the Royal Astronomical Society* **3**, 343–367 (1935).

[2] Turcotte, D. L. & Schubert, G. *Geodynamics* (Cambridge University Press, Cambridge, 2002), 2nd edn.

[3] Richards, M. A. & Hager, B. H. Geoid Anomalies in a Dynamic Earth. *Journal of Geophysical Research* **89**, 5987–6002 (1984).

[4] Hager, B. H., Clayton, R. W. & Richards, M. A. Lower mantle heterogeneity, dynamic topography and the geoid. *Nature* **313**, 541–545 (1985).

[5] Schuberth, B. S. A. & Bunge, H. P. Tomographic filtering of high-resolution mantle circulation models: Can seismic heterogeneity be explained by temperature alone? *Geochemistry, Geophysics, Geosystems* **10**, 5 (2009).

[6] Davies, D. R. *et al.* Reconciling dynamic and seismic models of Earth's lower mantle: The dominant role of thermal heterogeneity. *Earth and Planetary Science Letters* **353-354**, 253–269 (2012).

[7] Steinberger, B. Effects of latent heat release at phase boundaries on flow in the Earths mantle, phase boundary topography and dynamic topography at the Earths surface. *Physics of the Earth and Planetary Interiors* **164**, 2–20 (2007).

[8] Conrad, C. P. & Husson, L. Influence of dynamic topography on sea level and its rate of change. *Lithosphere* **1**, 110–120 (2009).

[9] Ricard, Y., Richards, M. A., Lithgow-Bertelloni, C. & Le Stunff, Y. A Geodynamic Model of Mantle Density Heterogeneity. *Journal of Geophysical Research* **98**, 21,895–21,909 (1993).

[10] Flament, N., Gurnis, M. & Müller, R. D. A review of observations and models of dynamic topography. *Lithosphere* **5**, 189–210 (2013).

[11] Moucha, R. *et al.* Dynamic topography and long-term sea-level variations: There is no such thing as a stable continental platform. *Earth and Planetary Science Letters* **271**, 101–108 (2008).

[12] Bunge, H. P., Hagelberg, C. R. & Travis, B. J. Mantle circulation models with variational data assimilation: Inferring past mantle flow and structure from plate motion histories and seismic tomography. *Geophysical Journal International* **152**, 280–301 (2003).

[13] Spasojević, S. & Gurnis, M. Sea level and vertical motion of continents from dynamic earth models since the Late Cretaceous. *AAPG Bulletin* **96**, 2037–2064 (2012).

[14] Crosby, A. G., McKenzie, D. P. & Sclater, J. G. The relationship between depth, age and gravity in the oceans. *Geophysical Journal International* **166**, 553–573 (2006).

[15] Menard, H. W. Depth Anomalies and the Bobbing Motion of Drifting Islands. *Journal of Geophysical Research* **78**, 5128–5137 (1973).

[16] McKenzie, D. P. The influence of dynamically supported topography on estimates of Te. *Earth and Planetary Science Letters* **295**, 127–138 (2010).

[17] Müller, R. D., Sdrolias, M., Gaina, C. & Roest, W. R. Age, spreading rates, and spreading asymmetry of the world's ocean crust. *Geochemistry, Geophysics, Geosystems* **9**, 4 (2008).

[18] White, R. S., McKenzie, D. P. & O'Nions, R. K. Oceanic Crustal Thickness From Seismic Measurements and Rare Earth Element Inversions. *Journal of Geophysical Research* **97**, 19,683–19,715 (1992).

[19] Winterbourne, J. R., Crosby, A. G. & White, N. J. Depth, age and dynamic topography of oceanic lithosphere beneath heavily sedimented Atlantic margins. *Earth and Planetary Science Letters* **287**, 137–151 (2009).

[20] Czarnota, K., Hoggard, M. J., White, N. J. & Winterbourne, J. Spatial and temporal patterns of Cenozoic dynamic topography around Australia. *Geochemistry, Geophysics, Geosystems* **14**, 634–658 (2013).

[21] Winterbourne, J. R., White, N. J. & Crosby, A. G. Accurate measurements of residual topography from the oceanic realm. *Tectonics* **33**, 1–34 (2014).

[22] Crosby, A. G. & McKenzie, D. P. An analysis of young ocean depth, gravity and global residual topography. *Geophysical Journal International* **178**, 1198–1219 (2009).

[23] Hohertz, W. L. & Carlson, R. L. An independent test of thermal subsidence and asthenosphere flow beneath the Argentine Basin. *Earth and Planetary Science Letters* **161**, 73–83 (1998).

[24] Jackson, M. P. A., Hudec, M. R. & Hegarty, K. A. The great West African Tertiary coastal uplift: Fact or fiction? A perspective from the Angolan divergent margin. *Tectonics* **24**, TC6014 (2005).

[25] Guiraud, M., Buta-Neto, A. & Quesne, D. Segmentation and differential post-rift uplift at the Angola margin as recorded by the transform-rifted Benguela and oblique-to-orthogonal-rifted Kwanza basins. *Marine and Petroleum Geology* **27**, 1040–1068 (2010).

[26] Roberts, G. G. & White, N. J. Estimating uplift rate histories from river profiles using African examples. *Journal of Geophysical Research* **115**, B02406 (2010).

[27] Smith, W. H. F. & Sandwell, D. T. Global Sea Floor Topography from Satellite Altimetry and Ship Depth Soundings. *Science* **277**, 1956–1962 (1997).

[28] Divins, D. L. Total Sediment Thickness of the World's Oceans & Marginal Seas, NOAA National Geophysical Data Center, Boulder, CO (2003).

[29] Laske, G. & Masters, G. A Global Digital Map of Sediment Thickness, EOS Trans. AGU, 78, F483 (1997).

[30] Jordan, T. H. The Continental Tectosphere. *Reviews of Geophysics* **13**, 1–12 (1975).

[31] Tapley, B. *et al.* The GGM03 Mean Earth Gravity Model from GRACE; Eos Trans. AGU 88(52), Fall Meet. Suppl., Abstract G42A-03 (2007).

[32] Colli, L., Ghelichkhan, S. & Bunge, H.-P. On the ratio of dynamic topography and gravity anomalies in a dynamic Earth. *Geophysical Research Letters* **43** (2016).

[33] Wilson, J. W. P., Roberts, G. G., Hoggard, M. J. & White, N. J. Cenozoic epeirogeny of the Arabian Peninsula from drainage modeling. *Geochemistry, Geophysics, Geosystems* **15**, 3723–3761 (2014).

[34] Stephenson, S. N., Roberts, G. G., Hoggard, M. J. & Whittaker, A. C. A Cenozoic uplift history of Mexico and its surroundings from longitudinal river profiles. *Geochemistry, Geophysics, Geosystems* **15**, 4734–4758 (2014).

[35] Czarnota, K., Roberts, G. G., White, N. J. & Fishwick, S. Spatial and temporal patterns of Australian dynamic topography from river profile modeling. *Journal of Geophysical Research: Solid Earth* **119**, 1384–1424 (2014).

[36] Priestley, K. & McKenzie, D. P. The relationship between shear wave velocity, temperature, attenuation and viscosity in the shallow part of the mantle. *Earth and Planetary Science Letters* **381**, 78–91 (2013).

[37] Hager, B. H. & Richards, M. A. Long-Wavelength Variations in Earth's Geoid: Physical Models and Dynamical Implications. *Philosophical Transactions of the Royal Society A: Mathematical, Physical and Engineering Sciences* **328**, 309–327 (1989).

[38] Steinberger, B., Werner, S. C. & Torsvik, T. H. Deep versus shallow origin of gravity anomalies, topography and volcanism on Earth, Venus and Mars. *Icarus* **207**, 564–577 (2010).

[39] Forte, A. M. Constraints on Seismic Models from Other Disciplines - Implications for Mantle Dynamics and Composition. *Treatise on Geophysics* 805–858 (2007).

[40] Ritsema, J., Deuss, A., van Heijst, H. J. & Woodhouse, J. H. S40RTS: a degree-40 shear-velocity model for the mantle from new Rayleigh wave dispersion, teleseismic traveltime and normal-mode splitting function measurements. *Geophysical Journal International* **184**, 1223–1236 (2011).

[41] Cazenave, A., Souriau, A. & Dominh, K. Global coupling of Earth surface topography with hotspots, geoid and mantle heterogeneities. *Nature* **340**, 54–57 (1989).

[42] Wen, L. & Anderson, D. L. Layered mantle convection: A model for geoid and topography. *Earth and Planetary Science Letters* **146**, 367–377 (1997).

[43] Delorey, A. A., Dunn, R. A. & Gaherty, J. B. Surface wave tomography of the upper mantle beneath the Reykjanes Ridge with implications for ridgehot spot interaction. *Journal of Geophysical Research* **112**, B08313 (2007).

[44] Rickers, F., Fichtner, A. & Trampert, J. The Iceland-Jan Mayen plume system and its impact on mantle dynamics in the North Atlantic region: Evidence from full-waveform inversion. *Earth and Planetary Science Letters* **367**, 39–51 (2013).

[45] Yale, M. M. & Morgan, J. P. Asthenosphere flow model of hotspot-ridge interactions: A comparison of Iceland and Kerguelen. *Earth and Planetary Science Letters* **161**, 45–56 (1998).

[46] Hartley, R. A., Roberts, G. G., White, N. & Richardson, C. Transient convective uplift of an ancient buried landscape. *Nature Geoscience* **4**, 562–565 (2011).

[47] Fichtner, A., Kennett, B. L. N., Igel, H. & Bunge, H.-P. Full seismic waveform tomography for upper-mantle structure in the Australasian region using adjoint methods. *Geophysical Journal International* **179**, 1703–1725 (2009).

[48] French, S., Lekic, V. & Romanowicz, B. Waveform Tomography Reveals Channeled Flow at the Base of the Oceanic Asthenosphere. *Science* **342**, 227–231 (2013).

[49] Dalton, C. A., Langmuir, C. H. & Gale, A. Geophysical and Geochemical Evidence for Deep Temperature Variations Beneath Mid-Ocean Ridges. *Science* **344**, 80–83 (2014).

[50] Buck, W. R., Small, C. & Ryan, W. B. F. Constraints on asthenospheric flow from the depths of oceanic spreading centers: The East Pacific Rise and the Australian-Antarctic discordance. *Geochemistry, Geophysics, Geosystems* **10** (2009).

[51] Weismüller, J. *et al.* Fast asthenosphere motion in high-resolution global mantle flow models. *Geophysical Research Letters* **42**, 7,429–7,435 (2015).

[52] Parsons, B. & Sclater, J. G. An analysis of the variation of ocean floor bathymetry and heat flow with age. *Journal of Geophysical Research* **82**, 803–827 (1977).

[53] Stein, C. & Stein, S. A model for the global variation in oceanic depth and heat flow with lithospheric age. *Nature* **359**, 123–139 (1992).

[54] Laske, G., Masters, G., Ma, Z. & Pasyanos, M. Update on CRUST1.0 - A 1-degree Global Model of Earth's Crust. *Geophysical Research Abstracts, 15, Abstract EGU2013-2658* (2013).

[55] Lago, B. & Rabinowicz, M. Admittance for a convection in a layered spherical shell. *Geophysical Journal of the Royal Astonomical Society* **77**, 461–482 (1984).

[56] Revenaugh, J. & Parsons, B. Dynamic topography and gravity anomalies for fluid layers whose viscosity varies exponentially with depth. *Geophysical Journal International* **90**, 349–368 (1987).

[57] Molnar, P., England, P. C. & Jones, C. H. Mantle dynamics, isostasy, and the support of high terrain. *Journal of Geophysical Research: Solid Earth* **120**, 1,932–1,957 (2015).

[58] Lambeck, K. Aristoteles : An ESA Mission to Study the Earth's Gravity Field. *ESA Journal* **14**, 14 (1990).

[59] Kaula, W. M. *Theorey of Satellite Geodesy* (Blaisdell Publishing Company, Waltham, Massachusetts, 1966).

[60] Courtillot, V., Davaille, A., Besse, J. & Stock, J. Three distinct types of hotspots in the Earths mantle. *Earth and Planetary Science Letters* **205**, 295–308 (2003).

[61] Bevier, M. L., Armstrong, R. L. & Souther, J. G. Miocene peralkaline volcanism in west-central British Columbia - Its temporal and place-tectonics setting. *Geology* **7**, 389–392 (1979).

[62] Innocenti, F. *et al.* Neogene and Quaternary volcanism in Western Anatolia: Magma sources and geodynamic evolution. *Marine Geology* **221**, 397–421 (2005).

[63] Bardintzeff, J. M., Liégeois, J. P., Bonin, B., Bellon, H. & Rasamimanana, G. Madagascar volcanic provinces linked to the Gondwana break-up: Geochemical and isotopic evidences for contrasting mantle sources. *Gondwana Research* **18**, 295–314 (2010).

[64] Whitehead, P. W. *et al.* Temporal development of the Atherton Basalt Province, north Queensland. *Australian Journal of Earth Sciences* **54**, 691–709 (2007).

[65] Knesel, K. M., Souza, Z. S., Vasconcelos, P. M., Cohen, B. E. & Silveira, F. V. Young volcanism in the Borborema Province, NE Brazil, shows no evidence for a trace of the Fernando de Noronha plume on the continent. *Earth and Planetary Science Letters* **302**, 38–50 (2011).

[66] Vasconcelos, P. M., Knesel, K. M., Cohen, B. E. & Heim, J. A. Geochronology of the Australian Cenozoic: a history of tectonic and igneous activity, weathering, erosion, and sedimentation. *Australian Journal of Earth Sciences* **55**, 865–914 (2008).

[67] Maund, J. G., Rex, D. C., Le Roex, a. P. & Reid, D. L. Volcanism on Gough Island: a revised stratigraphy. *Geological Magazine* **125**, 175–181 (1988).

[68] Barling, J., Goldstein, S. L. & Nicholls, I. A. Geochemistry of Heard Island (Southern Indian Ocean): Characterization of an enriched mantle component and implications for enrichment of the sub-Indian ocean mantle. *Journal of Petrology* **35**, 1017–1053 (1994).

[69] Cucciniello, C. *et al.* New 40Ar-39Ar ages and petrogenesis of the Massif d'Ambre volcano, northern Madagascar. *Geological Society of America Special Papers* **478**, 257–281 (2011).

[70] Camp, V. E. & Roobol, M. J. Upwelling asthenosphere beneath western Arabia and its regional implications. *Journal of Geophysical Research* **97**, 15,255–15,271 (1992).

[71] Macpherson, C. G. *et al.* Plio-Pleistocene intra-plate magmatism from the southern Sulu Arc, Semporna peninsula, Sabah, Borneo: Implications for high-Nb basalt in subduction zones. *Journal of Volcanology and Geothermal Research* **190**, 25–38 (2010).

[72] Ferrari, L., Valencia-Moreno, M. & Bryan, S. Magmatism and tectonics of the Sierra Madre Occidental and its relation with the evolution of the western margin of North America. *Geological Society of America Special Paper* **422** (2007).

[73] Johnson, K. T. M. *et al.* Boomerang Seamount: The active expression of the Amsterdam-St. Paul hotspot, Southeast India Ridge. *Earth and Planetary Science Letters* **183**, 245–259 (2000).

[74] Irving, A. J. & Green, D. H. Geochemistry and petrogenesis of the newer basalts of Victoria and South Australia. *Journal of the Geological Society of Australia* **23**, 45–66 (1976).

Correspondence

Correspondence and requests for materials should be addressed to M.J. Hoggard and N. White.

Acknowledgements

This research was supported by a BP-Cambridge collaboration. We are grateful to ION for permission to publish partial seismic reflection profiles shown in Figure 2 from their IndiaSPAN™ and Greater BrasilSPAN™ datasets. We thank J. Austermann, P. Bellingham, J. Braun, R. Buck, A. Bump, H-P. Bunge, R. Corfield, A. Crosby, K. Czarnota, M. Falder, A. Forte, I. Frame, S. Ghelichkhan, D. Glassey, T. Heyn, B. Horn, S. Kisin, D. Lyness, L. Mackay, K. McDermott, D. McKenzie, R. Parnell-Turner, F. Richards, G. Roberts, B. Schuberth, B. Steinberger, E. Stirling, M. Thompson, J. Weismüller, J. Wilson and J. Winterbourne for their help. Figures were prepared using Generic Mapping Tools and routines from the SHTOOLS package were used in the spherical harmonic analysis. Earth Sciences contribution esc.3605.

Author Contributions

This project was conceived and managed by NW. MJH processed, interpreted and modelled the databases with guidance from NW and DA-A. The paper was written by all three authors.

Additional Information

Data and synthetic tests reported in this paper are tabulated in the Supplementary Information.

Competing Financial Interests

The authors declare no competing financial interests.

Supplementary Information

Exclusion Polygons

A sufficiently accurate grid of crustal thickness throughout the oceanic realm is not yet available. As a result, residual topographic estimates determined from ship-track observations are not isostatically corrected for anomalous crustal thickness. This shortcoming means that it is essential to manually and conservatively excise all regions where anomalously thick or thin oceanic crust occurs, using high resolution bathymetric and gravity anomaly maps. The resultant exclusion polygons are shown in Figure 7a.

On the continents, we have estimated dynamic topography by scaling long-wavelength free-air gravity anomalies using a constant admittance of $+50$ mGal km^{-1}. It is important to excise all regions where gravity anomalies are affected by active/ancient orogenic belts and by flexure at subduction zones. We used a combination of gravity, topographic and geological maps to manually excise these regions. The resultant exclusion polygons are shown in Figure 7b.

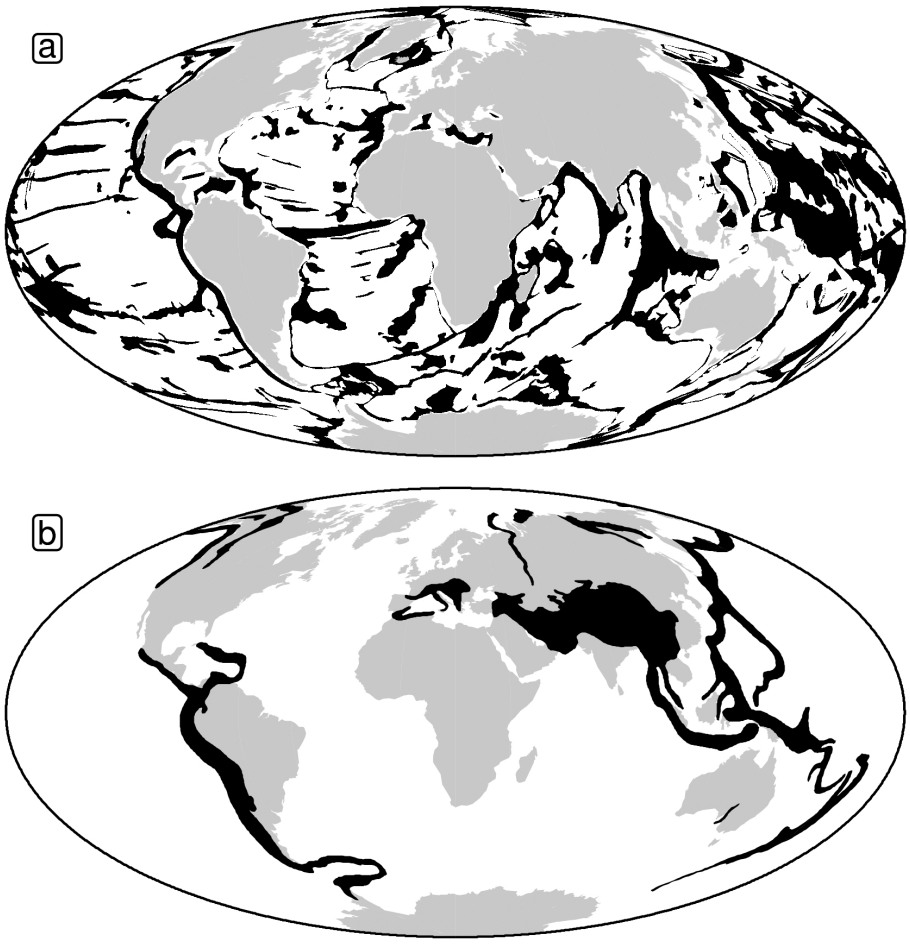

Figure 7: Exclusion polygons. (a) Distribution of exclusion polygons within oceanic realm that were used to excise regions of anomalously thick or thin oceanic crust from residual topographic measurements derived from ship-track database. (b) Distribution of exclusion polygons that were used to excise orogenic and flexural zones from maps of long-wavelength gravity anomalies.

Alternative Age-Depth Relationships

To demonstrate the robustness of the power spectrum of observed dynamic topography shown in Figure 5b, we recalculated oceanic residual topography from spot measurements and ship-track observations using alternative age-depth relationships (Figure 8a). First, we calculated residual topography using the well-known plate cooling models of Parsons and Sclater[52] and Stein and Stein[53]. Secondly, we fitted a new plate cooling model by minimising the misfit between this model and spot measurements from the oceanic realm. Thirdly, we fitted a half-space (i.e. $\sqrt{t}$) cooling model using the same approach. Finally, we fitted a different half-space cooling model to only observations from oceanic floor younger than 70 Ma. We then extrapolated this relationship to older ages. This extreme approach implies that seafloor flattening could conceivably make a significant contribution to long-wavelength dynamic topography. However, all calculated power spectra are in close agreement with our previous results (Figure 8b).

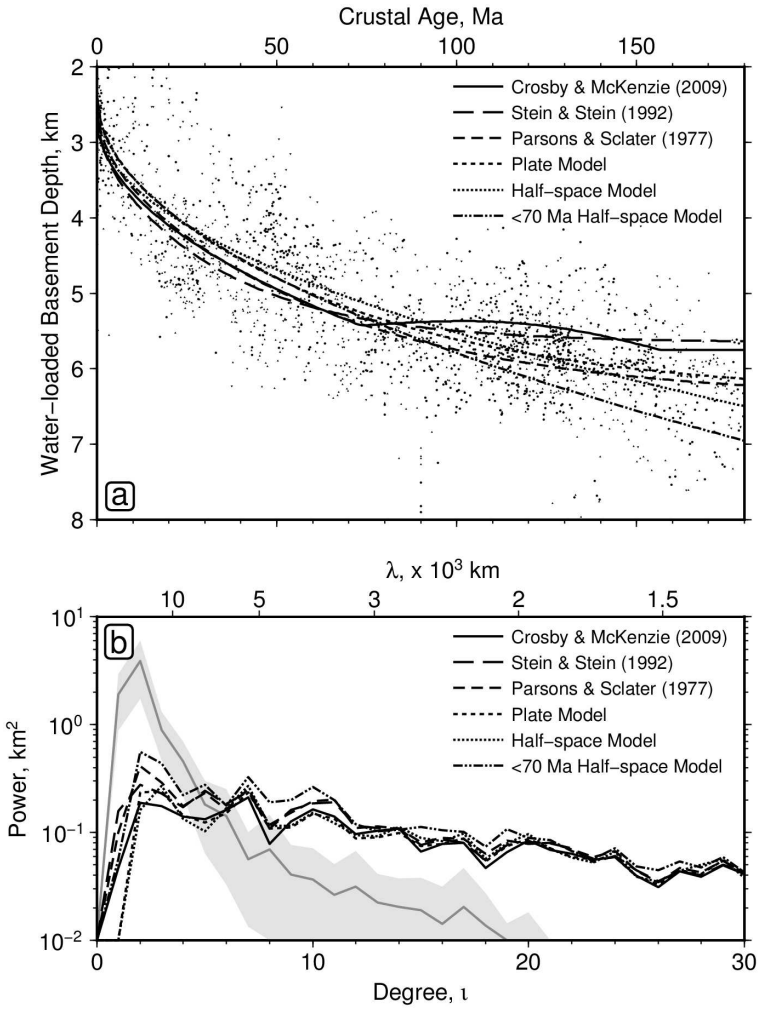

Figure 8: Alternative age-depth relationships. (a) Solid points = 2,120 measurements of water-loaded depth to oceanic basement as function of plate age; solid/dashed lines = age-depth relationships[22,52,53]; dotted lines = calculated plate and half-space cooling models. (b) Power spectra of observed dynamic topography using four different age-depth relationships. Grey line/bounds = mean/standard deviation of the five predictive dynamic topography models.

Continental Dynamic Topography

We have carried out a series of tests which check how different methods for calculating dynamic topography on the continents affect our observed power spectrum shown in Figure 5b. In the first pair of tests, we have completely excised the continents and calculated power spectra using oceanic observations alone. One of these tests includes all oceanic observations (i.e. spot measurements and edited ship-track data) and the other test includes only the most reliable oceanic observations (i.e. 2,120 spot measurements alone). Calculated power spectra are in close agreement (Figure 9a). Thus excision of gravity-derived continental estimates and oceanic ship-track data does not significantly alter our substantive result concerning the discrepancies between observed and predicted spectra.

In a second set of tests, we calculated continental dynamic topography using the CRUST1.0 digital grid of Laske et al.[54]. Their grid was first re-sampled at continental nodes that are identical to those shown in Figure 1b. Dynamic topography was calculated at each node using an isostatic balance between the thickness and density structure of crust taken from CRUST1.0 and the structure of an unperturbed mid-oceanic ridge. The related issue of lithospheric thickness and density was addressed in three different ways. First, we assumed that continental lithosphere had a constant thickness everywhere of 125 km. Secondly, we assumed that lithospheric thickness varied in accordance with the surface wave tomographic model estimates of Priestley and McKenzie[36]. Thirdly, we incorporated the effects of chemical depletion (i.e. the existence of harzburgitic lithospheric mantle in cratonic regions) by reducing the average density of lithospheric mantle that is thicker than 175 km by 10 and 30 kg m^{-3}.

The four resultant power spectra are shown in Figure 9b. Our series of tests show that spectral power at $l = 2$ remains an order of magnitude smaller than that of predictive models. Similarly, spectral power at $l = 20$–30 remains significant. In each case, spectral slopes match that obtained using long-wavelength free-air gravity anomalies. There is greater spectral power at all degrees since the amplitude of continental dynamic topography predicted by CRUST 1.0 is much greater than that observed within the oceanic realm. For example, the test which uses constant lithospheric thickness has air-loaded dynamic topographic peaks of ± 3.5 km. Given observed peak water-loaded oceanic residual depth anomalies are ± 2.5 km, we might expect equivalent air-loaded values of only ± 1.7 km. Inclusion of variable lithospheric thickness reduces both amplitude and spectral power of continental dynamic topography. However, if significant depletion is permitted within thicker cratonic regions, the buoyancy contribution of thick lithosphere is essentially cancelled out due to the isopycnal effect.

There are two significant drawbacks in exploiting CRUST1.0. First, a feature of this (and other) digital databases is that the original raw input data is not provided, which means that the fidelity of the CRUST1.0 database cannot be verified or assessed. It is constructed from a variety of data sources whose resolution and accuracy is variable. It is also extrapolated away from actual measurements into regions where data coverage is either poor or non-existent. Secondly, the amplitude of dynamic topography from CRUST 1.0 on its own is geologically implausible. It is essential to include the buoyancy effects associated with variable lithospheric thickness — a correction that is clearly of paramount importance in the oceanic realm. We prefer the use of long-wavelength free-air gravity anomalies to estimate continental dynamic topography. In the oceanic realm, these anomalies correlate surprisingly well with residual depth estimates (e.g. Figure 3 of main text). There is also a good match at passive margins where oceanic lithosphere abuts the continents.

Finally, we investigate the spectral consequences of changing the value of admittance, $Z = 50$ mGal km^{-1}, used to estimate continental dynamic topography from long-wavelength

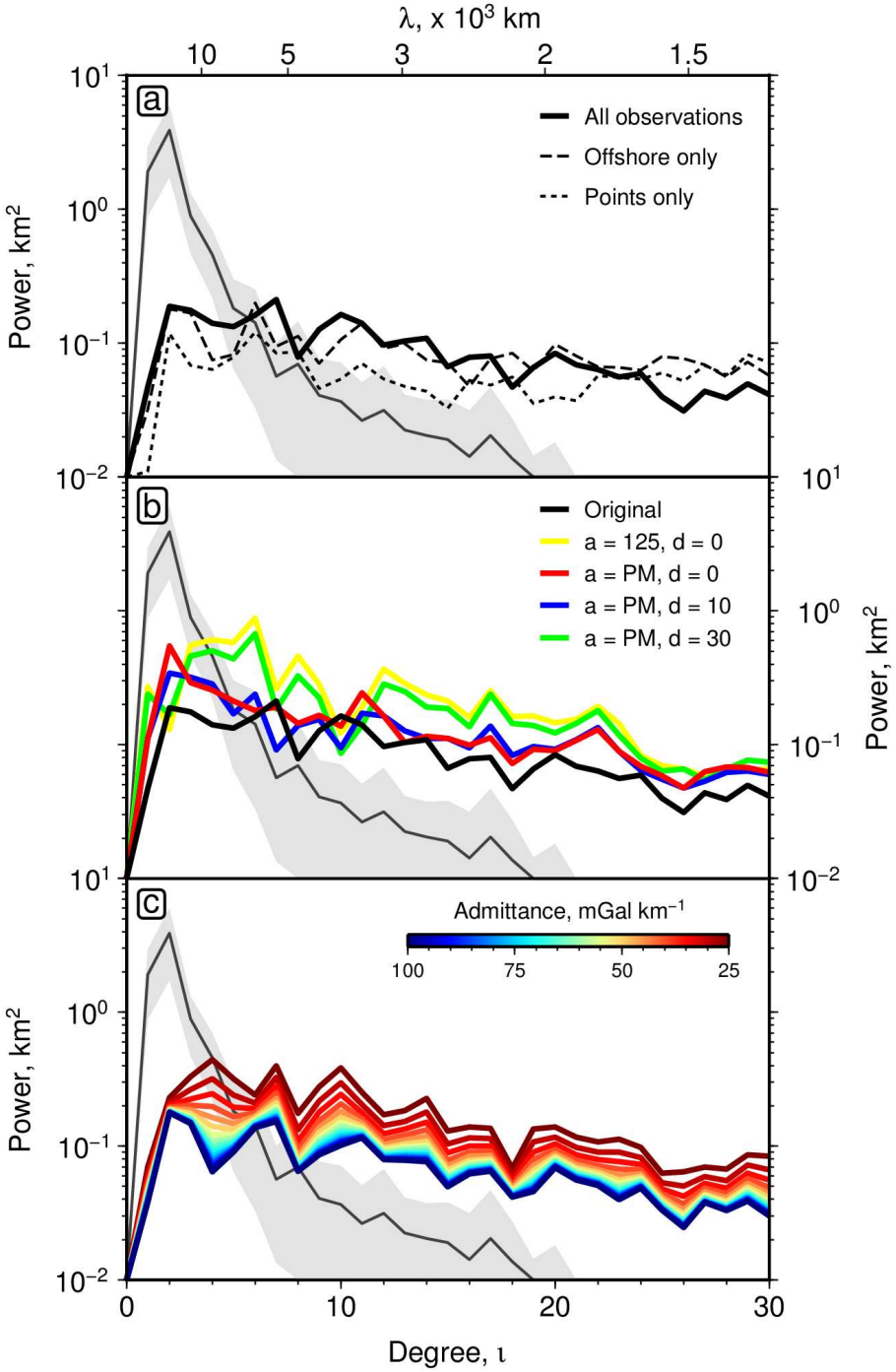

Figure 9: Continental Tests. (a) Power spectra for decimated datasets. Solid line = power spectrum for complete observational database (Figure 1b of main text); dashed line = power spectrum for oceanic spot measurements and ship-track data alone (i.e. no continental input); dotted line = power spectrum for oceanic spot measurements alone. Grey line/band = mean/standard deviation of 5 predictive models of dynamic topography[7,8,9,10,13]. (b) Power spectra for alternative continental observations. Black line = power spectrum using continental dynamic topography calculated from long-wavelength free-air gravity anomalies; yellow line = power spectrum using continental dynamic topography calculated from CRUST 1.0 database assuming constant lithospheric thickness of 125 km[54]; red line = as before but using variable lithospheric thickness[36]; blue line = as before where lithosphere thicker than 175 km is depleted by 10 kg m^{-3}; green line = as before with depletion of 30 kg m^{-3}. (c) Coloured lines = power spectra using continental dynamic topography calculated from long-wavelength free-air gravity anomalies using admittance values ranging from 25–100 mGal km^{-1}.

free-air gravity anomalies. In Figure 9c, a range of $Z = 25$–100 mGal km^{-1} has been used. The resultant power spectra have similar slopes. When Z increases, spectral power for continental dynamic topography decreases for all wavelengths. As $Z \to \infty$, continental dynamic topography tends toward zero and the resultant power spectrum is dominated by oceanic measurements. As $Z \to 0$, continental dynamic topography becomes unrealistically large. Thus admittance of less than $Z = 25$ mGal km^{-1} is unlikely since it gives rise to geologically implausible values. For example, $Z = 10$ mGal km^{-1} yields peak dynamic topographic amplitudes of ± 8 km.

Several studies have suggested that admittance can vary as a function of wavelength e.g.[32,55,56,57]. For example, Revenaugh and Parsons[56] argue that Z varies from 25 to 75 mGal km^{-1} for wavelengths of 2×10^4 and 2×10^3 km, if mantle viscosity decreases exponentially with depth. We have tested the spectral implications of this proposed variation by assuming that

$$Z(l) = 50 \tanh\left(\frac{l}{a}\right) \tag{22}$$

where $Z(l)$ is admittance as a function of degree and a is a constant term that controls how quickly admittance reaches 50 mGal km^{-1}. The consequences of using three different admittance curves where $a = 2$, 5 and 10 are investigated (Figure 10a). Significantly, the resultant harmonic representations of dynamic topography do not accurately match our oceanic residual depth observations. As before, these global grids have been used to constrain continental dynamic topography by re-sampling the grids at identical onshore nodes. Power spectra were then calculated. Even for the extreme case of $a = 10$ that implies $Z \approx 10$ mGal km^{-1} at $l = 2$, there is a one order of magnitude difference between observed and predicted power for $l = 2$ (Figure 10c). We confidently conclude that our choice of continental admittance is not the source of spectral discrepancies between observed and predicted dynamic topography.

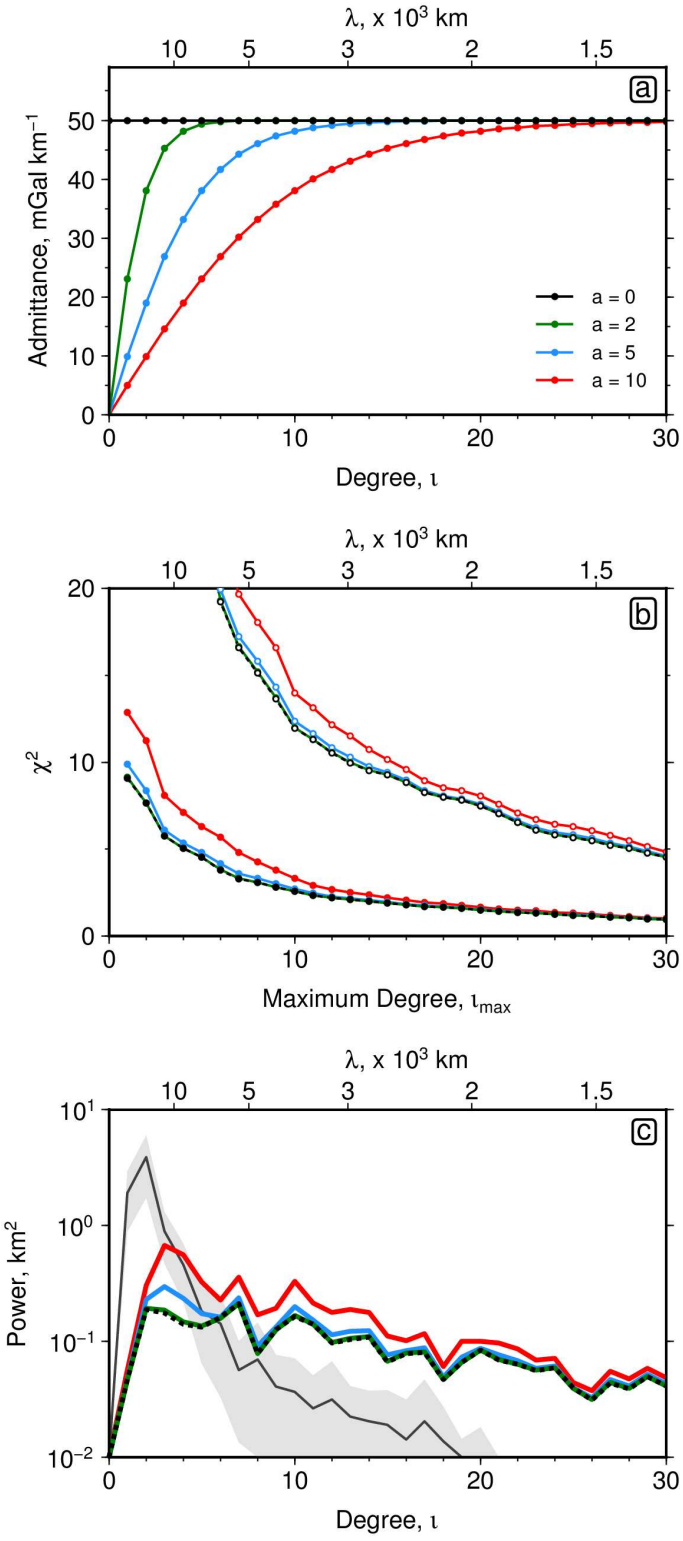

Figure 10: Wavelength-dependent admittance tests. (a) Admittance curves used to calculate four different sets of gravity-derived continental dynamic topographic databases. (b) Residual misfit, χ^2, for these four sets. Solid circles = oceanic and continental databases; open circles = spot measurements from oceanic realm alone. (c) Power spectra. Thick lines = power spectra calculated from four different sets of databases; thin line with grey bounds = mean and standard deviation of power spectra for five predictive models.

Checkerboard, Damping and Benchmarking Tests

We have carried out a series of tests which enable us to assess how different data coverage affects the recoverability of our spherical harmonic analysis. First, a series of checkerboard tests were performed. Three different input models were constructed: (i) $l = 10$ and $m = 5$; (ii) $l = 20$ and $m = 10$; and (iii) $l = 30$ and $m = 15$ (Figures 11a, 12a and 13a). Each input model was sub-sampled in accordance with the distribution of measurements from oceanic and continental realms (Figures 11b, 12b and 13b). Regularised least squares inversion of each sub-sampled distribution demonstrates the fidelity of signal recovery (Figures 13c, 13c and 13c). If the continental realm is completely removed, signal recovery of the oceanic realm is good (Figures 11e, 12e and 13e). Finally, if only spot measurements from the oceanic realm are included, signal recovery is still satisfactory (Figures 11g, 12g and 13g).

Secondly, we explored the effects of gradient smoothing, λ_1, and amplitude damping, λ_2, upon the recoverability of power spectra. λ_1 and λ_2 were systematically varied between $10^{-0.5}$–$10^{+0.5}$ and 10^2–10^3, respectively. When both are zero, the recovered power spectrum becomes convex upward between $l = 10$ and $l = 20$. When any regularisation is introduced, resultant spectra stabilise and exhibit little significant variation apart from a gradual decrease in overall amplitudes. This range of regularisation parameters gives rise to the calculated error bounds shown in Figure 5b of the main text.

Thirdly, we benchmarked our ability to recover red spectra by analysing the predictive model of Flament et al.[10]. We sub-sampled this model in accordance with the distribution of our oceanic and continental observations. Random noise was added, scaled by the uncertainty associated with each observation. We then carried out a regularised least squares inversion of a series of increasingly decimated data distributions. Recovered power spectra closely resemble the original spectrum of the predictive model (Figure 14).

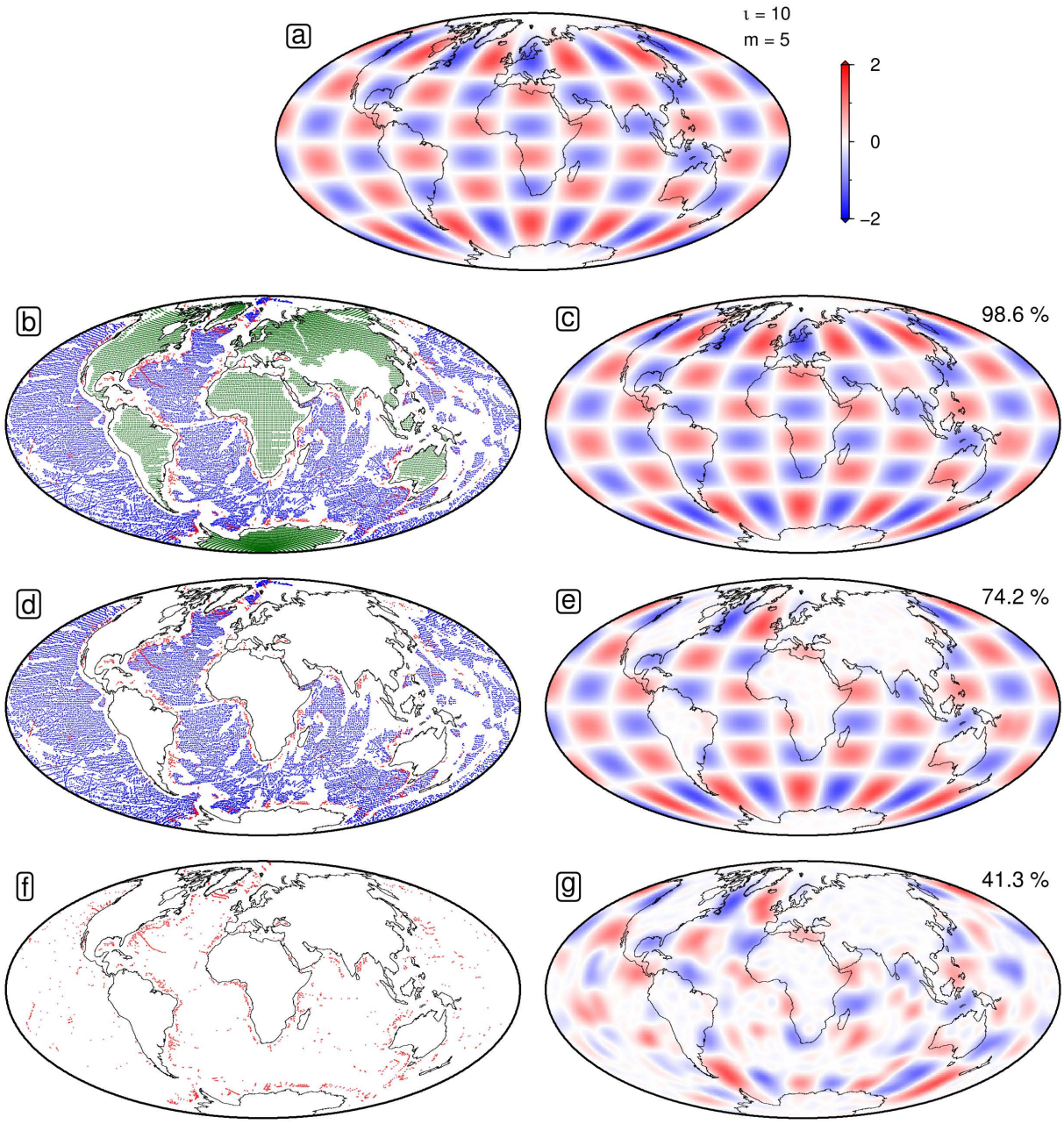

Figure 11: Synthetic checkerboard test. (a) Input spherical harmonic function with $l = 10$ and $m = 5$. (b) Locations of all oceanic and continental data points used to sub-sample input model. (c) Resulting spherical harmonic fit with recovery of input coefficients. (d) All measurements from oceanic realm alone. (e) Recovery obtained using (d). (f) Only spot measurements from oceanic realm (symbols from Figure 1b of main text). (g) Recovery obtained using (f).

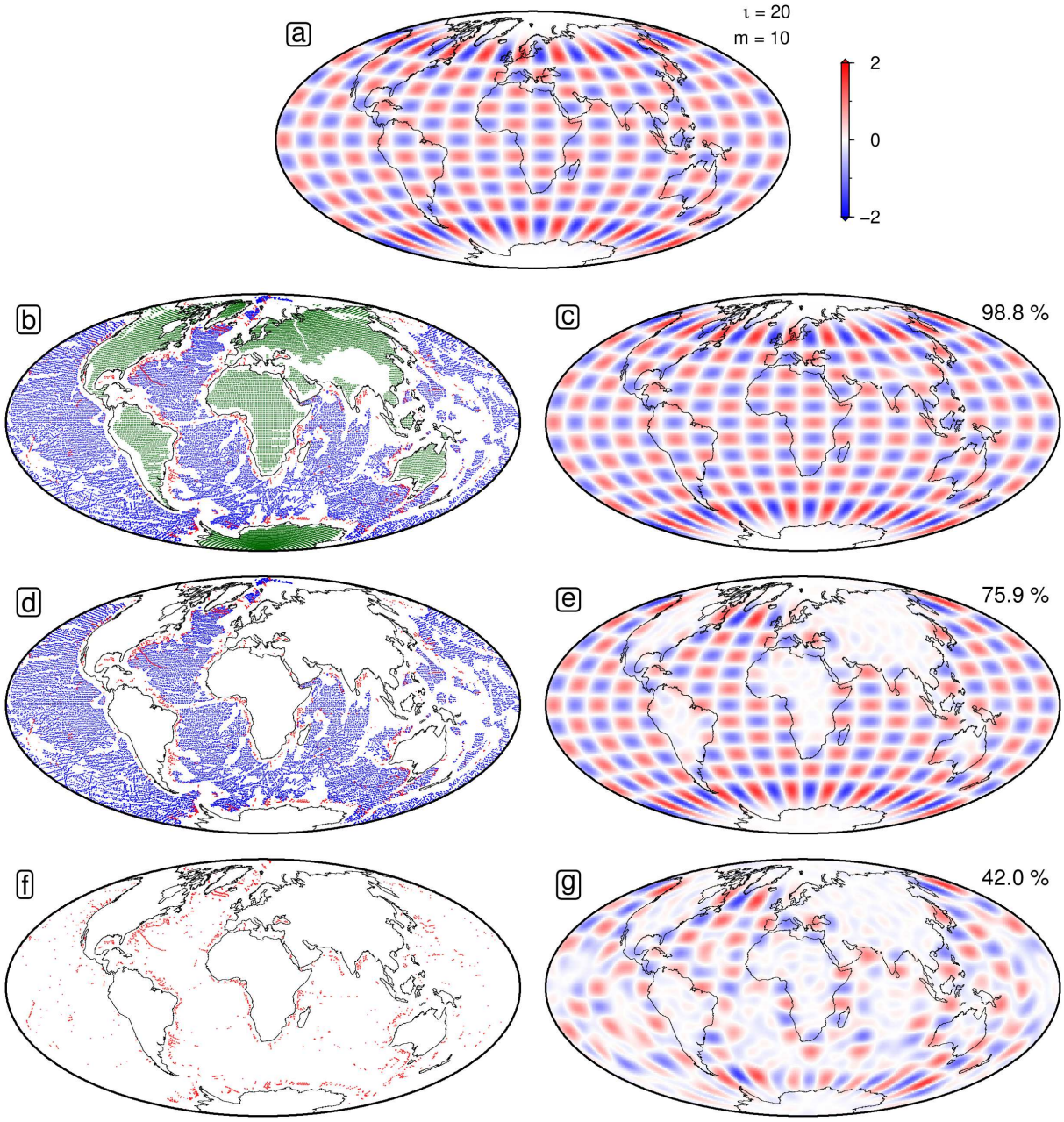

Figure 12: Synthetic checkerboard test. (a) Input spherical harmonic function with $l = 20$ and $m = 10$. (b) Locations of all oceanic and continental data points used to sub-sample input model. (c) Resulting spherical harmonic fit with recovery of input coefficients. (d) All measurements from oceanic realm alone. (e) Recovery obtained using (d). (f) Only spot measurements from oceanic realm (symbols from Figure 1b of main text). (g) Recovery obtained using (f).

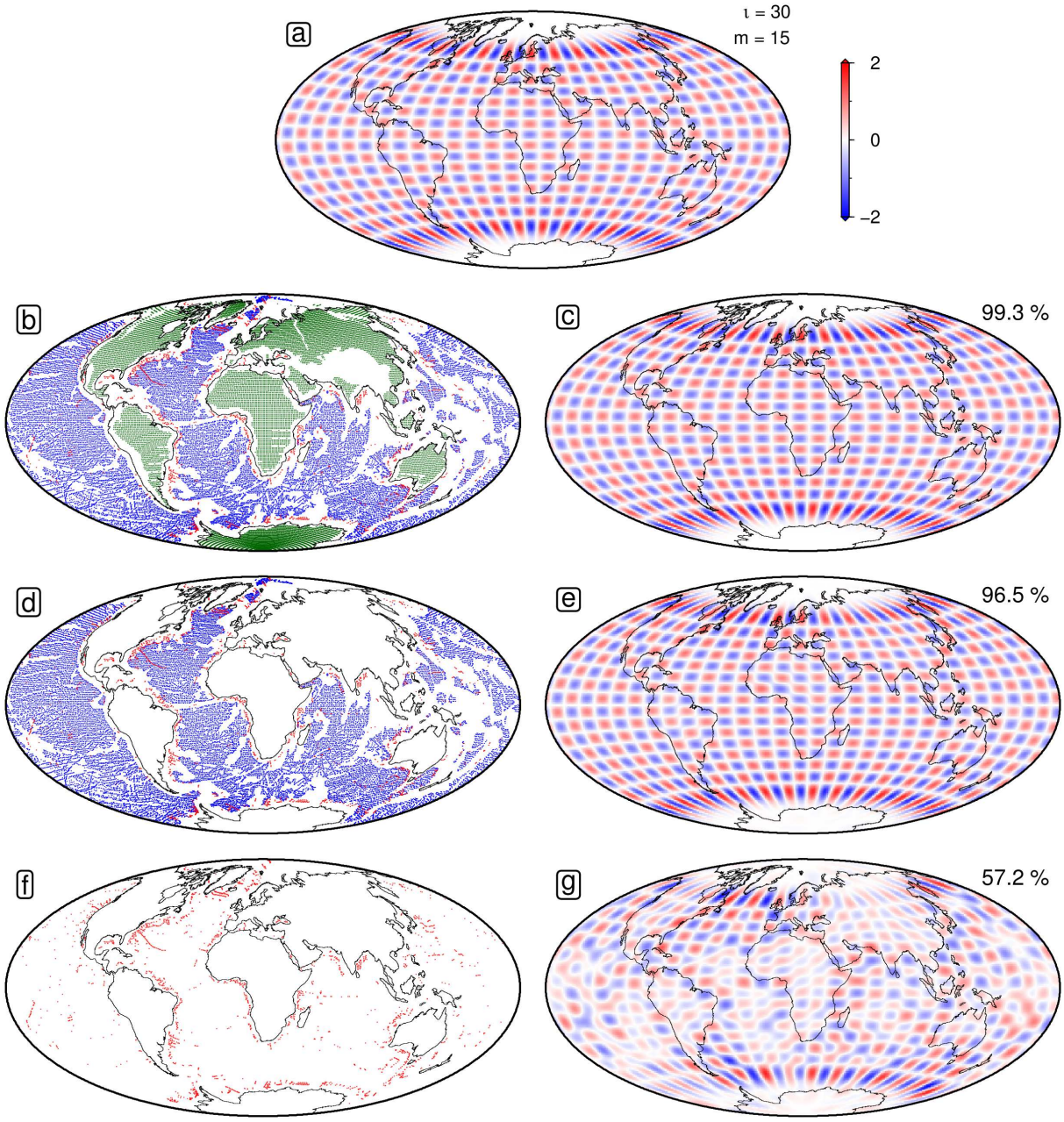

Figure 13: Synthetic checkerboard test. (a) Input spherical harmonic function with $l = 30$ and $m = 15$. (b) Locations of all oceanic and continental data points used to sub-sample input model. (c) Resulting spherical harmonic fit with recovery of input coefficients. (d) All measurements from oceanic realm alone. (e) Recovery obtained using (d). (f) Only spot measurements from oceanic realm (symbols from Figure 1b of main text). (g) Recovery obtained using (f).

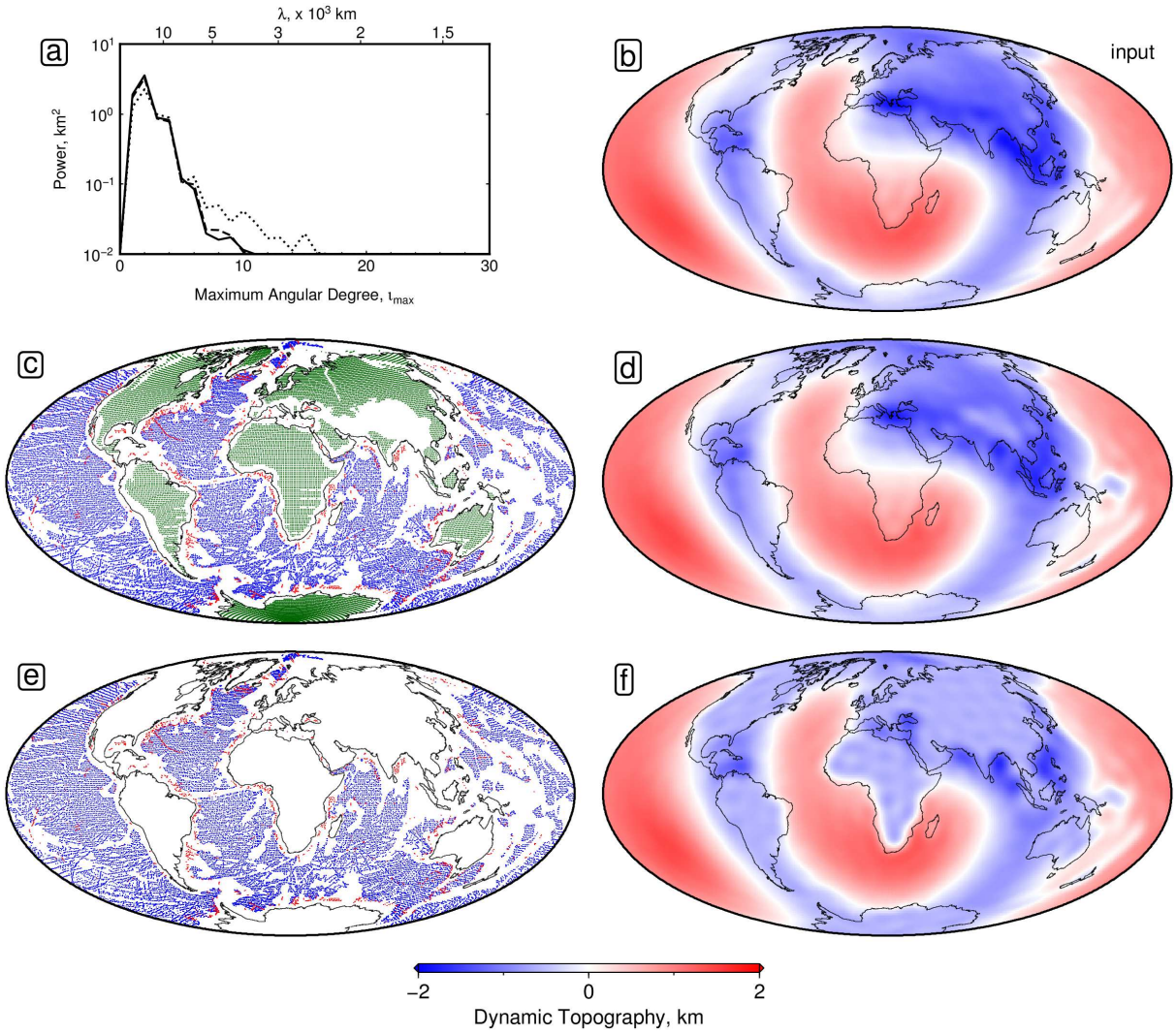

Figure 14: Benchmark test. (a) Solid line = power of predicted dynamic topographic model shown in (b); dashed line = recovered power using data distribution shown in (c); dotted line = recovered power using data distribution shown in (e). (b) Global dynamic topography prediction from Flament et al.[10]. (c) Oceanic and continental data points used to sub-sample input model. (d) Recovered model obtained using (c). (e) Oceanic data points. (f) Recovered model obtained using (e).

Latitudinal Test

Residual depth observations are averaged into 1° bins which results in an increased density of data toward higher latitudes. To check whether this density increase affects our results, we have carried out an inversion for which each datapoint is weighted by the surface area of the 1° bin within which it lies. The modified misfit function is

$$\chi^2 = \frac{1}{N} \sum_{i=1}^{N} \frac{1}{\sigma_i^2} \left(\frac{A_i}{A_{45}} \right) [f(\theta_i, \varphi_i) - d_i]^2 \tag{23}$$

where A_i is the area of a 1° bin and A_{45} is the area of a 1° bin at a latitude of 45°. In this way, points closer to either pole are correctly weighted with respect to points which are closer to the equator. The resultant power spectrum is very similar to that calculated without latitudinal weighting, which means that this effect does not alter our conclusions (Figure 15).

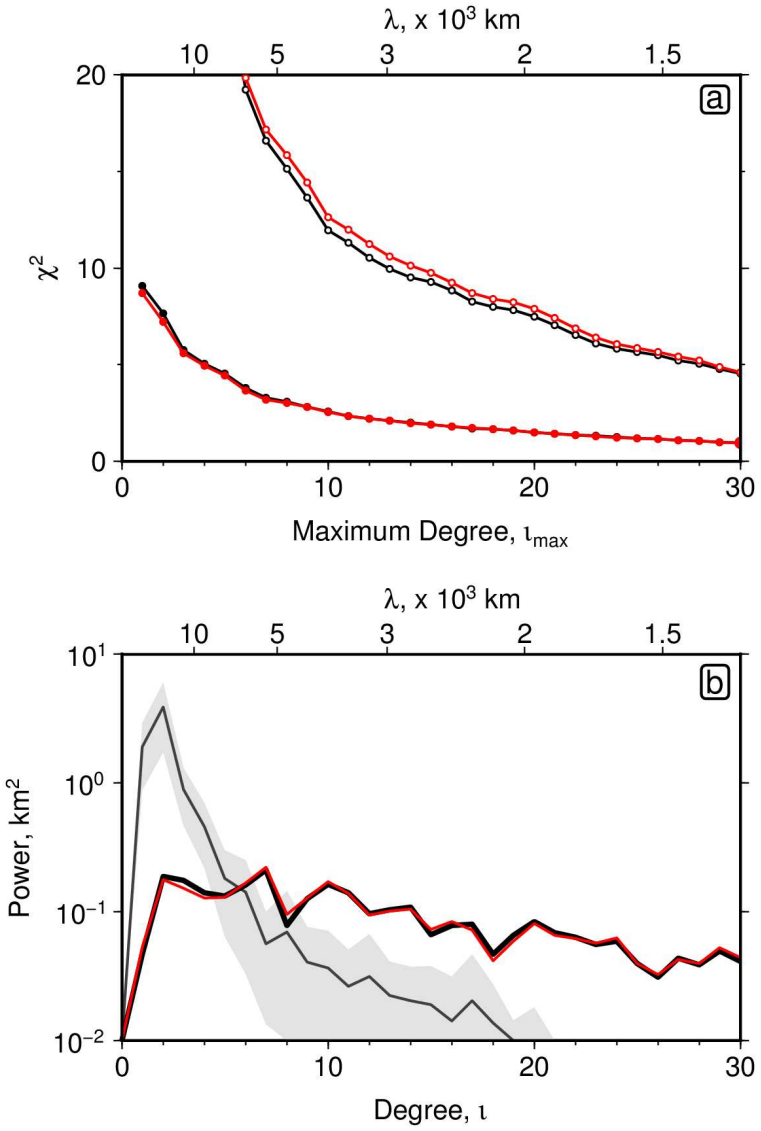

Figure 15: Effect of weighting the data by latitude. (a) Residual misfit, χ^2, plotted as function of maximum degree; solid circles = χ^2 values from fitting combined offshore/onshore global database of dynamic topographic observations; open circles = χ^2 values from fitting spot measurements from oceanic realm alone; black = original, non-latitude weighted data; red = including a latitude weighting. (b) Power spectra of observed dynamic topography using non-latitude (black) and latitude-weighted (red) misfit functions. Grey line/bounds = mean/standard deviation of the five predictive models.

Kaula's Rule

The Earth's gravity field can be described using spherical harmonic coefficients. Power, $P_l^{\Delta g}$, as a function of degree, l, is given by

$$P_l^{\Delta g} = \left(\frac{GM}{R^2}\right)^2 (l-1)^2 \sum_{m=-l}^{l} f_{lm}^2 \tag{24}$$

where $G = 6.67 \times 10^{-11}$ m^3 kg^{-1} s^{-2} is the gravitational constant, $M = 5.97 \times 10^{24}$ kg is the mass of the Earth, $R = 6371$ km is the radius of the Earth, and f_{lm} are the fully normalised spherical harmonic coefficients[58].

Kaula[59] proposed a rule of thumb to estimate the order of magnitude of each coefficient as a function of degree, where $f_{lm} = 10^{-5}/l^2$. Satellite observation was in its infancy and only the first few coefficients for the lowest degrees were known. Nevertheless, this rule has proven to be surprisingly accurate for spherical expansions of up to $l = 360$ and higher. Combining Kaula's rule with Equation (24) and noting that for each degree there are $(2l + 1)$ separate coefficients, the calculated power of dynamic topography is given by

$$P_l^{DT} = \left(\frac{GM}{ZR^2}\right)^2 \left(\frac{2}{l} - \frac{3}{l^2} + \frac{1}{l^4}\right) \tag{25}$$

where $G = 6.67 \times 10^{-11}$ m^3 kg^{-1} s^{-2} is the gravitational constant, $M = 5.97 \times 10^{24}$ kg is mass of the Earth, $R = 6371$ km is radius of the Earth, and Z is the admittance. If $Z = 12 \pm 3$ mGal km^{-1}, we can match the spectral power distribution of observed dynamic topography (Figure 16). Note that Z is independent of degree.

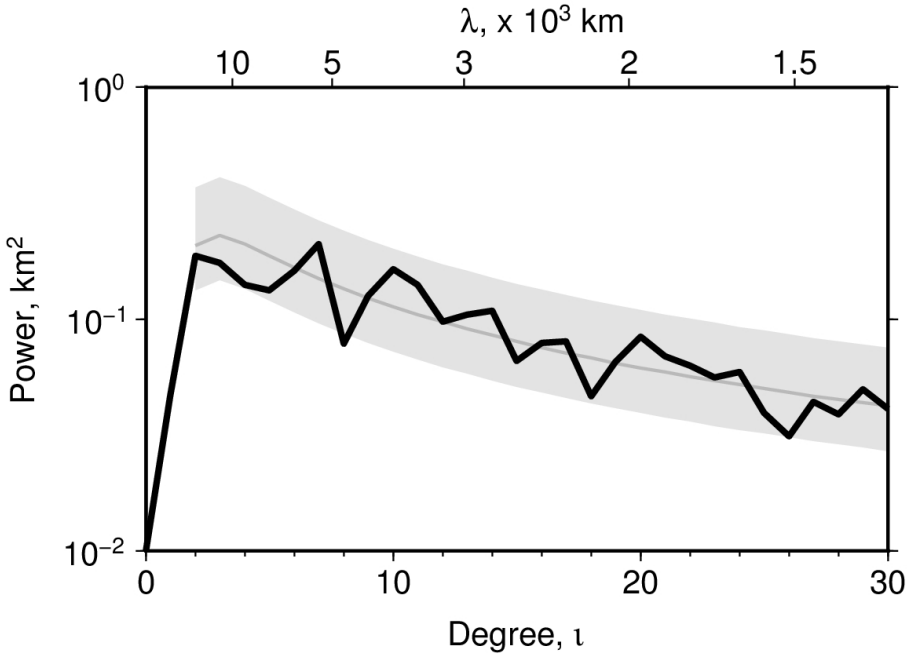

Figure 16: Kaula's rule. Solid line = power spectrum of observational database (Figure 5b in main text); grey line/band = power spectrum calculated using Equation 25 for $Z = 12 \pm 3$ mGal km^{-1}.

Isostatic Vertical Displacement Caused by an Asthenospheric Channel

The air-loaded vertical displacement generated by a sub-plate asthenospheric channel is calculated by balancing the lithostatic pressure at the base of two columns (Figure 17). This calculation assumes that the flow field has zero vertical component. The pressure beneath the original column, P_a, is given by

$$P_a = \rho_l g z_l + \rho_\circ \left(1 - \alpha T_\circ\right) g \left(h - U\right) \tag{26}$$

where g is gravitational acceleration, ρ_l and z_l are density and thickness of lithosphere respectively, and $\rho_\circ$ is asthenospheric density at $0°$C (Figure 17a). U is the air-loaded isostatic uplift, h is the channel thickness, α is the thermal expansion coefficient and $T_\circ$ is the average temperature of the channel (Figure 17b). The pressure beneath the perturbed column, P_b, is given by

$$P_b = \rho_l g z_l + \rho_\circ \left[1 - \alpha \left(T_\circ + \Delta T\right)\right] g h \tag{27}$$

where ΔT is the average excess temperature within the channel. If these two columns are in isostatic equilibrium, then $P_a = P_b$. Expanding Equations 26 and 27, cancelling out common factors, and re-arranging yields

$$\Delta T = \frac{U \left(1 - \alpha T_\circ\right)}{h \alpha}. \tag{28}$$

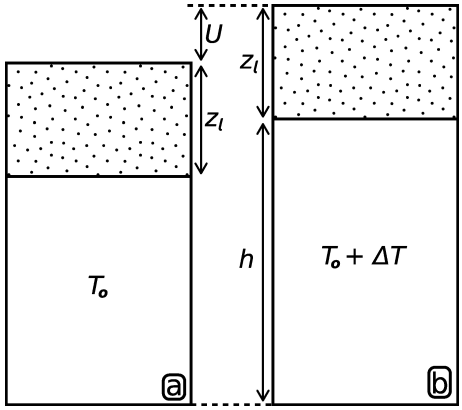

Figure 17: Sub-plate asthenospheric isostatic balance. (a) Standard case, where $T_\circ$ = average temperature of the asthenosphere. Dotted pattern = crust and lithospheric mantle. (b) Air-loaded uplift, U, generated from a sub-plate channel of thickness h, and average temperature $T_\circ + \Delta T$.

Residual Depth Database

Table 1: 1,006 accurate residual depth measurements (circles in Figure 1b of main text), averaged over 1° bins.

Lon.[a]	Lat.[a]	z_r, m	Error, m	Lon.[a]	Lat.[a]	z_r, m	Error, m	Lon.[a]	Lat.[a]	z_r, m	Error, m	Lon.[a]	Lat.[a]	z_r, m	Error, m
7.49	70.00	551	104	8.01	69.80	689	101	8.52	69.51	681	80	10.31	69.93	426	102
10.97	69.68	495	103	-15.83	69.87	1776	21	-15.04	69.81	1762	27	-14.03	69.70	1887	21
-13.00	69.56	1842	32	-12.48	69.50	1899	21	-10.33	69.52	2013	53	7.09	69.31	974	72
9.02	69.27	450	104	9.60	69.00	406	111	11.47	69.49	539	102	11.82	69.36	559	104
-64.54	69.47	1011	137	-63.98	69.33	792	162	-63.00	69.07	355	173	-62.00	68.82	387	184
-61.12	68.59	619	170	-15.66	69.46	1723	31	-11.97	69.44	1774	43	-10.99	69.28	1769	61
-10.43	69.38	1922	61	0.98	67.71	1315	91	-60.62	68.47	790	175	-60.00	68.31	1172	198
-59.39	68.15	1416	189	-18.12	67.82	1828	35	-18.52	66.81	1766	78	-18.38	67.18	1958	61
1.07	65.91	1353	81	1.61	65.57	1292	91	-33.59	65.51	532	364	-3.70	66.21	634	100
-3.00	65.97	1038	100	-2.05	65.65	1082	104	0.00	64.96	1225	90	0.79	64.70	995	104
2.10	65.26	1404	75	-33.53	65.48	511	363	-33.00	65.26	526	290	-32.00	64.84	935	137
-31.34	64.57	1371	64	-1.54	65.48	1250	101	-1.00	65.30	1069	110	0.00	64.96	1225	90
-31.01	64.43	1146	66	-23.61	63.55	2072	106	-38.66	63.02	778	222	-37.93	62.78	779	192
-37.26	62.58	1018	160	-24.64	63.04	2107	78	-24.00	63.22	2138	84	-36.78	62.41	903	143
-36.16	62.22	958	114	-26.75	61.74	1654	47	-25.84	62.06	2481	45	-25.07	62.09	2257	57
-24.27	61.61	2013	46	-57.22	60.79	762	97	-26.23	61.45	1807	23	-23.96	61.47	1780	52
177.18	59.86	-509	145	-59.72	59.90	247	183	-59.08	59.60	415	156	-57.87	60.23	480	131
-56.88	59.52	301	130	-51.79	59.88	805	81	-51.20	60.05	916	83	-20.91	59.78	1150	87
-20.41	59.55	972	118	177.19	59.00	-362	156	-59.08	59.40	307	185	-57.59	59.15	670	110
-57.22	59.34	524	126	-42.66	59.10	418	202	-42.00	58.93	466	141	-41.00	58.66	631	106
-40.44	58.52	644	97	-20.20	59.45	759	137	177.20	58.00	-605	132	-178.25	57.92	-502	161
-176.97	57.62	-488	167	-55.97	57.77	328	143	-55.41	57.63	388	124	-40.27	58.47	497	98
-32.74	57.75	1257	7	-32.23	57.61	1631	14	177.21	57.42	-610	124	-55.79	57.30	470	135
-54.99	57.07	845	115	-54.19	56.97	1020	114	-24.82	57.23	1275	64	-24.07	56.94	1128	81
-23.30	56.92	1212	59	-53.74	56.30	394	115	-53.26	55.87	363	121	-23.84	56.49	1002	117
-163.59	52.54	-425	28	-163.53	52.45	-220	32	-163.47	52.38	-102	27	-171.84	50.53	-46	16
-171.66	50.25	223	14	-44.69	50.34	922	111	-44.48	50.38	1093	92	-41.38	48.54	487	95
-14.72	48.60	364	56	-14.04	48.79	247	84	-130.74	48.36	389	62	-129.85	48.17	272	63
-129.00	47.98	350	65	-128.12	47.78	264	63	-127.42	47.63	114	74	-42.02	48.39	294	120
-130.85	47.31	577	60	-129.91	47.06	485	59	-128.82	46.70	182	61	-128.29	46.59	85	66
-7.40	46.51	-1158	146	-127.95	46.39	114	67	-45.12	45.55	564	115	-43.52	46.32	724	140
-43.16	46.10	493	131	-7.78	46.09	-1108	120	-7.46	46.45	-1134	125	-131.54	45.29	177	60
-131.23	45.22	366	58	-129.66	44.83	235	61	-129.16	44.71	119	63	-126.59	44.64	418	69
-126.16	44.64	112	81	-46.67	44.58	307	146	-44.77	45.37	294	141	-44.00	44.99	313	124
-43.48	44.73	501	99	-8.58	44.84	-1263	97	32.21	43.79	-2441	533	32.68	43.59	-2940	561
-53.28	43.53	-339	236	-47.09	43.58	-652	133	-45.92	44.17	238	102	-45.35	43.87	135	106
32.16	43.06	-2125	493	33.04	43.31	-2885	552	34.00	42.88	-2517	503	37.27	42.66	-265	246
37.98	42.90	-917	327	38.78	42.64	-1066	351	138.21	42.61	-740	92	-58.53	42.98	-1545	275
-58.20	43.03	-1519	274	-53.37	43.45	-531	232	-46.69	43.47	-591	116	-46.48	43.44	-504	101
5.18	41.56	-1078	227	37.99	42.35	-181	241	39.18	42.42	-1197	368	136.38	41.83	-787	81
137.00	42.10	-879	88	137.72	42.40	-831	90	-63.75	41.66	-408	220	-60.54	41.79	-1417	172
-60.34	41.85	-1355	190	-57.67	41.99	-851	188	-57.47	41.56	-770	160	-13.24	42.14	-714	71
5.36	41.41	-1239	217	5.93	40.93	-1554	237	147.57	40.52	-345	76	-59.91	41.12	-1222	145
-57.38	41.38	-807	166	-13.63	40.50	-924	63	6.34	39.86	-716	230	6.55	39.84	-586	216
147.94	40.00	-308	72	150.82	40.05	-164	67	-13.54	40.49	-1129	67	-13.12	40.45	-1242	102
5.55	38.53	-300	153	145.18	38.98	47	49	145.69	38.92	272	27	147.09	39.24	-140	68
148.13	39.09	-338	64	148.63	39.02	-379	63	-72.27	38.60	-1313	294	2.45	37.65	-385	144
5.61	38.00	-317	155	147.69	38.47	-314	64	-68.88	38.06	-480	156	-11.64	38.15	-1003	152
-11.16	38.12	-1102	148	2.49	37.47	-546	145	2.52	37.39	-569	147	5.67	37.44	-444	169
153.25	36.69	-548	68	153.91	36.74	-620	73	154.96	36.82	-546	71	155.57	36.86	-602	69
-123.50	37.22	-48	89	-123.38	37.28	-37	132	-74.04	36.51	-574	257	-70.26	37.12	-352	131
145.16	36.27	-336	63	146.01	36.10	-358	65	146.61	35.77	-457	64	152.64	36.40	-543	68
-73.75	36.45	-524	222	-73.42	36.39	-573	208	-12.90	35.85	-834	112	146.48	34.53	-484	64
146.55	35.39	-503	64	-72.69	34.75	-790	153	-71.93	34.63	-444	129	-69.84	34.54	-475	93
-36.51	34.59	455	32	-36.40	34.92	577	28	-10.78	34.74	-388	139	-10.42	34.86	85	144
146.49	34.33	-470	64	147.07	34.06	-429	63	147.66	34.03	-427	58	149.35	33.92	-288	61
150.12	33.86	-401	66	152.02	33.96	-459	63	152.84	33.88	-578	64	153.91	34.00	-357	62
154.56	34.02	-278	65	-73.15	34.00	-963	157	-72.19	33.74	-791	112	-70.54	34.14	-542	96
-37.72	33.88	25	34	-37.09	34.31	67	25	-12.96	33.67	-103	115	-10.53	34.48	-798	144
-10.36	34.31	-1066	166	34.14	32.85	-270	333	143.35	33.26	-213	69	-73.60	33.13	-1081	147
-73.45	33.42	-1091	154	-71.78	32.62	-812	102	-71.33	32.96	-900	106	33.48	32.24	76	357
33.86	32.11	216	334	34.56	32.43	-88	359	143.74	31.86	-341	61	-76.52	31.78	-875	297
-76.16	32.10	-794	219	-69.81	32.06	-414	84	-69.01	31.67	-248	81	133.86	31.00	-490	74
143.98	31.07	-365	61	144.77	31.00	-425	60	146.14	30.83	-576	62	147.20	30.69	-645	63
148.03	30.71	-635	63	148.75	30.73	-662	64	-75.52	30.64	-455	178	-68.59	31.47	-141	76
-68.00	31.18	-216	77	-67.03	30.69	-210	76	-75.51	30.24	-676	164	-66.53	30.43	-202	78
-66.29	30.30	-45	77	-65.41	29.83	65	74	-71.63	28.54	-528	99	-63.63	28.88	50	64
-63.19	28.61	36	60	147.12	27.59	-256	65	-111.85	27.57	-888	149	-71.50	28.50	-647	99
-71.07	28.17	-557	89	-69.64	27.83	-525	79	-69.28	27.70	-415	80	-62.70	28.33	23	61
-62.08	27.97	-229	59	-61.45	27.61	-569	58	-20.87	27.95	-291	91	146.34	27.19	-336	73
147.00	27.14	-249	71	147.85	27.07	-283	62	-111.62	27.42	-635	115	-111.00	27.02	-293	111
-110.36	26.60	-412	122	-89.76	26.91	-1246	388	-88.92	27.06	-1050	365	-88.03	26.94	-899	311
-87.05	26.69	-696	262	-60.74	27.19	-648	60	-59.90	26.68	-707	60	-109.97	26.35	-257	149
-93.93	26.01	-1713	383	-93.15	25.92	-1791	381	-92.00	25.76	-1680	374	-90.88	25.92	-1685	332
-89.95	25.98	-1388	312	-88.96	26.25	-1200	322	-87.92	26.21	-969	294	-86.96	26.03	-739	248
-86.20	25.85	-458	219	-75.26	25.71	136	92	-59.07	26.16	-704	68	-58.13	25.58	-617	58
146.14	25.18	-575	75	-86.67	25.40	-560	220	-86.10	25.31	-349	213	-85.42	25.11	-280	192
-75.05	25.38	98	98	-56.96	24.94	-393	62	-108.62	23.63	-570	124	-108.47	23.53	-647	113
-54.42	24.28	-605	67	-53.35	24.00	-625	79	-52.26	23.71	-559	75	-23.04	24.14	138	90
-21.66	23.82	-304	100	-21.00	23.69	-202	101	-20.30	23.56	-277	122	65.38	22.75	170	255
65.70	22.76	-4	284	121.92	22.83	-769	115	-157.55	23.39	1085	57	-108.86	22.62	-442	88
-108.04	23.23	-148	105	-50.84	23.35	-573	66	-46.85	22.78	-448	103	-46.47	22.78	-575	92
-19.71	23.45	-286	139	-18.94	23.21	-353	177	-17.86	22.99	-362	292	-17.50	23.37	-159	335
65.03	22.19	203	205	-108.59	22.45	-51	96	-108.08	22.18	-133	111	-107.37	21.76	-5	123
-67.84	22.27	-494	79	-67.25	22.25	-656	77	-66.49	22.14	-501	65	38.28	20.06	2088	92
38.69	19.59	1497	67	60.37	20.13	614	131	60.57	20.00	932	90	64.06	19.91	350	133
64.94	19.88	71	148	66.09	19.77	879	132	89.02	19.50	-1208	437	155.24	20.00	-237	69
-159.31	19.58	907	60	38.45	19.31	1547	153	38.56	19.43	1668	127	64.92	19.48	330	127
65.89	19.41	952	122	67.99	19.11	985	100	68.77	18.70	1100	102	86.81	18.65	-244	261
88.13	18.82	-1168	372	88.75	19.29	-1227	418	119.22	18.99	-1266	146	64.92	17.88	-142	142
68.20	18.04	742	103	68.76	18.11	635	114	87.02	17.93	-798	296	88.01	17.92	-1045	341

Continued overleaf...

Table 1 – continued

Lon.[a]	Lat.[a]	z_r, m	Error, m	Lon.[a]	Lat.[a]	z_r, m	Error, m	Lon.[a]	Lat.[a]	z_r, m	Error, m	Lon.[a]	Lat.[a]	z_r, m	Error, m
88.61	18.06	-1034	352	114.86	18.04	-233	106	116.30	17.99	-552	111	64.81	17.24	-427	143
66.64	17.14	283	109	68.81	17.41	871	96	84.02	16.61	-820	257	86.50	16.80	-422	235
87.09	16.99	-753	285	87.83	17.23	-963	311	88.95	17.23	-842	294	115.57	16.58	-246	112
-23.61	16.80	1184	77	41.67	15.98	751	108	53.98	16.28	819	84	83.09	15.58	-801	251
84.10	16.10	-1071	273	84.69	16.33	-983	269	86.38	15.73	-583	231	86.76	16.24	-684	251
115.70	16.30	-678	106	-105.66	16.07	367	55	-105.26	16.11	197	55	-23.80	15.96	792	82
67.88	15.24	315	89	81.45	14.62	-807	244	81.53	14.57	-714	229	83.12	15.02	-658	224
83.95	14.68	-522	206	150.02	14.83	-236	63	150.96	15.13	-280	60	-66.56	14.87	40	97
-66.46	14.66	-34	104	-23.99	15.11	1311	80	81.29	13.97	-444	205	82.05	13.88	-449	195
82.91	13.77	-444	199	83.83	14.14	-461	194	-67.69	14.02	-273	96	-66.67	14.02	-257	121
-66.34	14.41	-81	109	-24.24	13.98	538	70	81.31	13.07	-140	187	81.84	12.97	-425	202
83.03	12.87	-376	207	83.53	12.91	-439	185	69.38	12.01	586	66	69.85	12.18	682	62
81.23	12.08	-172	167	82.07	12.13	-451	208	82.82	12.04	-402	196	81.35	11.14	-469	174
81.68	11.23	-587	181	-86.45	10.53	-122	64	-104.25	9.73	55	8	-86.67	10.30	222	66
-86.49	10.49	-41	65	-55.65	9.81	-1871	274	-55.37	9.72	-1246	210	-53.38	9.65	-785	123
-52.20	9.63	-533	160	71.82	8.56	584	119	-104.81	9.09	37	28	-104.16	9.03	-39	12
-55.65	8.82	-1208	254	-52.58	8.79	-382	108	-52.38	9.23	-553	157	71.36	8.36	590	82
71.59	8.46	572	99	-103.99	8.47	129	27	-55.53	8.49	-1044	258	-84.53	6.93	807	10
-84.38	6.77	724	24	-50.77	6.81	-752	229	-49.61	6.57	-1002	223	-13.87	6.91	31	115
-12.88	6.56	-71	151	-51.08	6.42	-375	224	-49.52	6.47	-1049	218	-49.13	6.06	-904	215
-46.23	5.68	-96	105	-12.94	6.48	-79	142	-12.14	5.68	-197	154	0.12	4.81	-928	211
1.36	4.52	-1028	192	1.71	4.53	-882	178	2.94	4.65	-827	210	3.82	4.87	-951	320
-48.93	4.95	-460	249	-47.98	4.73	-805	287	-47.08	4.88	-515	226	-46.20	5.15	-213	130
-45.42	4.51	81	153	-11.76	5.11	-160	147	-11.26	4.77	-164	156	0.12	4.81	-928	211
-0.13	4.28	-482	162	1.01	4.38	-841	174	2.13	4.13	-828	189	2.73	3.91	-631	173
3.95	4.03	-798	261	92.88	3.60	-570	112	-47.83	4.38	-626	336	-46.88	4.29	-643	271
-46.07	4.36	-407	198	-45.13	3.68	-232	141	-11.10	4.29	-155	136	-8.52	3.56	288	100
-7.96	3.65	159	116	-0.93	4.16	-592	129	-0.13	4.28	-482	162	2.47	3.31	-494	127
2.80	3.27	-466	127	3.95	3.29	-787	208	4.76	3.02	-430	203	5.66	2.69	-99	194
7.21	2.62	340	178	8.26	2.88	261	259	8.68	2.65	167	268	93.23	3.22	-793	120
93.70	2.72	-1039	137	-94.53	2.71	447	63	-94.34	2.69	474	58	-46.80	2.62	-983	309
-45.97	3.12	-479	182	-45.44	3.46	-318	155	-43.26	2.63	64	101	-8.54	3.48	301	96
-3.80	3.09	-585	110	5.42	2.41	-113	160	5.80	2.03	201	137	6.70	2.09	531	142
8.26	1.78	588	190	8.80	2.12	505	217	94.03	2.38	-1132	138	-91.66	2.29	533	67
-91.44	2.25	542	70	-46.73	2.39	-1071	303	-46.06	1.71	-912	286	-44.54	1.53	-208	130
-43.89	2.09	-32	108	-43.45	2.46	96	98	5.55	1.50	328	120	-83.71	1.11	82	60
-45.77	1.41	-706	249	-44.68	1.30	-213	129	-44.00	1.23	-7	112	-43.38	1.26	119	108
-43.83	-0.26	-5	171	-42.60	-0.35	-232	161	-42.28	0.03	-331	141	-41.32	-0.20	-274	138
-40.42	-0.34	123	113	-38.26	-0.41	375	82	-41.92	-1.17	-479	213	-40.90	-1.07	-39	153
-38.56	-0.83	21	99	-38.41	-0.62	251	88	43.15	-2.26	-409	206	44.77	-2.42	-277	140
56.92	-2.14	807	63	-41.20	-1.53	-84	184	7.90	-3.49	-277	118	42.85	-3.15	-242	188
43.86	-3.28	-256	158	44.92	-2.54	-311	135	56.33	-3.09	802	75	56.73	-2.98	791	76
-35.91	-2.90	13	145	-35.18	-3.34	215	115	-34.41	-3.29	-140	126	8.30	-4.09	-364	137
42.58	-3.58	-205	190	44.03	-3.60	-317	146	56.48	-3.58	895	83	56.52	-3.52	850	82
9.07	-4.74	-509	173	9.64	-5.13	-218	211	42.25	-5.34	366	135	43.12	-4.83	-332	152
43.64	-4.83	-198	131	-34.59	-4.51	244	107	9.13	-6.27	-800	191	42.20	-6.00	315	141
-138.14	-6.40	696	55	-34.20	-5.58	79	107	9.25	-6.98	-962	180	10.04	-7.11	-711	184
42.15	-6.66	90	170	43.31	-7.38	-83	117	-137.56	-7.21	723	56	-137.45	-7.37	691	57
-32.73	-6.83	-222	90	-32.20	-7.13	-377	92	9.20	-7.65	-590	120	10.29	-8.05	-442	140
10.51	-8.30	-304	134	42.97	-8.25	-255	140	-138.25	-8.34	928	11	-137.12	-7.83	699	56
-32.85	-7.72	-480	98	-32.16	-8.19	-752	97	10.45	-8.98	-73	112	10.51	-8.79	-165	123
42.06	-9.25	650	143	-138.67	-8.70	709	21	-138.47	-8.53	822	3	-33.62	-9.35	-150	94
-32.68	-9.09	-410	92	-32.19	-8.86	-605	93	10.50	-9.50	155	95	10.55	-9.72	511	94
42.07	-9.73	750	147	153.05	-10.05	-395	75	153.85	-10.13	-228	56	-140.65	-10.38	930	10
-140.25	-10.03	641	26	-34.11	-10.42	-192	95	-33.34	-9.56	-237	89	11.34	-11.31	825	91
11.57	-11.47	800	98	42.67	-11.08	720	136	-140.82	-10.52	1054	24	-35.67	-11.26	-259	165
-35.02	-11.00	-84	121	-34.36	-10.84	-75	93	11.37	-11.52	809	90	11.69	-11.52	663	110
42.36	-11.86	618	153	42.55	-11.68	834	149	50.03	-12.19	1249	88	-142.96	-12.30	450	56
-142.12	-11.61	580	62	-36.69	-12.19	225	138	-36.05	-12.01	-102	127	-35.49	-12.21	-77	101
11.34	-12.62	725	115	11.63	-12.77	771	135	41.89	-12.90	565	161	42.63	-12.74	3	156
44.25	-13.22	-20	152	44.56	-13.39	-108	157	46.12	-12.72	388	135	46.67	-13.20	239	149
119.14	-13.24	-26	86	-37.55	-13.41	123	129	-37.14	-13.04	8	130	-36.15	-12.63	-121	108
11.14	-13.94	456	121	43.14	-13.54	122	148	44.18	-13.65	-100	156	45.07	-13.88	-99	160
45.73	-13.84	-198	176	111.98	-13.91	-526	95	-145.81	-13.96	411	63	-145.42	-13.77	483	62
-37.90	-14.20	121	135	-37.19	-13.66	-37	120	10.83	-14.96	183	158	44.28	-14.53	-74	164
111.36	-15.36	-349	95	111.74	-15.34	-351	98	114.82	-15.46	-487	77	118.48	-14.75	-734	97
118.56	-14.79	-629	99	-149.25	-15.45	974	58	-77.07	-15.38	211	143	-37.73	-15.31	-140	140
-37.26	-15.25	-146	130	10.44	-16.27	-151	148	10.74	-15.85	15	156	110.37	-16.19	-500	76
110.56	-16.32	-360	68	112.05	-16.26	-159	147	114.89	-15.63	-389	73	117.46	-15.94	-545	75
117.65	-16.01	-542	76	-149.55	-16.07	1089	60	-114.53	-16.02	151	24	-114.00	-15.95	128	23
-112.97	-15.80	234	19	-112.00	-15.66	252	19	-111.48	-15.59	97	21	-76.79	-15.71	254	165
-76.36	-16.05	344	118	10.22	-16.84	-159	161	10.57	-16.85	-120	186	40.12	-17.18	355	251
41.00	-16.98	370	214	109.22	-17.42	-443	77	109.89	-17.33	-495	84	111.07	-17.00	-223	103
111.82	-16.93	-74	123	-114.72	-17.47	229	30	-114.06	-17.39	245	30	-112.78	-17.23	73	26
-112.33	-17.18	94	27	38.47	-18.09	-212	288	38.59	-18.34	-310	288	39.79	-18.08	-193	259
40.65	-18.19	470	215	109.34	-17.81	-375	73	109.98	-17.95	-220	94	110.93	-17.82	31	126
112.02	-17.64	-125	121	-115.50	-17.57	215	30	-115.22	-17.53	313	28	38.91	-18.99	-306	261
40.07	-19.00	-250	247	108.47	-18.97	-389	73	108.97	-18.89	-344	88	109.61	-18.78	-305	120
-37.31	-18.89	389	117	40.41	-19.70	145	217	40.66	-20.20	371	205	108.38	-19.62	-337	90
108.90	-20.00	-62	95	109.75	-20.21	-175	79	106.48	-20.99	-205	66	106.72	-21.24	-195	74
108.36	-20.86	-51	83	108.63	-20.61	-40	82	111.03	-21.34	-348	92	-38.33	-21.37	247	108
37.33	-21.71	380	156	110.41	-22.46	-530	89	110.99	-21.99	-409	87	111.74	-21.97	-391	90
-176.75	-22.26	523	23	-176.44	-22.15	752	33	-38.25	-21.94	411	111	37.05	-23.13	806	146
37.80	-22.97	740	121	110.30	-22.70	-486	87	110.93	-22.78	-462	92	-176.51	-22.50	911	22
-38.15	-23.10	240	125	11.41	-24.15	-244	133	11.71	-23.86	29	145	37.15	-23.75	955	138
37.58	-23.87	867	131	106.42	-23.72	-173	71	106.69	-23.79	-55	83	-38.81	-24.20	192	126
-38.47	-23.62	273	108	11.38	-25.04	-260	105	11.71	-24.83	-79	115	106.71	-24.67	-212	61
165.34	-24.98	91	113	165.78	-24.70	41	118	-38.84	-24.78	224	127	-38.32	-24.77	-118	124
-2.14	-25.01	-54	60	166.13	-26.43	228	114	166.53	-26.38	255	116	-173.87	-26.40	221	55
-39.52	-25.60	-396	161	-39.31	-25.76	-169	121	-4.16	-26.02	33	59	65.95	-27.33	334	47
-173.97	-26.75	12	58	-139.99	-27.11	397	59	65.47	-27.59	-34	35	66.00	-27.65	-422	46
66.58	-27.54	218	54	-174.43	-28.30	-220	62	-145.22	-28.26	745	55	-46.06	-28.20	-250	215
-38.98	-28.23	-639	128	-29.94	-28.12	681	62	112.44	-29.29	19	68	156.46	-29.29	-469	115
156.85	-29.13	-172	113	-174.54	-28.67	-216	58	-174.50	-28.52	-248	60	-145.47	-28.78	1070	57
-140.57	-29.46	481	67	-140.40	-29.15	561	74	-46.58	-29.46	-236	292	-46.40	-28.57	-284	236
-45.40	-29.40	-307	157	-43.62	-29.41	-240	150	13.70	-30.44	529	148	113.43	-30.38	-8	78
154.44	-29.67	-277	86	154.88	-29.67	-314	86	-140.84	-29.92	470	66	-46.08	-29.75	-313	257
-45.25	-30.20	-186	174	-43.95	-29.80	-312	150	113.73	-31.04	195	73	-141.22	-30.57	499	61
-73.19	-31.00	369	4	-46.52	-31.22	-255	159	-46.44	-31.27	-110	143	-44.58	-30.55	-350	187

Continued overleaf...

Table 1 – continued

Lon.[a]	Lat.[a]	z_r, m	Error, m	Lon.[a]	Lat.[a]	z_r, m	Error, m	Lon.[a]	Lat.[a]	z_r, m	Error, m	Lon.[a]	Lat.[a]	z_r, m	Error, m
-44.00	-30.86	-154	172	-43.16	-31.29	-317	153	14.73	-32.24	487	145	57.28	-32.46	789	46
-48.55	-32.19	-888	256	-48.00	-31.98	-737	223	-47.03	-32.16	-598	177	-45.99	-32.15	-472	147
-42.62	-31.55	20	119	-41.88	-31.91	70	112	-41.17	-32.26	-70	105	57.08	-32.74	680	47
57.70	-32.74	548	49	111.33	-32.76	43	91	-48.91	-33.25	-992	271	-47.90	-32.83	-889	210
-46.92	-33.06	-667	170	-46.03	-32.72	-608	149	-45.16	-33.16	-553	134	-37.15	-32.91	249	79
-49.83	-34.04	-1085	284	-49.27	-34.37	-944	215	-47.88	-33.89	-840	175	-47.06	-34.05	-829	141
-46.29	-34.43	-758	119	-43.88	-33.81	-421	113	-42.98	-34.27	-340	102	15.85	-34.63	338	85
158.45	-35.37	-197	80	159.12	-34.95	-219	82	159.63	-35.48	-109	83	-50.64	-34.95	-1126	244
-50.14	-35.27	-946	188	-48.98	-34.54	-856	178	-48.19	-34.57	-992	145	-45.80	-34.63	-750	108
-45.27	-34.86	-647	101	-42.52	-34.51	-582	102	-42.30	-34.62	-420	97	23.82	-36.44	225	92
25.18	-36.01	-304	114	110.04	-35.73	-333	71	129.18	-36.28	-607	79	158.12	-35.57	36	83
159.48	-35.54	-81	87	159.77	-35.94	-171	79	-49.63	-35.59	-890	154	-48.99	-36.00	-891	126
-48.34	-36.40	-903	113	24.03	-36.81	37	68	25.41	-36.86	-329	154	25.54	-37.36	-121	212
123.72	-36.94	-334	66	129.41	-36.61	-603	73	129.62	-36.92	-797	74	135.56	-37.20	-796	90
159.29	-36.70	-95	78	160.49	-37.49	65	73	160.92	-37.27	-73	76	-76.92	-37.47	88	23
-50.52	-36.93	-1080	149	-50.40	-36.99	-1049	142	-47.84	-36.71	-725	99	-47.29	-37.04	-789	97
25.71	-38.00	-484	234	50.32	-37.69	344	47	50.58	-37.66	549	26	137.15	-37.82	-617	80
160.29	-37.60	82	73	161.17	-38.34	38	78	161.82	-38.01	16	79	-76.64	-37.53	26	31
-76.00	-37.66	49	29	-75.34	-37.80	-117	38	-52.85	-38.16	-769	136	25.97	-39.00	-322	254
139.30	-39.17	-702	70	150.21	-39.22	-333	107	150.87	-39.23	-359	100	160.84	-38.51	114	73
26.16	-39.71	-109	260	139.28	-39.62	-728	71	150.02	-40.16	-21	101	-53.78	-39.84	-1018	141
-53.13	-39.81	-881	108	128.34	-41.08	-464	54	129.98	-41.30	-605	62	131.07	-41.44	-704	57
141.04	-40.89	-935	78	150.12	-41.17	-124	103	150.63	-41.43	-121	93	-54.78	-41.10	-1000	115
-54.37	-41.13	-991	121	132.18	-41.59	-495	55	132.96	-41.70	-467	55	150.03	-41.69	-128	102
150.77	-41.51	2	87	-56.62	-42.15	-1149	134	-56.03	-42.26	-1036	106	-55.22	-41.65	-1108	141
-77.96	-43.12	230	33	-77.00	-43.01	217	38	-76.37	-42.93	118	56	-55.03	-42.96	-1176	138
-56.85	-43.73	-994	139	-56.45	-43.50	-832	100	-77.80	-44.89	402	50	-77.00	-44.73	255	44
-76.39	-44.61	112	53	-57.78	-46.44	-791	210	100.39	-47.41	159	16	100.54	-47.48	229	15
-57.76	-46.79	-681	194	-57.10	-46.97	-616	160	-56.09	-47.00	-936	119	101.07	-47.68	86	17
101.85	-47.86	82	11	127.00	-48.24	-257	52	127.58	-48.31	-660	37	-57.10	-47.52	-405	175
109.22	-49.45	-155	26	126.95	-48.76	-1047	38	151.97	-49.33	563	72	109.44	-49.52	-261	21
109.86	-49.65	-216	31	114.44	-49.84	-1079	43	114.97	-49.96	-1033	41	133.17	-50.05	-299	4
133.65	-50.08	-272	4	151.24	-50.12	435	76	151.75	-49.57	491	71	151.22	-51.79	528	69
151.84	-52.75	614	60	153.83	-53.96	157	62	153.92	-55.01	505	57	153.98	-55.73	486	60
-57.84	-56.23	-530	92	-57.28	-56.35	-123	97	-56.01	-56.63	-473	126	92.72	-60.46	-876	138
-54.74	-59.90	72	81	40.02	-61.47	-403	75	89.40	-61.26	-140	111	89.78	-61.32	-107	114
91.17	-60.82	-285	111	92.23	-61.30	-453	124	92.73	-61.03	-474	124	100.75	-61.07	-352	102
117.47	-61.28	-802	99	132.54	-61.09	-1032	102	54.84	-62.33	-363	89	61.66	-62.42	-143	96
63.71	-62.33	-53	97	65.58	-62.31	-252	105	67.22	-62.26	-178	103	68.71	-62.28	-56	104
70.50	-62.06	-92	116	72.11	-62.48	-391	140	90.44	-61.92	-119	118	91.03	-61.71	-279	120
92.00	-61.69	-408	124	92.88	-61.76	-383	124	93.83	-62.30	-383	145	97.33	-62.35	-337	133
100.70	-61.79	-515	117	140.06	-61.67	-109	86	151.09	-62.27	263	63	-64.07	-61.88	610	59
28.46	-62.93	-1024	112	52.44	-63.42	-430	113	53.03	-63.21	-436	109	53.92	-62.78	-492	98
60.38	-63.49	-51	88	62.05	-63.00	-160	100	63.74	-63.01	-129	107	65.54	-63.00	-232	110
67.26	-63.00	-212	111	68.72	-63.00	-186	120	70.53	-62.99	-155	123	72.14	-63.02	-306	134
73.94	-63.43	-283	136	75.77	-63.11	-88	131	91.23	-62.86	-233	131	91.53	-63.22	-192	138
97.34	-62.55	-199	132	-66.39	-63.49	732	79	52.34	-63.54	-455	119	60.42	-63.53	-112	92
60.56	-63.65	-189	94	62.45	-63.58	-287	121	62.52	-63.68	-305	132	63.77	-63.59	-301	121
65.49	-63.68	-289	130	67.30	-63.74	-206	130	68.74	-63.70	-24	137	70.55	-63.61	-79	135
72.17	-63.71	-208	140	75.73	-63.58	-71	129	153.87	-64.33	-250	85	-97.99	-64.09	125	68
-70.09	-64.42	211	86	153.59	-64.55	158	75	-97.98	-64.85	62	69	-73.98	-65.10	-31	70
-73.19	-64.98	-166	73	-72.00	-65.17	-31	79	-71.18	-65.41	85	89	-129.38	-66.40	244	63
-72.81	-66.28	-232	96	-72.10	-65.95	193	93	-70.81	-65.52	163	94	6.01	-67.01	133	106
-75.90	-67.11	-684	112	-75.39	-67.46	-413	125	-4.96	-67.07	132	72	6.04	-67.64	435	78
-78.82	-68.35	-610	97	-77.99	-68.05	-681	96	-77.27	-67.80	-611	102	-75.50	-67.51	-387	124
-40.97	-69.08	-568	151	-40.47	-68.78	-638	136	2.19	78.69	897	82	3.89	78.86	187	119
2.19	78.69	897	82	6.36	76.66	1190	83	8.66	76.92	1388	96	14.52	75.41	734	249
-74.05	74.17	-314	382	3.49	72.53	1111	35	-132.60	73.08	-2136	436	-131.76	73.04	-2176	464
-13.79	73.24	1335	85	2.30	72.27	1051	78	3.57	72.01	1204	75	-143.24	71.72	-1946	382
-134.10	71.90	-2203	532	-14.96	72.22	1728	100	2.30	72.27	1051	78	4.33	71.36	898	94
-17.64	70.69	882	96	-17.31	71.00	1083	91	7.05	70.24	691	98	8.03	70.06	734	108
-19.17	70.08	1087	159	-16.25	70.08	1236	60								

[a] In decimal degrees

Table 2: 626 minimum residual depth measurements (upwards pointing triangles in Figure 1b of main text), averaged over 1° bins. Crustal corrections have not been applied, but crust is deemed to be thinner than average, based upon constraints from nearby lines, absence of seamounts, presence of fracture zones and regional tectonic setting. Additional error of 100 metres was included during spherical harmonic fitting to account for uncertainty caused by the lack of crustal correction.

Lon.[a]	Lat.[a]	z_T, m	Error, m	Lon.[a]	Lat.[a]	z_T, m	Error, m	Lon.[a]	Lat.[a]	z_T, m	Error, m	Lon.[a]	Lat.[a]	z_T, m	Error, m
3.82	69.69	972	16	3.46	68.80	1237	10	3.62	69.20	862	19	8.43	69.36	599	39
-140.58	58.06	-416	47	-51.63	54.39	-92	127	-51.00	53.91	-65	104	-50.48	53.51	-68	91
-50.26	53.34	-129	90	-41.52	48.51	687	32	-42.99	48.26	283	37	-45.89	44.75	194	57
-7.62	45.49	-526	32	-5.12	44.71	-2950	132	-57.16	43.59	-1577	219	-47.82	43.65	-548	82
31.21	42.63	-1776	367	-134.61	42.91	-88	2	-134.00	42.98	-137	2	-133.00	43.09	-94	2
-132.00	43.16	-195	4	-131.00	43.06	-254	5	-130.00	42.95	-133	5	-129.00	42.84	-273	6
-128.00	42.72	39	2	-127.00	42.60	154	0	-126.31	42.52	241	2	-57.02	43.33	-1417	189
-53.60	43.24	-1147	164	30.45	42.28	-1665	358	30.72	42.40	-1804	370	-125.81	42.46	372	4
-125.48	42.42	-72	9	-59.00	41.85	-1605	119	-56.33	41.59	-1742	112	-46.77	42.06	-281	37
-46.28	41.86	-592	46	-64.09	41.45	-457	136	-59.49	40.67	-1444	106	-57.91	41.08	-1476	95
-55.77	41.24	-1475	94	-55.24	40.74	-1368	77	-12.92	40.70	-1014	35	-12.49	40.82	-464	18
-58.60	39.70	-1111	61	-58.10	40.14	-1509	86	-56.73	40.36	-1510	82	-56.00	39.88	-1322	65
-54.84	40.17	-1186	57	-54.23	39.76	-1251	54	-48.61	40.35	709	25	-48.19	40.22	506	27
-47.23	39.94	42	32	144.40	39.08	-1193	29	-54.92	39.19	-1173	47	-54.00	39.03	-837	31
-53.45	38.99	-447	16	149.19	38.23	-522	7	144.00	33.62	-333	5	151.34	34.03	-714	9
-13.62	33.93	-312	57	-12.00	33.65	-450	67	143.66	33.39	-228	7	-14.57	33.22	381	30
-13.93	33.07	-79	49	-13.09	33.11	107	49	-12.00	32.97	109	67	-10.90	33.42	-518	79
-14.80	32.34	159	36	-14.03	32.19	162	42	-13.00	32.27	343	48	-12.21	32.24	241	79
143.46	31.21	-489	5	-15.99	30.79	252	43	-14.99	30.80	568	51	-14.13	30.90	939	63
-15.66	29.70	387	74	-15.24	30.21	829	60	-15.88	28.97	-31	94	-15.29	28.59	-404	122
-17.06	27.62	239	75	-16.48	27.51	14	95	-61.55	26.58	-783	5	-17.66	26.75	662	49
-16.99	27.12	195	78	-16.30	27.17	-213	113	-61.65	26.46	-790	6	-59.55	26.47	-1076	9
-18.00	26.25	838	46	-57.75	25.34	-933	6	-157.52	23.62	1002	1	-157.47	23.92	963	1
-17.76	23.55	-179	270	-17.46	23.53	129	306	-93.81	22.70	-1597	215	-93.38	22.98	-1562	202
37.74	22.43	1190	1	-94.67	22.14	-1857	259	-94.31	22.37	-1731	238	-65.50	21.97	-757	12
-17.80	22.44	-544	307	38.59	20.52	1713	31	-65.51	21.39	-587	15	155.72	19.66	-212	10
118.11	18.53	-657	40	123.19	18.62	-616	22	123.61	18.79	-1300	19	156.04	19.42	-132	7
117.77	18.43	-627	36	122.84	18.48	-746	37	133.07	17.80	-1064	1	133.78	17.82	-956	2
136.44	18.00	-393	1	137.00	18.00	-588	1	138.00	17.99	-753	1	138.77	17.99	-866	1
140.07	17.98	-636	2	141.00	17.98	-814	10	141.69	17.99	-975	18	144.09	18.01	-738	2
144.79	18.15	-565	2	156.44	17.78	-158	5	156.66	17.62	-224	6	158.43	17.73	-175	5
158.62	17.59	-138	5	84.64	17.05	-919	210	157.11	17.30	-156	4	159.12	17.23	-117	4
159.56	16.91	-159	5	-65.62	15.65	188	36	84.55	15.18	-748	166	149.48	14.67	-391	9
-76.25	14.58	184	40	-74.99	14.66	734	20	-74.50	14.75	395	27	113.80	13.82	-510	8
114.75	13.73	-538	5	-76.65	13.78	412	34	-76.40	14.29	661	26	-74.61	14.45	913	15
-74.00	14.21	738	26	-73.03	13.81	-7	54	-57.81	14.12	-1140	63	-57.48	14.37	-1699	73
113.08	12.66	-839	16	114.24	13.00	-588	7	115.14	12.78	-744	12	155.17	12.92	-375	4
156.00	13.16	-499	6	156.53	13.32	-577	7	-77.03	13.03	-132	63	83.53	12.27	-607	123
113.35	12.30	-729	11	113.63	11.92	-688	10	114.91	12.29	-637	10	-103.86	12.04	-142	0
-103.00	12.15	-62	0	-102.40	12.23	93	0	82.81	11.46	-725	125	155.16	11.25	-198	4
155.53	11.16	-110	3	-53.97	9.84	-861	62	-50.20	7.55	-1038	126	-91.34	7.21	-13	5
164.32	6.16	546	6	165.00	6.22	371	8	166.00	6.31	450	5	167.00	6.40	420	6
167.50	6.45	-1585	7	-43.63	5.84	256	20	-43.42	5.59	257	21	-43.16	5.26	226	21
5.74	3.56	-294	348	51.01	3.78	-702	30	51.83	4.02	-1110	36	-83.79	3.54	462	2
-44.35	4.24	-112	46	-3.94	3.84	-496	85	50.98	3.00	-65	16	-83.77	3.00	-113	1
-42.44	3.33	152	25	-4.51	2.95	-1889	133	51.38	2.31	-553	19	51.53	2.06	-822	21
-92.67	2.21	757	4	-83.74	2.00	-148	3	6.93	0.94	269	89	7.83	1.48	657	98
7.42	0.42	339	94	7.51	0.33	368	92	-42.87	-0.67	-801	163	-37.16	-1.14	167	23
42.42	-2.39	-619	187	44.13	-2.07	-468	108	42.20	-2.68	-870	209	42.20	-4.44	-235	119
45.17	-3.58	-724	64	-34.56	-3.55	189	44	8.49	-5.10	-994	119	45.00	-4.68	-659	60
45.66	-4.67	-463	44	80.17	-5.49	-803	30	9.97	-6.25	-931	162	79.95	-5.51	-878	32
128.13	-6.20	-2470	15	128.21	-6.55	-2261	15	42.04	-8.45	8	89	42.58	-8.56	-193	81
42.19	-11.00	544	106	-141.91	-11.43	807	3	50.51	-11.52	833	18	50.23	-12.51	1308	32
-144.68	-13.42	468	2	-144.09	-13.13	482	2	-143.34	-12.62	156	2	11.54	-13.92	629	61
-149.38	-15.73	920	3	-37.10	-16.04	-373	64	-149.79	-16.58	1152	3	3.21	-17.90	-390	8
3.55	-17.99	-392	7	-150.69	-18.39	1112	3	-150.39	-17.80	1501	7	7.17	-18.90	-578	19
8.00	-19.08	-470	20	8.55	-19.19	-419	23	-150.78	-18.57	1068	3	-150.96	-19.72	944	0
43.09	-24.25	570	51	43.34	-24.65	518	42	-11.74	-25.96	-170	2	-3.35	-25.84	-110	2
155.74	-29.58	-316	43	-73.52	-31.00	451	9	123.13	-36.47	-600	17	124.10	-36.43	-259	7
127.40	-36.07	-627	14	128.07	-36.24	-798	18	130.01	-36.41	-945	21	130.55	-36.47	-1068	26
-31.21	-36.48	353	9	123.33	-36.63	-442	11	127.22	-37.00	-656	9	128.06	-36.93	-712	11
130.90	-36.88	-946	19	131.81	-37.02	-1033	21	132.73	-37.11	-1075	22	136.93	-37.48	-1231	30
-30.82	-36.55	306	8	-30.00	-36.69	279	10	-29.14	-36.86	152	7	127.05	-37.75	-744	2
130.17	-37.70	-1085	12	131.48	-37.92	-1390	18	131.54	-37.67	-1327	19	133.01	-37.76	-938	9
138.08	-38.19	-818	12	138.39	-38.62	-641	7	139.50	-39.50	-11	0	139.90	-39.88	-541	9
150.58	-40.03	-512	52	129.00	-41.17	-803	0	140.43	-40.69	-739	9	141.70	-41.09	-643	13
127.35	-42.50	-723	0	127.81	-42.06	-802	0	131.49	-41.50	-514	0	134.00	-41.85	-669	0
134.82	-42.19	-638	0	142.16	-42.08	-507	8	142.80	-42.29	-498	10	166.00	-41.83	114	40
127.19	-42.50	-730	0	135.05	-43.00	-621	0	141.43	-42.65	-352	5	141.59	-42.55	-167	6
143.20	-42.85	-360	8	143.74	-43.27	-351	15	135.12	-44.00	-496	0	143.35	-44.05	-443	7
143.70	-44.03	-433	8	152.01	-43.91	29	26	153.00	-43.91	-105	23	154.00	-43.91	-51	17
163.03	-44.01	80	12	128.43	-45.20	-620	0	135.19	-45.00	-471	0	144.15	-45.17	-455	5
149.47	-45.33	93	29	149.54	-45.26	155	27	151.49	-44.61	-231	43	151.83	-44.76	-159	32
163.39	-44.52	-36	16	128.48	-45.64	-541	0	128.97	-45.84	-684	0	129.92	-46.04	-618	0
135.27	-46.00	-439	0	144.35	-45.95	-306	4	144.58	-45.95	-177	3	150.26	-46.43	-198	36
150.65	-46.37	194	12	130.13	-47.00	-551	0	135.31	-46.51	-203	0	144.79	-46.78	-45	4
130.24	-48.00	-521	0	151.89	-47.82	1	20	154.15	-48.49	200	17	154.53	-48.49	168	15
130.30	-48.51	388	0	147.29	-49.22	-18	7	153.06	-49.01	307	12	154.10	-48.73	326	9
154.74	-48.71	367	4	156.19	-49.24	-335	12	162.28	-49.42	285	2	-51.60	-48.72	-1187	13
-51.32	-48.92	-1333	20	-45.81	-49.11	-826	9	-44.77	-49.07	-612	5	-44.41	-49.37	-612	4
115.52	-50.08	-320	0	153.31	-49.84	-247	16	154.03	-49.94	50	9	154.64	-49.81	-187	10
156.47	-49.53	-337	18	156.97	-50.03	-232	13	158.32	-50.17	100	5	158.55	-50.45	194	6
160.46	-50.47	329	0	161.00	-50.16	94	4	161.82	-49.69	171	2	150.80	-50.97	591	11
157.47	-50.54	-404	19	157.93	-51.01	-107	9	158.88	-50.86	492	2	160.01	-50.73	326	1
-39.69	-51.36	-171	73	-39.33	-51.09	-68	52	151.59	-52.36	436	7	-40.82	-52.19	-511	95
-40.20	-51.73	-339	86	153.18	-53.41	-15	6	153.75	-53.27	142	5	152.78	-53.52	-19	6
157.88	-54.48	-462	8	158.17	-54.61	-77	5	159.38	-55.13	-430	1	159.80	-55.31	-95	4
156.84	-56.50	181	5	159.35	-56.50	-65	9	159.79	-56.50	2	15	-29.89	-57.48	-110	0
-29.00	-57.44	-243	9	-28.16	-57.41	139	11	-22.95	-57.17	-286	9	-22.00	-57.13	-60	8

Continued overleaf...

Table 2 – continued

Lon.[a]	Lat.[a]	z_r, m	Error, m	Lon.[a]	Lat.[a]	z_r, m	Error, m	Lon.[a]	Lat.[a]	z_r, m	Error, m	Lon.[a]	Lat.[a]	z_r, m	Error, m
-32.59	-57.60	59	8	-32.00	-57.57	-278	4	-31.00	-57.53	-281	2	-30.40	-57.51	-185	1
-31.98	-59.09	487	1	-31.00	-59.20	-21	1	-30.00	-59.30	232	1	-29.27	-59.38	941	0
90.88	-60.46	-232	43	97.24	-60.40	-284	37	132.50	-60.46	-718	21	-61.40	-60.47	230	5
-55.71	-60.26	-333	29	-22.92	-60.05	119	2	-22.30	-60.11	168	1	-2.06	-60.03	-566	11
46.87	-61.23	-573	21	97.27	-61.00	-336	46	107.33	-61.28	-420	19	112.23	-61.21	-715	35
126.02	-61.28	-997	46	131.46	-61.46	-941	46	140.04	-61.13	-281	20	140.84	-61.08	-372	22
157.25	-61.17	566	0	157.61	-61.42	472	0	168.24	-61.07	383	6	169.00	-61.30	766	1
169.58	-61.47	569	3	-61.12	-60.69	370	5	25.12	-62.46	-696	28	28.49	-62.31	-915	33
40.02	-61.96	-568	22	46.83	-62.01	-444	41	53.34	-62.32	-768	34	53.63	-62.11	-765	33
107.19	-61.80	-498	27	112.26	-61.52	-972	48	117.45	-61.61	-985	49	126.07	-62.00	-901	62
131.48	-62.02	-689	53	140.67	-61.56	54	16	141.81	-61.90	-275	23	150.24	-62.06	373	4
151.75	-62.44	210	4	158.12	-61.78	514	0	158.82	-62.27	580	0	170.14	-61.64	779	2
170.97	-61.87	850	3	172.00	-62.15	210	3	172.56	-62.30	536	0	24.33	-63.31	-843	35
24.80	-62.81	-681	27	34.21	-63.11	-924	40	41.77	-63.34	-560	29	46.79	-62.94	-420	67
57.05	-63.08	-458	35	126.11	-62.55	-702	66	131.50	-62.72	-912	65	147.33	-63.09	102	14
152.26	-62.56	143	3	152.65	-62.66	71	1	159.32	-62.62	556	0	160.00	-63.09	625	0
163.15	-63.47	552	0	164.00	-63.39	661	0	164.54	-63.34	596	0	166.44	-63.03	976	0
166.75	-63.30	1182	0	23.36	-64.36	-574	30	23.82	-63.86	-718	33	25.44	-64.30	-866	45
27.26	-64.13	-1209	59	28.42	-64.01	-1228	56	34.31	-63.84	-886	43	39.10	-64.46	-817	45
40.08	-64.38	-693	44	41.00	-64.10	-564	41	41.97	-64.16	-397	39	42.86	-64.11	-336	32
56.49	-63.99	-405	43	56.65	-63.73	-510	42	73.95	-63.63	-132	66	92.08	-63.88	62	75
162.00	-63.57	557	0	162.65	-63.51	411	0	167.25	-63.71	814	0	167.71	-64.10	701	0
-75.11	-64.46	12	14	-70.70	-64.26	-198	28	22.40	-65.39	-813	50	22.86	-64.89	-730	42
25.48	-64.80	-897	52	25.52	-65.30	-1126	75	27.07	-65.00	-1279	71	28.38	-64.78	-1408	72
37.27	-64.64	-910	47	38.00	-64.57	-896	46	38.61	-64.51	-1165	61	40.20	-64.50	-433	37
153.49	-64.62	-32	21	172.06	-65.43	452	10	172.56	-65.36	296	13	-74.76	-64.61	-71	16
-69.62	-64.53	94	41	-69.47	-64.57	35	48	-27.51	-65.20	-931	44	-27.20	-65.36	-728	36
21.43	-66.43	-708	65	21.89	-65.93	-780	59	25.57	-66.00	-1008	86	26.85	-66.00	-1192	78
171.46	-65.52	462	16	171.55	-65.51	507	9	-128.01	-66.02	247	5	-127.11	-66.30	327	5
-119.99	-66.15	48	14	-104.53	-66.24	-210	50	-84.61	-66.15	-519	38	-75.55	-66.47	-337	21
-75.22	-66.22	-156	16	-74.25	-66.42	-987	51	-26.70	-65.60	-624	33	-26.00	-65.94	-176	17
-25.18	-66.34	-130	16	21.34	-66.52	-634	62	23.09	-66.77	-1207	86	24.07	-66.99	-1201	95
24.98	-67.00	-1104	95	25.86	-66.77	-1070	97	26.91	-66.62	-1088	85	28.00	-66.61	-958	84
28.99	-66.59	-808	86	29.64	-66.58	-780	88	-132.51	-67.34	42	13	-132.38	-67.42	160	11
-130.80	-67.02	352	5	-130.00	-67.01	236	11	-128.96	-66.94	326	10	-128.00	-67.20	554	8
-126.99	-67.25	617	8	-126.25	-67.13	717	5	-119.98	-66.51	97	13	-109.92	-67.02	91	29
-104.54	-67.00	-358	55	-84.52	-66.58	-666	47	-84.48	-66.72	-565	46	-81.17	-67.43	-703	31
-80.00	-66.75	-576	34	-79.00	-67.00	-810	46	-78.00	-67.25	-760	55	-77.00	-67.40	-736	57
-73.95	-66.77	-833	55	-73.44	-66.57	-588	41	-24.68	-66.59	-219	19	-24.00	-66.92	-514	29
-23.16	-67.34	-475	27	25.46	-67.51	-1052	118	25.55	-67.54	-1415	119	-131.87	-67.73	299	10
-131.04	-68.23	548	7	-130.08	-68.00	690	6	-126.80	-67.74	806	7	-125.91	-67.94	831	10
-125.08	-67.80	935	7	-124.06	-67.73	947	8	-109.97	-67.71	289	31	-104.55	-68.00	-316	56
-81.80	-68.46	-884	48	-80.98	-68.08	-944	43	-80.00	-67.95	-840	30	-39.98	-68.49	-808	60
-28.93	-68.13	-578	41	-28.00	-68.13	-531	37	-27.00	-68.12	-459	33	-26.32	-68.12	-745	45
-22.66	-67.58	-670	35	-22.00	-67.91	-641	34	-21.14	-68.33	-725	39	-4.62	-67.52	-143	23
-1.64	-67.77	17	28	-1.45	-67.66	13	26	176.04	-69.28	510	17	-130.55	-68.53	543	11
-129.78	-68.60	722	10	-129.41	-68.81	754	12	-124.87	-68.66	850	13	-104.55	-69.00	-287	68
-98.85	-69.06	-421	44	-98.07	-68.92	-431	41	-89.66	-69.39	-155	41	-89.00	-69.31	-494	50
-88.00	-69.20	-361	54	-87.00	-69.08	-306	53	-86.00	-68.96	-226	51	-85.00	-68.85	-281	43
-83.94	-68.72	-552	38	-83.00	-68.61	-646	49	-82.30	-68.53	-869	55	-80.82	-68.50	-1126	63
-79.62	-68.63	-675	60	-79.38	-68.54	-626	45	-31.55	-69.49	-858	66	-31.00	-69.41	-875	66
-30.00	-69.26	-872	64	-29.00	-69.11	-770	55	-28.35	-69.01	-558	40	-20.65	-68.57	-527	33
-20.00	-68.89	-601	39	-19.09	-69.33	-592	44	-104.56	-69.72	-292	81	-103.51	-69.99	-276	59
-103.00	-69.61	-253	53	-102.00	-69.50	-145	50	-101.00	-69.50	-199	51	-100.00	-69.50	-100	43
-99.00	-69.50	-347	51	-98.00	-69.50	-274	43	-97.00	-69.50	-173	36	-96.48	-69.50	-946	36
-33.91	-69.85	-798	73	-33.00	-69.71	-834	71	-32.05	-69.57	-834	69	-18.58	-69.52	-669	48
-18.00	-69.65	-488	41	-17.00	-69.87	-316	35	-16.45	-69.99	-514	43	121.35	88.56	-158	65
125.00	88.72	-268	73	129.20	88.92	185	51	100.50	87.59	-355	64	105.00	87.80	-553	77
110.00	88.03	-342	70	115.00	88.26	-589	83	118.80	88.44	-392	76	77.15	86.52	149	2
80.00	86.65	612	2	85.00	86.88	475	2	90.00	87.11	-248	33	95.00	87.34	-307	47
97.95	87.47	-599	73	15.35	85.60	-1086	3	74.75	86.40	-674	1	16.55	85.25	-349	16
18.30	84.75	-205	9	20.85	84.01	-231	50	25.77	83.65	-318	74	27.65	83.58	-407	80
24.35	83.00	-395	81	28.90	82.98	-692	100	26.75	82.31	-682	105	29.40	82.07	-343	106
-0.40	79.70	118	66	-3.35	79.98	276	85	-0.40	79.70	118	66	-1.90	77.61	-36	91
-2.70	77.76	-58	93	-1.90	77.61	-36	91	0.65	77.15	284	62	0.65	77.15	284	62
5.35	76.31	956	21	-147.54	72.17	-2207	274	-140.64	71.65	-2181	363	-132.22	72.05	-1610	453
-140.52	71.39	-2457	425	-135.26	71.34	-2498	557	-103.53	-70.01	-343	64	-16.36	-70.01	-612	46
-158.75	-72.39	218	21	-155.44	-72.41	-102	37								

[a] In decimal degrees

Table 3: 488 maximum residual depth measurements (downwards pointing triangles in Figure 1b of main text), averaged over 1° bins. Crustal corrections have not been applied, but crust is deemed to be thicker than average, based upon constraints from nearby lines, presence of seamounts and regional tectonic setting. Additional error of 100 metres was included during spherical harmonic fitting to account for uncertainty caused by the lack of crustal correction.

Lon.[a]	Lat.[a]	z_r, m	Error, m	Lon.[a]	Lat.[a]	z_r, m	Error, m	Lon.[a]	Lat.[a]	z_r, m	Error, m	Lon.[a]	Lat.[a]	z_r, m	Error, m
-18.40	69.98	991	86	2.99	68.56	1473	48	3.30	68.39	2000	58	3.52	68.28	2443	60
-0.68	67.71	1215	121	-0.12	64.18	727	142	-23.29	63.70	3232	0	-0.12	64.18	727	142
-36.11	62.68	1516	20	-23.33	62.99	2191	25	-39.50	61.76	1875	38	-39.20	61.63	1641	34
-35.00	62.32	1203	20	-34.01	62.11	1131	16	-33.00	62.07	1448	7	-32.00	62.06	1533	6
-31.00	62.01	1635	5	-30.00	61.94	1675	5	-29.00	61.88	1854	3	-28.00	61.82	1826	2
-57.52	60.53	-24	64	-38.70	61.41	1396	31	-38.00	61.13	1097	31	-37.01	60.79	1042	21
-36.02	60.58	1167	12	-35.00	60.53	1321	7	-34.00	60.52	1342	5	-33.47	60.50	1215	4
-28.79	61.27	2245	72	-27.00	61.29	2028	5	-23.00	61.43	1672	15	-22.00	61.34	1704	21
-21.00	61.26	1644	19	-19.97	61.13	1318	27	-19.02	60.75	1474	23	-32.97	60.47	1404	4
-32.00	60.42	1386	3	-31.00	60.37	1735	2	-30.00	60.32	1729	2	-29.00	60.25	1847	1
-28.00	60.20	1726	3	-27.00	60.14	1560	7	-26.00	60.05	1410	8	-25.00	59.96	1504	8
-24.00	59.89	1616	12	-23.00	59.83	1417	21	-22.29	59.77	1254	22	-18.54	60.47	1647	18
-18.21	60.22	1735	15	-59.50	59.31	1422	60	-140.05	58.33	-359	132	-175.00	56.51	-665	131
-139.97	57.32	-352	126	-31.78	57.48	1521	0	168.39	56.39	-211	82	-176.72	55.62	-614	126
-176.00	55.99	-576	123	-175.26	56.38	-610	126	-173.87	56.18	-731	134	-172.29	55.65	-642	120
-178.69	55.17	-308	116	-177.96	54.96	-834	139	-177.21	55.35	-700	130	-176.50	54.67	-372	126
-135.63	54.53	185	125	-135.32	54.63	221	79	-42.91	54.77	920	83	-176.07	53.90	-202	115
-135.99	54.20	618	105	177.44	53.39	-204	111	-175.95	52.64	309	101	-157.10	53.23	5	57
-141.17	52.60	260	53	-138.75	53.13	17	80	-133.90	53.40	-828	122	-154.47	51.50	234	66
-148.37	50.73	119	27	-145.18	51.38	223	31	-169.80	47.93	-93	41	-174.82	46.88	-388	22
-126.07	46.93	-314	112	-9.85	46.89	-62	85	-143.18	45.57	-38	46	-128.80	45.87	398	76
-127.03	46.50	237	104	-125.97	46.23	-191	105	-15.35	46.14	995	107	-144.47	45.02	1	54
-132.63	44.70	-95	66	-163.78	44.30	-184	20	-143.12	43.82	-120	30	-140.63	43.97	-206	20
-137.10	43.75	92	48	-125.83	44.11	121	67	-134.45	43.00	-13	45	-160.65	40.98	234	57
-128.41	40.90	292	110	-126.67	40.97	319	100	-125.79	40.98	652	82	-18.96	40.56	-260	95
145.38	39.88	-165	44	146.00	39.78	-22	44	-172.98	39.70	-240	37	-136.27	40.30	-473	26
-128.18	40.07	-380	58	-67.12	39.83	-1020	220	-65.27	40.24	-370	74	-58.73	39.56	-940	51
-136.17	38.90	5	16	-128.00	38.58	-221	47	-124.92	39.15	31	96	-70.72	38.57	-474	173
-70.00	38.83	-319	170	-68.94	39.16	-278	156	-68.21	39.40	-297	154	-58.98	39.00	-779	43
-39.04	38.75	23	74	-37.12	39.12	629	123	-35.29	38.75	1034	94	171.99	37.70	-262	45
-125.02	38.14	-418	72	-71.91	38.02	-480	175	-71.24	38.12	-484	168	-69.99	37.54	-252	69
-66.17	38.23	302	123	-64.56	37.52	-119	23	-64.00	37.70	-80	21	-63.00	37.73	-245	25
-62.29	37.55	-705	43	-60.82	37.61	-680	35	-60.00	37.90	-213	17	-59.35	38.23	-505	29
-157.03	37.15	-241	39	-143.12	37.25	-218	32	-125.87	37.47	-344	64	-72.95	37.11	-580	185
-72.47	36.96	-468	155	-70.58	37.26	-281	70	-69.22	36.82	-193	50	-67.52	36.51	190	18
-67.00	36.69	-299	31	-66.00	37.02	-269	30	-65.05	37.35	-124	25	-61.85	37.44	-753	43
-61.31	37.44	-397	25	17.86	36.00	-1283	228	-125.89	35.62	-156	39	-125.03	35.52	-187	12
-72.29	35.66	-438	85	-69.94	36.06	-148	48	-68.90	36.22	-118	40	-68.03	36.34	11	28
-142.52	35.08	-101	28	-125.10	34.98	-187	48	-123.27	35.15	-231	67	-73.99	35.01	-643	155
-69.42	34.78	-366	22	-26.04	35.29	1393	37	-173.05	34.33	151	50	-134.25	34.45	-348	37
-126.03	34.48	-322	43	-122.13	34.37	308	71	-74.76	33.69	-971	152	-74.01	33.99	-996	122
-70.16	34.27	-397	24	-69.22	33.91	-199	15	-63.03	34.47	138	109	28.10	33.14	-2204	392
152.51	32.52	-396	44	-127.07	32.83	76	42	-125.93	32.98	64	53	-75.64	32.65	-1018	197
-74.97	32.88	-1041	130	-69.94	33.01	-470	23	-57.50	32.86	119	100	-53.43	32.87	-47	107
151.76	32.49	-448	33	-172.07	32.13	-241	42	-154.65	32.30	-276	30	-75.08	32.35	-896	131
-73.95	31.60	-801	52	-71.78	32.45	-735	35	-70.61	32.45	-749	32	-32.71	31.88	869	47
-31.14	31.85	527	60	-135.40	31.08	423	71	-120.90	31.30	49	30	-120.12	30.93	146	33
-75.01	30.99	-68	94	-74.33	31.41	-652	62	-72.95	30.73	-817	43	-66.00	30.72	71	12
135.07	29.74	-822	53	-152.68	30.45	-61	27	-121.73	29.87	413	24	-75.23	30.24	-148	58
-74.00	30.13	-362	65	-73.42	30.46	-725	50	136.53	28.75	-663	37	-153.52	28.75	184	79
-152.47	29.33	-374	22	-117.58	29.13	370	68	-117.41	28.77	281	49	-76.01	29.06	-361	35
-74.78	28.63	-302	41	-74.00	29.01	-355	53	-73.34	29.33	-303	70	-64.65	29.42	148	8
-174.18	28.34	-94	74	-127.42	28.08	-238	26	-75.80	28.09	-345	37	-75.25	28.03	-192	32
-169.08	26.70	792	27	-121.58	27.40	-238	21	-76.00	27.34	-365	43	-74.72	27.01	-139	38
-74.15	26.79	13	42	-70.22	27.50	-475	17	-69.14	27.37	-414	17	-168.83	26.07	1404	67
-163.70	25.50	502	8	-74.11	26.34	-27	23	-72.45	25.73	-493	83	-70.15	26.13	-725	82
-67.59	25.77	-432	66	-178.02	25.44	164	40	-160.32	24.67	896	21	-134.57	24.77	427	59
-92.41	25.13	-1857	347	-90.58	25.32	-1371	205	-90.49	25.11	-1635	225	-69.26	24.66	-586	82
-56.00	24.70	-829	5	-55.37	24.53	-661	2	128.12	23.86	-507	44	146.08	23.57	-636	40
-165.48	24.34	492	99	-160.48	23.96	683	0	-156.13	23.62	1376	24	-116.63	24.50	260	31
-54.88	24.40	-366	2	-51.46	23.51	-236	1	130.97	23.38	-111	22	138.78	23.44	-489	32
-156.58	23.10	1189	12	-155.90	22.80	1200	12	-151.00	23.00	-266	54	-148.05	22.97	71	65
-137.50	23.07	-98	34	-58.25	23.49	-343	73	-50.00	23.13	109	1	-49.00	22.88	67	1
-48.00	22.80	187	1	65.50	22.49	-235	190	-166.12	22.50	593	51	-155.22	22.22	1185	30
-116.05	21.97	77	36	131.88	20.10	-747	42	-161.42	20.30	821	5	-160.00	19.54	415	46
67.48	18.97	642	50	138.35	19.05	-741	12	-177.32	19.03	225	37	-157.70	18.87	687	71
-128.50	19.37	10	35	69.70	17.62	507	46	140.99	18.09	-633	51	-57.38	17.94	-573	53
69.94	16.83	599	30	-23.50	17.30	843	82	53.47	16.18	1414	61	69.80	16.43	607	25
136.78	15.62	-427	34	51.54	14.58	1514	88	-151.90	14.68	-295	57	-124.20	14.97	46	14
52.02	14.02	927	65	53.07	13.69	1069	33	69.42	13.73	393	14	69.58	13.79	623	8
130.53	14.16	-1055	23	46.30	12.91	1824	75	69.84	12.60	427	9	-24.35	13.48	372	50
44.31	11.77	2224	35	168.37	12.45	651	59	-111.05	12.22	260	90	-103.80	11.63	154	46
-98.78	12.18	-192	67	45.01	10.88	1924	63	69.38	11.32	182	11	69.86	10.98	406	6
161.58	11.33	1019	80	165.17	11.20	522	67	-145.88	10.72	296	46	-104.77	10.88	204	41
70.14	9.91	250	8	70.75	9.60	401	9	-93.48	9.80	427	33	70.19	9.46	288	6
70.44	8.18	697	7	120.28	7.58	-808	65	70.67	7.37	866	95	122.14	5.56	-824	90
-123.98	5.78	-75	71	122.83	4.08	-1254	101	-115.68	4.07	-75	62	-4.20	3.90	-599	167
123.62	2.92	-1597	100	138.17	2.91	-57	42	-2.77	2.91	-911	43	140.33	2.41	134	37
143.27	1.86	-71	43	-19.66	2.45	252	67	169.18	0.78	101	106	-116.08	1.45	231	78
-39.08	0.98	596	82	-123.43	0.18	-148	57	-23.86	-0.07	160	67	-22.68	0.17	198	25
-131.52	-1.38	-248	40	-40.07	-1.12	30	132	-26.67	-1.27	522	68	47.03	-2.92	-119	81
49.60	-3.47	795	56	51.48	-3.60	620	86	-114.22	-3.62	-262	67	54.59	-5.43	1244	17
58.48	-5.33	911	42	59.22	-5.42	1018	75	60.03	-5.45	550	40	74.30	-5.37	698	41
75.08	-5.35	470	56	54.84	-5.96	806	27	63.07	-5.52	1142	70	63.73	-5.55	325	38
69.97	-5.66	301	93	54.64	-6.65	757	22	-118.67	-7.33	-96	66	174.93	-9.02	162	35
56.50	-9.83	1233	39	57.12	-9.97	1428	95	57.88	-10.08	1488	39	-110.63	-9.67	362	64
153.81	-10.65	-69	0	-142.42	-11.33	433	20	-133.58	-10.75	618	30	109.62	-11.67	-35	102
115.45	-11.88	314	40	119.12	-12.49	254	8	-128.95	-11.77	328	43	93.22	-13.15	-169	11
115.35	-12.85	67	69	149.92	-12.58	-781	104	-143.55	-12.78	396	21	-108.50	-13.47	-150	53

Continued overleaf...

Table 3 – continued

Lon.[a]	Lat.[a]	z_r, m	Error, m	Lon.[a]	Lat.[a]	z_r, m	Error, m	Lon.[a]	Lat.[a]	z_r, m	Error, m	Lon.[a]	Lat.[a]	z_r, m	Error, m
90.80	-13.83	-10	18	115.55	-13.78	-656	56	118.43	-13.52	-439	48	154.11	-14.35	-371	37
-119.17	-14.27	271	54	-79.07	-13.58	218	38	108.15	-14.95	-157	41	113.48	-15.38	-319	19
114.01	-15.40	-39	11	150.62	-14.80	-322	176	153.44	-15.05	-168	16	153.81	-14.86	-332	21
-136.10	-15.03	9	42	-112.08	-14.73	60	39	89.32	-16.42	-380	59	114.22	-15.59	-294	10
-168.52	-16.27	-505	76	-160.98	-17.47	487	46	112.54	-17.80	970	3	-176.35	-18.32	653	0
-158.67	-17.53	313	27	-141.43	-18.47	168	60	38.26	-18.72	40	234	-176.44	-18.57	706	0
-81.55	-18.98	418	70	162.32	-20.01	44	50	162.74	-19.90	129	47	-175.94	-19.52	299	0
-113.75	-20.30	-203	71	97.20	-20.72	-288	27	-37.44	-21.48	128	45	37.81	-22.14	440	77
178.55	-21.92	-907	98	-147.63	-21.70	347	19	-79.07	-21.55	365	29	-38.54	-22.27	592	54
-37.32	-21.66	146	43	10.28	-23.15	-219	54	10.80	-23.00	-51	62	106.39	-23.22	-183	6
106.53	-23.27	-472	18	111.59	-22.70	-273	21	164.95	-23.00	418	99	-117.83	-23.27	336	67
-38.58	-22.53	717	52	10.32	-23.60	-315	57	36.45	-24.02	1571	78	166.04	-24.32	114	55
170.83	-23.90	-510	61	171.80	-23.53	-1145	79	57.45	-24.57	364	50	104.20	-25.05	564	41
107.79	-25.33	-340	5	11.39	-26.20	-227	44	11.99	-25.95	-56	59	-36.66	-26.22	21	32
-36.36	-26.23	-38	36	11.42	-26.67	-247	43	11.54	-26.55	-199	47	58.17	-26.93	-359	45
110.11	-27.08	-636	10	155.87	-27.10	-398	114	-88.82	-27.07	429	18	-45.60	-27.29	378	140
-45.34	-27.40	78	137	156.10	-27.78	-88	134	-106.93	-27.93	314	58	-96.32	-28.02	570	20
-45.41	-27.54	113	131	37.15	-29.49	-216	64	112.53	-29.26	-266	21	13.10	-30.07	60	87
33.38	-30.27	931	61	33.68	-30.38	892	59	111.52	-29.70	25	49	113.60	-30.28	263	12
176.00	-29.50	-317	101	176.77	-29.92	-658	59	13.41	-31.16	138	73	13.86	-31.21	138	87
61.87	-31.48	296	51	62.60	-31.35	687	27	113.41	-31.23	-26	14	13.48	-31.72	161	71
13.93	-31.73	241	81	32.49	-31.81	-24	115	61.50	-31.54	836	44	111.40	-32.48	2	13
111.68	-32.49	66	13	113.16	-32.10	376	7	113.81	-31.64	36	22	14.35	-32.53	386	94
31.26	-33.37	61	106	31.94	-33.03	559	103	62.08	-33.09	-40	36	102.75	-32.75	325	25
103.50	-33.02	290	77	109.32	-32.76	-104	13	110.31	-32.51	9	8	16.00	-34.08	194	36
96.02	-33.80	-81	45	105.92	-34.18	-323	43	28.48	-35.49	126	108	29.09	-35.37	-25	92
111.06	-35.35	123	13	112.04	-35.37	-8	9	73.67	-35.77	224	73	111.49	-35.84	218	2
111.59	-35.66	38	6	76.38	-36.85	743	79	78.52	-37.25	668	42	133.98	-36.89	-933	132
134.63	-37.12	-991	166	87.65	-37.93	-51	36	63.97	-39.75	271	54	-132.88	-40.60	-98	15
-96.08	-42.73	-263	55	-104.43	-43.77	185	59	-110.62	-44.58	-161	26	-45.13	-55.37	-764	16
-44.83	-56.01	-235	11	-44.56	-56.54	-29	17	11.48	-62.49	409	4	11.86	-61.99	470	4
11.11	-63.00	147	4	10.46	-63.88	-112	7	10.62	-63.65	-19	6	15.41	74.31	471	184
9.86	73.17	1190	146	13.46	72.09	948	187	-12.00	71.94	985	76	15.91	70.38	899	145

[a] In decimal degrees

Table 4: 64 locations of Neogene intraplate hotspot volcanism.

Name	Location	Lon.[a]	Lat.[a]	Reference
Afar	Ethiopia	43	10	[60]
Anahim	British Columbia	-124	53	[61]
Anatolia	Turkey	34	39	[62]
Ankaratra	Madagascar	47	-20	[63]
Ascension	S Atlantic Ocean	-14	-8	[60]
Atherton	Queensland	144	-20	[64]
Azores	C Atlantic Ocean	-28	39	[60]
Balleny	SW Pacific Ocean	163	-67	[60]
Bermuda	C Atlantic Ocean	-67	33	[60]
Borborema	NE Brazil	-37	-7	[65]
Bouvet	S Atlantic Ocean	2	-54	[60]
Bowie	NE Pacific Ocean	-135	53	[60]
Cameroon	Cameroon	9	4	[60]
Canary	C Atlantic Ocean	-20	28	[60]
Cape Verde	C Atlantic Ocean	-20	14	[60]
Caroline	W Pacific Ocean	164	5	[60]
Carnarvon	Queensland	147	-25	[66]
Cobb	NE Pacific Ocean	-130	46	[60]
Comores	Mozambique Channel	43	-12	[60]
Crozet	SW Indian Ocean	50	-45	[60]
Darfur	Sudan	24	13	[60]
Discovery	S Atlantic Ocean	0	-42	[60]
East Australia	Victoria	143	-38	[60]
Easter	SE Pacific Ocean	-110	-27	[60]
Eifel	Germany	7	50	[60]
Fernando	C Atlantic Ocean	-32	-4	[60]
Galapagos	E Pacific Ocean	-92	0	[60]
Gough	S Atlantic Ocean	-10	-40	[67]
Guadalupe	E Pacific Ocean	-113	27	[60]
Hawaii	C Pacific Ocean	-156	20	[60]
Heard	SW Indian Ocean	73	-53	[68]
Hoggar	Algeria	6	23	[60]
Iceland	N Atlantic Ocean	-20	65	[60]
Jan Mayen	N Atlantic Ocean	-8	71	[60]
Juan Fernandez	SE Pacific Ocean	-83	-34	[60]
Kerguelen	SW Indian Ocean	69	-49	[60]
Lord Howe	Tasman Sea	159	-33	[60]
Louisville	S Pacific Ocean	-141	-51	[60]
Macdonald	C Pacific Ocean	-140	-30	[60]
Marion	SW Indian Ocean	38	-47	[60]
Marqueses	C Pacific Ocean	-138	-10	[60]
Meteor	S Atlantic Ocean	1	-52	[60]
Mount d'Ambre	Madagascar	49	-13	[69]
New England	C Atlantic Ocean	-32	28	[60]
Pitcairn	C Pacific Ocean	-130	-26	[60]
Rahat	W Arabia	40	23	[70]
Raton	Colorado	-104	37	[60]
Reunion	W Indian Ocean	56	-21	[60]
Samoa	W Pacific Ocean	-170	-14	[60]
San Felix	SE Pacific Ocean	-80	-26	[60]
Semporna	Borneo	118	5	[71]
Shamah	Jordan	36	33	[70]
Sierra Madre	Mexico	-102	20	[72]
St Helena	S Atlantic Ocean	-20	-17	[60]
St Paul	C Indian Ocean	78	-38	[73]
Socorro	E Pacific Ocean	-111	19	[60]
Tasmanid	Tasman Sea	156	-39	[60]
Tahiti	C Pacific Ocean	-150	-18	[60]
Tibesti	Chad	17	21	[60]
Trindade	S Atlantic Ocean	-29	-20	[60]
Tristan	S Atlantic Ocean	-12	-37	[60]
Vema	S Atlantic Ocean	4	-33	[60]
Victoria	Victoria	145	-35	[74]
Yellowstone	Wyoming	-111	44	[60]

[a] In decimal degrees

Table 5: 9 amagmatic topographic swells with approximately radial drainage patterns.

Name	Location	Lon.[a]	Lat.[a]
Guiana Highlands	Venezuela	-64	5
Mantiqueira Mountains	SE Brazil	-45	-21
Atlas Mountains	Morocco	-5	32
Fouta Djallon	Guinea	-9	8
Albertine Rift Mountains	Rwanda	29	-2
Bié Dome	Angola	16	-13
Namibian Dome	Namibia	17	-22
Drakensberg Mountains	South Africa	28	-28
Hardangervidda	Norway	9	61

[a] In decimal degrees

Spherical Harmonic Coefficients

Table 6: Fully normalised spherical harmonic coefficients for $l = 30$ model shown in Figure 4a of main text.

l	m	f_{lm}, m	f_{l-m}, m	l	m	f_{lm}, m	f_{l-m}, m	l	m	f_{lm}, m	f_{l-m}, m	l	m	f_{lm}, m	f_{l-m}, m
0	0	0.0	0.0	15	4	-21.2	-26.3	21	17	9.8	-19.6	26	21	-68.4	65.7
1	0	-163.0	0.0	15	5	-40.5	16.8	21	18	-46.6	91.8	26	22	16.6	-5.4
1	1	108.8	-92.4	15	6	-22.3	-39.9	21	19	66.6	-19.6	26	23	-27.9	-1.7
2	0	40.6	0.0	15	7	-32.5	-86.4	21	20	11.5	-21.2	26	24	-12.8	-2.3
2	1	162.7	-169.8	15	8	2.6	-1.2	21	21	-18.1	-74.5	26	25	-4.3	-10.7
2	2	263.7	248.0	15	9	-100.5	51.0	22	0	-9.8	0.0	26	26	40.5	-13.9
3	0	280.0	0.0	15	10	-26.8	-66.1	22	1	68.6	12.7	27	0	47.2	0.0
3	1	59.3	-182.0	15	11	-10.6	2.9	22	2	-17.0	-14.1	27	1	31.3	33.0
3	2	-139.9	118.5	15	12	21.1	36.9	22	3	31.6	-6.0	27	2	-18.5	-5.7
3	3	-78.1	142.9	15	13	23.0	82.4	22	4	-9.9	-30.9	27	3	49.8	26.4
4	0	134.4	0.0	15	14	8.5	49.8	22	5	-21.8	27.4	27	4	30.6	-9.4
4	1	-34.1	-42.5	15	15	59.6	34.2	22	6	-3.0	55.7	27	5	-24.1	-1.4
4	2	31.8	306.7	16	0	16.1	0.0	22	7	11.8	-3.4	27	6	11.7	6.5
4	3	-31.4	-145.7	16	1	62.1	-62.8	22	8	1.6	3.9	27	7	20.9	14.7
4	4	-24.6	38.2	16	2	-31.4	5.4	22	9	-47.2	3.0	27	8	-1.9	-4.5
5	0	-9.5	0.0	16	3	-25.4	22.1	22	10	6.5	-0.7	27	9	10.0	-7.8
5	1	-70.9	-102.3	16	4	39.6	43.3	22	11	9.8	5.1	27	10	13.7	-1.0
5	2	-209.0	109.4	16	5	81.7	34.4	22	12	15.8	-73.0	27	11	-21.1	37.9
5	3	-57.7	-104.7	16	6	-74.2	65.1	22	13	-25.0	14.3	27	12	-19.4	-15.1
5	4	13.6	-119.6	16	7	59.9	13.7	22	14	38.6	20.2	27	13	-43.7	-50.0
5	5	174.8	-45.5	16	8	24.7	-27.9	22	15	-15.8	-97.6	27	14	32.4	4.1
6	0	-1.7	0.0	16	9	19.5	54.6	22	16	-37.5	65.7	27	15	-39.8	-6.1
6	1	-23.3	-184.8	16	10	46.4	-28.8	22	17	8.3	8.6	27	16	44.0	-28.0
6	2	-69.5	36.7	16	11	48.9	-42.7	22	18	-54.0	25.6	27	17	-13.2	-18.1
6	3	77.5	-147.0	16	12	-99.4	33.8	22	19	-38.7	-6.9	27	18	5.5	-8.6
6	4	-112.2	-49.0	16	13	-0.6	46.8	22	20	74.8	4.6	27	19	2.1	-28.6
6	5	107.7	151.4	16	14	-110.9	57.7	22	21	-67.6	10.2	27	20	-25.0	85.0
6	6	-202.1	-51.5	16	15	-15.8	-47.8	22	22	49.9	-82.8	27	21	-10.3	3.0
7	0	-102.9	0.0	16	16	17.2	5.6	23	0	-67.0	0.0	27	22	-36.5	10.2
7	1	55.7	-110.2	17	0	-5.9	0.0	23	1	-32.0	36.2	27	23	-19.2	-18.9
7	2	4.6	68.8	17	1	67.0	97.3	23	2	25.4	16.8	27	24	-33.2	-54.8
7	3	142.8	-2.9	17	2	51.2	-9.8	23	3	10.8	11.7	27	25	64.0	13.2
7	4	23.7	-331.1	17	3	-67.2	-51.7	23	4	-54.2	-60.5	27	26	15.0	-25.8
7	5	-24.5	157.3	17	4	-25.3	55.7	23	5	2.3	-20.2	27	27	-1.2	6.3
7	6	100.8	-31.1	17	5	4.6	56.2	23	6	15.1	-34.3	28	0	-59.4	0.0
7	7	-108.7	37.0	17	6	-81.0	-43.0	23	7	-9.7	-6.3	28	1	2.4	-4.8
8	0	-158.9	0.0	17	7	27.7	-32.8	23	8	19.3	-12.8	28	2	-26.8	7.3
8	1	-14.9	9.8	17	8	-47.0	33.3	23	9	-18.6	-38.2	28	3	7.4	10.2
8	2	-7.0	143.9	17	9	67.1	-15.4	23	10	-8.1	5.5	28	4	5.5	0.3
8	3	62.8	9.6	17	10	11.7	-41.4	23	11	-59.9	-55.3	28	5	-19.8	-10.6
8	4	-52.8	-28.2	17	11	27.1	46.3	23	12	12.9	12.6	28	6	-9.8	-46.3
8	5	-45.5	24.8	17	12	59.7	67.0	23	13	23.9	46.9	28	7	-34.0	-10.8
8	6	5.6	-62.8	17	13	-4.7	-65.4	23	14	17.1	-30.0	28	8	-13.1	39.0
8	7	5.2	71.8	17	14	12.2	8.1	23	15	-8.4	27.4	28	9	31.7	-8.2
8	8	42.5	-102.9	17	15	66.0	27.7	23	16	3.0	24.1	28	10	-11.3	-60.6
9	0	32.1	0.0	17	16	-63.8	33.7	23	17	34.4	-65.0	28	11	-22.8	16.2
9	1	-2.5	-147.3	17	17	33.7	50.2	23	18	-30.3	-10.8	28	12	25.3	-19.1
9	2	-13.3	129.8	18	0	82.6	0.0	23	19	-28.6	-30.7	28	13	-30.3	-68.7
9	3	45.9	128.6	18	1	53.9	55.2	23	20	70.9	5.7	28	14	-17.0	-20.8
9	4	-74.1	-24.0	18	2	-9.7	-5.3	23	21	-5.6	43.6	28	15	19.3	36.9
9	5	16.0	-50.6	18	3	-72.9	5.7	23	22	-8.3	-35.6	28	16	6.1	-8.5
9	6	194.9	36.3	18	4	-5.6	19.7	23	23	71.3	55.7	28	17	-10.0	-11.3
9	7	31.2	84.1	18	5	-7.4	-39.6	24	0	-26.3	0.0	28	18	-2.1	3.2
9	8	-50.2	-87.4	18	6	-11.3	21.2	24	1	-21.9	58.5	28	19	-2.7	-15.5
9	9	27.8	-20.1	18	7	6.6	-13.3	24	2	-1.1	15.9	28	20	-4.3	49.5
10	0	24.2	0.0	18	8	-50.4	47.6	24	3	-2.9	-13.6	28	21	-13.3	-51.4
10	1	119.5	70.8	18	9	1.0	-68.5	24	4	12.1	2.7	28	22	-20.5	0.2
10	2	-107.1	-61.5	18	10	33.4	41.8	24	5	14.2	2.7	28	23	-6.7	-25.9
10	3	68.8	-31.5	18	11	-9.8	-0.8	24	6	24.0	-22.0	28	24	46.5	2.9
10	4	-155.4	-100.7	18	12	-9.8	-18.3	24	7	26.7	-5.8	28	25	-6.7	-34.7
10	5	-31.2	72.3	18	13	12.0	0.1	24	8	-37.5	25.6	28	26	-25.5	46.3
10	6	-54.7	5.5	18	14	-68.3	-24.0	24	9	-4.0	-14.4	28	27	-4.2	23.1
10	7	-20.0	88.4	18	15	-1.7	16.9	24	10	48.4	-43.3	28	28	12.8	-6.3
10	8	-46.8	16.1	18	16	-13.4	-42.2	24	11	-28.0	-23.1	29	0	40.8	0.0
10	9	95.6	-124.1	18	17	-34.9	-42.6	24	12	-3.2	104.5	29	1	29.4	10.5
10	10	72.6	199.5	18	18	-3.2	44.7	24	13	23.8	28.7	29	2	-6.0	-25.4
11	0	49.7	0.0	19	0	-92.3	0.0	24	14	7.5	-5.6	29	3	5.2	-5.8
11	1	-85.3	-41.4	19	1	23.6	58.9	24	15	22.0	40.8	29	4	-17.6	-43.3
11	2	-123.3	2.5	19	2	25.5	26.1	24	16	-31.5	42.6	29	5	-9.1	-4.5
11	3	156.0	-33.7	19	3	-6.1	6.0	24	17	50.4	-41.1	29	6	55.9	4.7
11	4	-30.3	-65.7	19	4	28.6	-14.2	24	18	-30.4	-31.9	29	7	-31.6	13.0
11	5	-38.0	-116.4	19	5	-84.6	-31.6	24	19	62.7	16.5	29	8	-1.2	-42.8
11	6	31.0	-159.3	19	6	43.2	-42.9	24	20	21.4	-35.7	29	9	0.9	-28.6
11	7	-34.6	0.8	19	7	-35.2	-46.4	24	21	-6.1	-36.7	29	10	-50.5	46.9
11	8	-19.0	8.6	19	8	-28.8	49.0	24	22	1.2	60.6	29	11	-50.8	-8.5
11	9	-106.9	-49.9	19	9	-9.7	46.1	24	23	7.8	38.5	29	12	18.8	-15.0
11	10	38.7	26.7	19	10	30.2	-93.2	24	24	-62.0	65.0	29	13	2.0	17.1
11	11	-83.6	130.2	19	11	-61.1	-2.4	25	0	16.2	0.0	29	14	4.0	34.1
12	0	-50.9	0.0	19	12	-9.0	30.2	25	1	22.1	11.7	29	15	65.4	28.9
12	1	55.7	34.1	19	13	46.7	34.0	25	2	23.3	9.3	29	16	14.6	39.4
12	2	141.9	37.0	19	14	-3.0	35.8	25	3	-17.9	16.1	29	17	-0.2	47.9
12	3	-53.2	-43.3	19	15	-41.6	-35.9	25	4	-24.8	-26.1	29	18	45.6	3.2
12	4	60.3	0.6	19	16	-15.8	-14.5	25	5	11.3	57.3	29	19	-7.2	-2.0
12	5	93.5	-28.0	19	17	-23.2	-53.2	25	6	-6.2	-6.6	29	20	40.3	0.7
12	6	32.1	22.2	19	18	-15.5	-2.2	25	7	32.6	-15.5	29	21	-29.1	26.9
12	7	-90.3	29.0	19	19	-29.2	54.7	25	8	-27.7	0.9	29	22	2.4	-5.5
12	8	33.5	-79.6	20	0	81.8	0.0	25	9	-35.2	87.8	29	23	23.8	-20.9
12	9	62.7	73.6	20	1	54.5	-8.5	25	10	-4.7	6.6	29	24	-6.6	-24.0
12	10	-29.9	-75.9	20	2	59.0	-30.4	25	11	-18.9	-12.6	29	25	37.8	-26.1
12	11	-52.7	-18.0	20	3	-52.4	56.9	25	12	13.8	51.1	29	26	-33.9	60.0
12	12	-117.6	-2.4	20	4	-61.7	12.6	25	13	40.6	-13.4	29	27	-33.8	15.7

Continued overleaf...

Table 6 – continued

l	m	f_{lm}, m	f_{l-m}, m	l	m	f_{lm}, m	f_{l-m}, m	l	m	f_{lm}, m	f_{l-m}, m	l	m	f_{lm}, m	f_{l-m}, m
13	0	78.6	0.0	20	5	42.1	19.0	25	14	-7.8	28.1	29	28	-38.5	-13.7
13	1	-0.5	-36.3	20	6	-22.7	50.9	25	15	-0.4	-7.0	29	29	8.5	-38.7
13	2	-16.0	-53.6	20	7	-10.2	48.9	25	16	-11.0	-5.2	30	0	14.5	0.0
13	3	-112.8	89.7	20	8	-28.4	-60.5	25	17	10.9	14.5	30	1	-74.7	-11.5
13	4	-28.0	-27.7	20	9	7.2	0.1	25	18	1.7	2.0	30	2	40.8	10.7
13	5	-97.8	-82.2	20	10	-5.9	-6.4	25	19	28.2	27.6	30	3	8.2	-39.9
13	6	-29.7	83.7	20	11	46.2	32.4	25	20	14.7	17.3	30	4	-78.9	-8.0
13	7	58.4	-41.9	20	12	41.6	-22.2	25	21	-29.9	-19.2	30	5	-18.5	13.2
13	8	17.4	-27.0	20	13	-81.1	-72.0	25	22	-52.6	20.3	30	6	24.9	-41.7
13	9	-66.7	-21.2	20	14	-80.5	3.1	25	23	-3.5	2.5	30	7	4.8	-30.4
13	10	8.2	26.8	20	15	37.2	50.8	25	24	-36.0	-33.9	30	8	-3.7	-3.1
13	11	30.2	-24.6	20	16	1.4	-47.2	25	25	-27.8	-72.7	30	9	28.5	23.1
13	12	108.7	-139.6	20	17	83.9	1.9	26	0	-19.8	0.0	30	10	38.8	7.3
13	13	-48.8	1.6	20	18	44.2	38.4	26	1	2.0	12.4	30	11	-19.3	-24.1
14	0	-43.1	0.0	20	19	15.4	46.6	26	2	37.9	-16.2	30	12	-11.8	38.0
14	1	-4.5	110.6	20	20	-70.7	0.5	26	3	2.3	-12.1	30	13	12.7	6.4
14	2	89.2	-115.7	21	0	20.3	0.0	26	4	-27.2	22.5	30	14	-3.6	18.5
14	3	-32.6	-52.2	21	1	46.3	50.0	26	5	-22.6	2.3	30	15	9.5	-8.6
14	4	-73.7	21.3	21	2	16.1	21.1	26	6	-19.1	26.3	30	16	-25.6	19.3
14	5	-5.6	-13.1	21	3	-59.2	-2.7	26	7	19.1	-0.8	30	17	17.7	15.9
14	6	-8.8	-21.2	21	4	-23.2	-9.6	26	8	-36.5	19.0	30	18	-13.2	-29.7
14	7	21.4	-40.7	21	5	-13.0	68.9	26	9	72.3	38.2	30	19	-27.5	-6.0
14	8	66.5	43.9	21	6	-9.8	18.6	26	10	16.8	-35.6	30	20	39.6	-8.4
14	9	-10.9	-36.3	21	7	73.9	-10.2	26	11	0.5	13.1	30	21	21.9	40.2
14	10	61.1	92.4	21	8	14.8	-56.8	26	12	16.6	-0.6	30	22	-13.3	-8.6
14	11	103.0	-30.8	21	9	9.8	12.9	26	13	1.9	-12.0	30	23	8.7	-1.4
14	12	52.3	33.5	21	10	-18.6	45.9	26	14	10.0	36.4	30	24	-47.5	13.6
14	13	-70.8	20.4	21	11	37.0	-4.8	26	15	-3.1	-8.9	30	25	35.5	3.6
14	14	46.9	-134.1	21	12	29.8	-46.4	26	16	-1.0	-18.3	30	26	-4.6	-1.5
15	0	29.6	0.0	21	13	-70.8	65.5	26	17	-18.6	-14.5	30	27	-47.4	-13.9
15	1	73.6	1.5	21	14	30.3	7.5	26	18	7.4	4.8	30	28	2.8	-21.9
15	2	-91.1	56.7	21	15	20.7	-55.1	26	19	-15.7	8.7	30	29	1.9	19.1
15	3	7.1	-20.0	21	16	-5.7	41.2	26	20	5.8	-4.3	30	30	21.1	19.0